

ANALYSIS, MODELING, AND PREDICTION OF THE THERMAL AND MECHANICAL
BEHAVIOR OF POLYLACTIC ACID UNDER FUSED DEPOSITION MODELING

A Dissertation

by

XUNFEI ZHOU

Submitted to the Office of Graduate and Professional Studies of
Texas A&M University
in partial fulfillment of the requirements for the degree of

DOCTOR OF PHILOSOPHY

Chair of Committee,	Sheng-Jen Hsieh
Co-Chair of Committee,	Bruce Tai
Committee Members,	Sy-bor Wen
	Jun Zou
Head of Department,	Andreas A. Polycarpou

December 2018

Major Subject: Mechanical Engineering

Copyright 2018 Xunfei Zhou

ABSTRACT

Fused Deposition Modeling (FDM) is an extrusion based additive manufacturing methodology. During the manufacturing process, a thread of thermoplastic material is melted through the extruder and solidified on the building platform to form a specific shape. Affordability and feasibility promote the development of FDM technology, nevertheless, the product quality problem hinders the future growth of this advanced manufacturing technique. Therefore, the focus of this dissertation is to realize FDM product and process development by establishing the relationship between manufacturing conditions and product quality and seeking an approach to optimize the process conditions with the lowest cost. To accomplish that, a hybrid experimental/numerical approach is proposed to model, predict, and optimize the thermal and mechanical behavior of the FDM process and the manufactured product.

The proposed hybrid model had three major components: experimental, numerical, and prediction models. For the investigation of thermal behavior, both experimental and numerical models were used to analyze how extrusion temperature, platform temperature, printing speed and layer thickness affect the cooling time of the filament during the manufacturing process. After the accuracy of the numerical model was validated, a prediction model was developed to predict the dimensional accuracy and the residual stress of the fabricated part. For the investigation of mechanical behavior, experimental and numerical models were used to examine how the infill topology

impacts the modulus of elasticity for several FDM products. Then a prediction model was developed to predict the tensile behavior of parts given filament structure settings. For investigating process optimization, the numerical model provides an approximate representation of the original optimization problem. Then, the approximate solution can be iteratively updated by evaluation using the experimental model which is more expensive, but also more accurate. This process allows an optimum condition be predicted.

The investigation of thermal behavior revealed that reducing extrusion temperature, slowing printing speed, and decreasing layer thickness could help lessen the vertical distortion and residual thermal stress, while the high platform temperature might have opposing effects on deformation and residual stress. The results from mechanical behavior analysis revealed that minimize the air gap, and triangular infill pattern would be beneficial to UTS/weight ratio. In addition, the finite element model developed in this study could be used to predict the product breakage location under high load, facilitated the redesign process to increase the strength of the products. Finally, it is demonstrated the optimization algorithm developed in this study is superior to traditional optimization algorithms in the area of additive manufacturing applications, reduced the cost by at least 72.4% when compared with experimental-only method, and costs less than half of the fellow surrogate-based method. The future directions of this study would be focused on increasing the accuracy of the predictive model and reduce the computation cost of the optimization algorithm.

DEDICATION

Dedicated to those who always love and support me

ACKNOWLEDGEMENTS

I would like to thank my advisors, Dr. Hsieh and Dr. Tai for their guidance and support throughout the course of this research. I also would like to thank Dr. Wen and Dr. Zou for serving on my committee and giving valuable comments on my research work.

Moreover, I would like to acknowledge Texas A&M High Performance Research Computing for providing software support for our numerical simulation. I also want to extend my gratitude to Dr. Terry Creasy and Dr. Alex (Gwo-Ping) Fang for using tensile testing machines of their labs.

My thanks also go to my friends and colleagues especially Bo Peng and Hongjin Wang and the department faculty and staff for making my time at Texas A&M University a great experience.

Finally, I would like to express my deepest appreciation to my mother and father for their encouragement, patience and love.

CONTRIBUTORS AND FUNDING SOURCES

This work was supported by a dissertation committee consisting of Professor Sheng-Jen Hsieh, Professor Bruce Tai, Professor Sy-bor Wen of Mechanical Engineering Department and Professor Jun Zou of the Department of Electrical & Computer Engineering. All work for the dissertation was completed independently by the student.

Part of the data and analysis of this dissertation were already published in the Journal of Virtual and Physical Prototyping, Microelectronics Reliability, and SPIE. And the permission for reproduction was acquired.

This work was partially supported by a Texas A&M University-CONACYT Collaborative Research Grant (No. 230308), by a gift from Rockwell Automation, and by the Additive Manufacturing Center for Mass Customization Production, which is part of the Featured Areas Research Center Program within the framework of Taiwan's Ministry of Education (MOE) Higher Education Sprout Project. Any opinions, findings, and conclusions or recommendations expressed in this material are those of the author and do not necessarily reflect the views of the Texas A&M University, Rockwell Automation, or Taiwan's the Ministry of Education (MOE). Graduate study was supported by Graduate Teaching Assistantship of Texas A&M University.

NOMENCLATURE

Acronyms

ABS	Acrylonitrile Butadiene Styrene
AE	Acoustic Emission
AM	Additive Manufacturing
ANN	Artificial Neural Network
ANOVA	Analysis of variance
ARC	Adaptive Response Correction
DDM	Direct Digital Manufacturing
DoE	Design of Experiment
FDM	Fused Deposition Modeling
FEA	Finite Element Analysis
GA	Generic Algorithm
H	Honeycomb
HF	High-Fidelity
IHCP	Inverse Heat Conduction Problem
IR	Infrared
LC	Lamina Composite
LF	Low-Fidelity
MS	Meso-structure
PC	Polycarbonate

PEEK	Poly-ether-ether-ketone
PLA	Polylactic Acid
PTAT	Proportion to Absolute Temperature
R	Rectilinear
RP	Rapid Prototyping
RSM	Response Surface Methodology
S/N	Signal-to-Noise
SAMO	Surrogate-based Additive Manufacturing Optimizer
SAO	Sequential Approximate Optimization
SBO-MFM	Surrogate-Based Optimization Using Multi-fidelity Models
SEM	Scanning Electron Microscope
SM	Space Mapping
STL	Stereolithography
T	Triangular
UTS	Ultimate Tensile Strength

Symbols

A Cross-section area

a Variation of the measurement error

b Biased term

C Compliance matrix, Costs

E modulus of elasticity

F Force

f Frequency

G Shear modulus

h Convective heat transfer coefficient, Hypothesis

k Heat conductivity, Bending/twisting curvatures in the lamina, Iteration number

L Length

P Perimeter

Q Radiation intensity, Stiffness Matrix

q Specific enthalpy

\dot{q} Thermal energy generation

R Response

\mathcal{S} Surrogate model

s Printing speed

T Temperature

t Time

W Received radiation

w Weight

z Half thickness

Greek Symbols

ε Strain

γ Shear Modulus

ρ density

σ Stefan-Boltzmann constant, Stress

τ Transmittance, Shear strain

ν Poisson's ratio

Superscripts

\mathbb{R}^n Real coordinate space of n dimensions

$Q^{(k)}$ At k th iteration

Subscripts

O_{atm} Atmosphere

O_{conv} Convection

O_{diff} Effective diffusion

O_{E} Extrusion

O_{eff} Effective

O_{exp} Experimental

O_{g} Glass transition

O_{obj} Object

O_{p} Platform

O_{ref} Reflected

O_{sim} Simulation

O_{tot} Total

O_∞ Ambient

TABLE OF CONTENTS

	Page
ABSTRACT	ii
DEDICATION	iv
ACKNOWLEDGEMENTS	v
CONTRIBUTORS AND FUNDING SOURCES.....	vi
NOMENCLATURE.....	vii
TABLE OF CONTENTS	xiii
LIST OF FIGURES.....	xviii
LIST OF TABLES	xxi
1. INTRODUCTION	1
1.1. Motive	1
1.2. Fused deposition modeling mechanisms and applications.....	1
1.3. Quality issues and difficulties of products fabricated by FDM	5
1.4. Scope and research objectives.....	9
1.5. Sections overview	11
2. LITERATURE REVIEW	13
2.1. Modeling of thermal extrusion process.....	13
2.1.1. Analytical model	13
2.1.2. Numerical simulation model	17
2.2. In-process monitoring techniques	19
2.2.1. Embedded thermocouples	19

2.2.2.	Infrared thermography.....	21
2.2.3.	Other techniques.....	24
2.3.	FDM process design.....	26
2.3.1.	Process parameters	26
2.3.2.	Influence of process parameters on dimensional accuracy	30
2.3.3.	Influence of process parameters on tensile strength.....	32
2.4.	Modeling of mechanical strength of FDM manufactured parts	35
2.4.1.	Conservative isotropic model.....	35
2.4.2.	Orthotropic constitutive model.....	36
2.4.3.	Laminar composite model.....	37
2.5.	Optimization with the application of FDM	39
2.5.1.	Parametric optimization	39
2.5.2.	Methods of parametric optimization	40
2.5.3.	Recent advance on optimization of the FDM process.....	46
2.5.4.	Surrogate-based optimization using multi-fidelity models	48
2.6.	Summary	53
3.	METHODOLOGY	55
3.1.	Introduction	55
3.2.	Thermal behavior	59
3.2.1.	Experimental model	59
3.2.2.	Numerical model	64
3.2.3.	Estimation of convective heat transfer coefficient and interfacial conduct resistance using artificial neural networks.....	70

3.3.	Mechanical behavior	79
3.3.1.	Experimental model	79
3.3.2.	Numerical model	83
3.4.	Development of surrogate-based additive manufacturing optimizer	87
3.4.1.	Objective function	87
3.4.2.	Optimization algorithm	88
3.4.3.	Optimization performance evaluation	90
3.4.4.	Case studies	91
3.5.	Summary	92
4.	RESULTS AND ANALYSIS OF THERMAL BEHAVIOR OF POLYLACTIC ACID DURING THE FUSED DEPOSITION PROCESS	95
4.1.	Experimental model	95
4.1.1.	Analysis of deposition temperature	95
4.1.2.	Analysis of ambient temperature	98
4.1.3.	Analysis of effective diffusion time	100
4.2.	Numerical model	104
4.2.1.	Grid independence test	104
4.2.2.	Determination of convective heat transfer coefficient	105
4.2.3.	Validation of simulation results	111
4.2.4.	Simulation results on distortion and thermal stress	116
4.3.	Discussion	119
4.4.	Summary	120
5.	RESULTS AND ANALYSIS OF MECHANICAL BEHAVIOR OF FDM MANUFACTURED POLYLACTIC ACID PARTS	122

5.1.	Experimental model	122
5.1.1.	Analysis of stress-strain relationship.....	122
5.1.2.	Analysis of the modulus of elasticity and UTS	124
5.2.	Numerical model	128
5.2.1.	Grid and time step independence test.....	128
5.2.2.	Results of effective elastic modulus on unidirectional samples.....	129
5.2.3.	Analysis of stress concentration region on unidirectional samples.....	130
5.2.4.	Analysis of effective elastic modulus on bidirectional samples	132
5.3.	Formulation of knowledge-based library	134
5.3.1.	Implementing the knowledge-based library information system	134
5.3.2.	Cross-validation with extrapolation and interpolation	136
5.4.	Summary	139
6.	RESULTS AND ANALYSIS OF SURROGATE-BASED ADDITIVE MANUFACTURING OPTIMIZATION USING MULTI-FIDELITY MODELS	140
6.1.	Case studies	140
6.1.1.	Case study 1—simple non-linear function	140
6.1.2.	Case study 2—Gramacy & Lee function	142
6.1.3.	Case study 3—Six-Hump Camel function	144
6.1.4.	Case study 4—optimize tensile strength of FDM manufactured part	146
6.1.5.	Case study 5—optimize strength and volumetric shrinkage of FDM manufactured part.....	147
6.1.6.	Case study 6—optimize the modulus of elasticity over building time of FDM manufactured part	148
6.2.	Discussions.....	151

6.3. Summary	154
7. SUMMARY, CONCLUSIONS, AND FUTURE DIRECTIONS	156
7.1. Summary	156
7.2. Conclusions	158
7.3. Future directions.....	159
REFERENCES	161
APPENDIX A CALIBRATION OF INFRARED SENSOR.....	183
APPENDIX B THERMAL MODEL APPLICABILITY ANALYSIS ON ANOTHER FDM MACHINE	185
APPENDIX C EFFECT OF PROCESS PARAMETERS ON WALL WIDTH	188

LIST OF FIGURES

	Page
Figure 1 A schematic of FDM system [3].....	3
Figure 2 Numer of FDM machines sold between 2007 to 2014	4
Figure 3 A schematic of the model used by Rodriguez	14
Figure 4 A schematic of contact area of a single filament [32]	17
Figure 5 An illustration of process parameters	26
Figure 6 Structures of rectilinear, triangular, and honeycomb infill patterns	28
Figure 7 A typical non-linear neural network	43
Figure 8 The flowchart of a typical SBO-MFM process	49
Figure 9 The flowchart for investigation of thermal behavior	57
Figure 10 The flowchart for investigation of mechanical behavior	58
Figure 11 The flowchart of SAMO	59
Figure 12 A schematic of the experimental setup for thermal behavior analysis	61
Figure 13 A grey scale image of the temperature matrix taken by the infrared camera ..	62
Figure 14 An example of the numerical model and its meshing scheme.....	68
Figure 15 Locally refined mesh in the region of interest	73
Figure 16 The numerical model used in the determination of boundary condition	73
Figure 17 The topology of the ANN model used to determine boundary condition	74
Figure 18 Performance of the trained model.....	76
Figure 19 An image of the experimental setup to determine boundary condition	77
Figure 20 An illustration of the points of interest in the boundary condition determination study	78

Figure 21 The dogbone structure and its dimensions.....	79
Figure 22 An example of bidirectional sample	80
Figure 23 An image of the tensile testing process	82
Figure 24 The conversion process from G-code to 3D FEA model.....	84
Figure 25 A plot of deposition temperature over time under experimental condition No. 1	96
Figure 26 Plots of deposition temperature over time for all experimental conditions	98
Figure 27 A plot of ambient temperature over time.....	99
Figure 28 Results of S/N ratio of effective diffusion time under experimental condition	102
Figure 29 A plot of temperature distribution curves with regard to element size.....	105
Figure 30 Plots of calculated h_p (left) and $h_{ambient}$ (right) in 100 networks.....	106
Figure 31 A plot of temperature history of two points under experimental and numerical conditions.....	106
Figure 32 The cumulative probability function of estimation results with error induced from training for h_p (left) and h_{∞} (right)	109
Figure 33 The cumulative probability function of estimation results with error induced from testing for h_p (left) and h_{∞} (right)	110
Figure 34 A S/N ratio of effective diffusion time under numerical condition	113
Figure 35 A comparison of effective diffusion time in this study and previous literature	115
Figure 36 A contour image of z-direction distortion of the model	116
Figure 37 A contour image of residual stress of the model	117
Figure 38 S/N ratio plots for distortion (left) and residual stress (right).....	118
Figure 39 Stress-strain curves for unidirectional samples under tensile testing	123

Figure 40 Stress-strain curves for bidirectional samples under tensile testing	123
Figure 41 An illustration of semi-crystalline polymer stress-strain curve	124
Figure 42 S/N ratio analysis for UTS (left) and UTS/weight ratio (right)	127
Figure 43 Plots of load force over node number (left) and time step (right)	128
Figure 44 Fracture point in experimental and numerical conditions for sample #1 to #9	132
Figure 45 The ANN used to construct the knowledge-based library	136
Figure 46 The flowchart of constructing the knowledge-based library	136
Figure 47 The regression performance of the developed network	138
Figure 48 Comparison of optimization error of SAMO, RAO, and ARC algorithms for case #1	141
Figure 49 Gramacy & Lee function	142
Figure 50 Comparison of optimization error of SAMO, RAO, and ARC algorithms for case #2	143
Figure 51 Six-Hump Camel function	144
Figure 52 Comparison of optimization error of SAMO, RAO, and ARC algorithms for case #3	145
Figure 53 Plots of convergence steps and estimation error in 100 runs with random initialization process	154
Figure 54 Schematic of experimental setup on Machine B	186

LIST OF TABLES

	Page
Table 1 The relationship between process parameters and increasing of vertical deformation.....	32
Table 2 The relationship between process parameters and increasing of tensile strength	35
Table 3 Summary of most recent (2014-2018) work on FDM process optimization	48
Table 4 Design of experiment for analysis of thermal behavior	64
Table 5 Material properties used in numerical modeling of thermal behavior	69
Table 6 Design of experiment for mechanical behavior investigation	81
Table 7 The testing cases for developed SAMO	92
Table 8 Results of effective diffusion time under experimental condition	101
Table 9 Results of ANOVA analysis on effective diffusion time under experimental condition	103
Table 10 Comparison of experimental, numerical, and literature value of effective diffusion time.....	111
Table 11 The highest von Mises stresses for each condition in the developed simulation model	118
Table 12 Tensile strength and the modulus of elasticity of all samples tested	126
Table 13 The modulus of elasticity of unidirectional samples obtained by MS approach and experiments	129
Table 14 The modulus of elasticity of bidirectional samples obtained by MS approach, LCT approach, and experiments	134
Table 15 Details of the SAMO attempted experimental runs and the corresponded response in Case 5	147

Table 16 Details of the SAMO attempted experimental runs and the corresponded response in Case 6	148
Table 17 LF model results used to establish the surrogate model and the SAMO suggested HF model results	150
Table 18 Results of samples manufactured in the vicinity of the obtained solution.....	151
Table 19 The convergence data for different sampling strategy	152
Table 20 The convergence data for low-fidelity model accuracy	153
Table 21 The calibration results	184
Table 22 Comparison of experimental and numerical values of effective diffusion time on Machine B.....	187
Table 23 Measurement results of the wall width for all experimental conditions	188
Table 24 ANOVA results of the wall width.....	189

1. INTRODUCTION

1.1. Motive

Additive manufacturing (AM), also known as 3D Printing, Direct Digital Manufacturing (DDM), Rapid Prototyping (RP), additive fabrication, or solid freeform fabrication, is a technique that could form selected surfaces using a fluid medium capable of changing its physical state in response to specific stimuli. Up to now, the most commonly used additive manufacturing systems are those based on extrusion, such as fused deposition modeling (FDM) [1]. An appropriate FDM process is vital since every manufacture process parameter could potentially affect the final part quality.

The next few chapters would elaborate on the mechanisms, the applications of the FDM process and the reliability problem of FDM manufactured products. Finally, difficulties on quality improvement of FDM products would be addressed, and the nature of the research problem is summarized.

1.2. Fused deposition modeling mechanisms and applications

Invented by S. Scott Crump [2], the technique of Fused Deposition Modelling uses a movable nozzle to deposit a thread of molten plastic material onto a surface. In a typical

¹ Part of this section is reprinted with permission from ‘*Experimental and numerical investigation of the thermal behaviour of polylactic acid during the fused deposition process*’ by Xunfei Zhou, Sheng-Jen Hsieh & Yintong Sun Virtual and Physical Prototyping Vol 12:3 pp. 221- 233 (2017) and *Modelling and estimation of tensile behaviour of polylactic acid parts manufactured by fused deposition modelling using finite element analysis and knowledge-based library*’ by Xunfei Zhou, Sheng-Jen Hsieh & ChenChing Ting Virtual and Physical Prototyping (2017). Copyright 2018 by Taylor & Francis Group

process, a thermoplastic filament is first fed into the machine through a pinch roller driven by a step motor. Then the filament would be heated in a preheated liquefier chamber to its liquid state; in the meantime, the solid upper portion is continuously pushed into the chamber, works as a piston to force the melted part out of the nozzle. A gantry is commonly used to control the extrusion path with a nozzle located at the bottom of it. The gantry is capable of moving horizontally as the material is deposited on a building platform that can be moved in the vertical direction. After fabrication of each layer, the platform moves down and enables the building of the next layer on the previously finished layers, as shown in Figure 1. Therefore, FDM offers users the ability to create arbitrary and complex three-dimensional geometry without increasing manufacture difficulty.

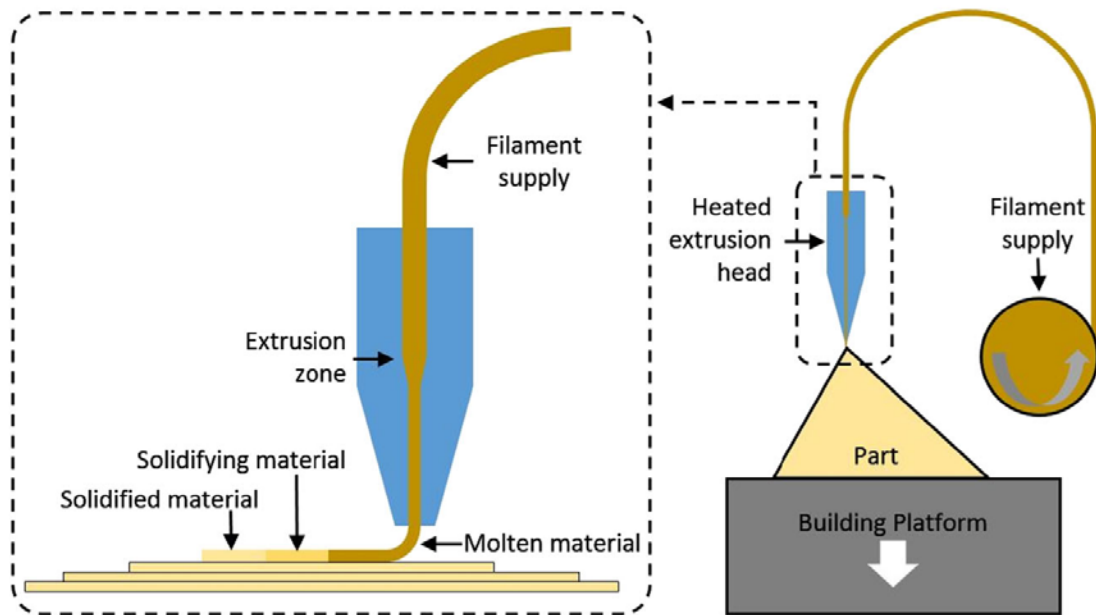


Figure 1 A schematic of FDM system [3]

Due to affordability and feasibility, FDM has become the most popular Additive Manufacturing (AM) process worldwide since the early 2000s. According to research from Wohlers [4], Stratasys, a company founded by Crump et al., is the dominant company in the market, sold around half of all FDM machines. However, with the patent expired in 2007, the whole FDM industry started booming. In a comprehensive industry

² Figure 1 is reprinted with permission from Kruth, J. P. (1991). *Material increment manufacturing by rapid prototyping techniques*. CIRP Annals-Manufacturing Technology, 40(2), 603-614. Copyright 2018 by Elsevier

survey conducted by Wohlers Cooperation [5], over 130k low-cost FDM-based 3D printers were sold in 2014, compared to only 66 sold in 2007, as indicated in Figure 2.

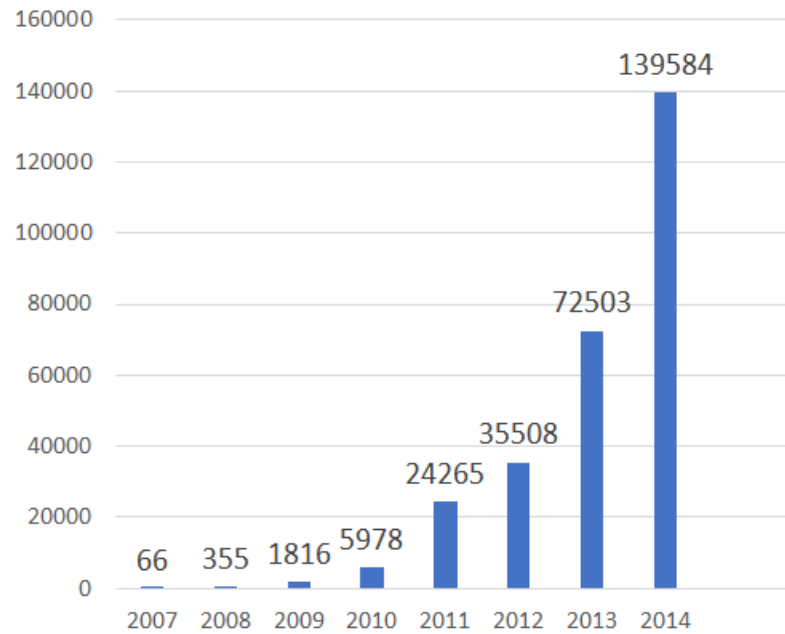


Figure 2 Numer of FDM machines sold between 2007 to 2014

The simplicity and the relatively cheap equipment of the FDM process render this technique's success in the field of tissue engineering, bio-engineering, and aerospace engineering. Scaffolds in tissue engineering are used to provide support for cell attachment and require hierarchical porous structures to achieve desired mass transport and mechanical functions [6], while 3D printer offers doctors the ability to print the

scaffolding layer by layer into a working tissue sample or organ [7]. In the fields of bioengineering, AM techniques including FDM could create 3D models for surgeons for practice and planning surgery [8], construct a dental model without traditional impression approaches [9], and produce microfluidic devices with biocompatible surfaces [10]. As a low-cost and flexible manufacturing technology, FDM is also successfully tested as a potential substitute to manufacture turbine blades [11, 12] and pump impellers [13]. Some of the influential companies view 3D printing as the future trend of manufacturing, General Electric (GE) Aviation plans a \$3.5 billion investment in AM, aims to produce over 1 million additive manufactured parts for its LEAP and GE9X engines [14].

1.3. Quality issues and difficulties of products fabricated by FDM

The quality of products is the most critical concern of the manufacturing industry. In general, the mechanical properties of plastic products fabricated by FDM are less than those made with traditional plastic processing methods. The tensile strength and compressive strength of acrylonitrile butadiene styrene (ABS) samples manufactured by FDM were 65%–72% and 80%–90% of those made by injection molding, respectively [15]. And the tensile strength of polypropylene homopolymerize samples manufactured by FDM exhibited a 20%–30% decay when compared with specimens produced by compressing molding of the same material [16]. However, with a proper post-treatment method, impellers fabricated by FDM could show a similar performance as the original impeller of a rotodynamic hydraulic pump, within a 2.5% deviation in the flow behavior

curve [13]. The variable properties and performance of FDM product are caused by the intermittent nature of the manufacturing process. Filaments are extruded and melted at the same time, and inaccurate control of such processes could create quality issues, such as layer shifting and weak infill. In addition, the machine deposits material in a directional way, resulting in anisotropic behavior of the manufactured parts.

Apart from mechanical strength, another important aspect of FDM part quality is dimensional accuracy. Dimensional accuracy is defined as the fidelity of part geometry to the original computer design. Similar to mechanical properties, dimensional accuracy of the final part is dependent upon the process design parameters as well as the properties of the raw material. Dimensional error in the final part is mostly induced from warping [17] caused by residual thermal stress created by uneven heat distribution as well as shrinkage [18] during the cooling process [19]. Deformation of the part could potentially lead into inner-layer delaminating or crack, and even cause fabrication failure [17]. Uneven heat distribution or thermal gradients are inevitable in the FDM process. When the hot melted material is depositing on a previously solidified cool part, the temperature of the below layers will rise again, creating a large thermal gradient in the vertical direction. The repetitive heating and cooling near the extrusion region make residual stress accumulated inside of the part, leads to deformation of the part.

Since both mechanical properties and dimensional accuracy are strongly dependent upon process parameters, a good understanding of this relationship would be necessary.

Moreover, with the thorough understanding of the process-product-property relationship, an optimization of the process can be performed to address the current quality issues associated with FDM technology. In this way, pre-process modeling and prediction approaches, in-process monitoring methods, and post-process analysis should be thoroughly investigated.

As mentioned above, the application of FDM is hindered mainly due to uncertainty regarding dimensional stability and mechanical properties of the products. Therefore, those attributes should be optimized to increase the reliability of the FDM manufactured products. However, limited understanding of the FDM processes, especially the deposition process, dramatically hinders the future growth of FDM technology [20]. An in-depth knowledge of FDM processes could be gained through experiments and theoretically analysis so that a model can be constructed to quantify the relationship between input and output parameters. One of the first challenges in modeling extrusion behavior is the highly dynamic and complex heating, melting and solidification of materials during the FDM process. Analytical models are cost-effective but to develop an analytical model for such a complicated process requires underlying assumptions carefully selected. On the other hand, numerical models stem from the physics of the process and can demonstrate very detailed system behavior. However, they are time-consuming to build, run, and need additional validation.

To optimize the FDM process, variables of interest should be obtained first. In-process monitoring is the integration of one or more sensor measurements, such as electrical, optical, and temperature, in determining the state of the processes [21]. The monitoring of process variable not only provides validation tool for predictive models but also facilitates development of closed-loop control system. Currently commercialized FDM machines just applies closed-loop control in sub-systems of the printer such as nozzle and step motor while the overall control of printing is still open-loop [22]. The machine does not track the actual dimension of the product so that a small printing error would lead to increase dimension error in subsequent layers. Hence human efforts are required to monitor the deposition process. Several process monitoring techniques for FDM have been developed to date, including optical cameras [23], embedded thermocouples [24], and acoustic emission [25]. Nevertheless, there are limitations for these inspection methods: the scan quality of optical cameras is limited for surfaces with overhangs or undercuts; pre-embedded thermocouples can only measure temperature at a few fixed points, and the signal-noise ratio of the acoustic emission method is mostly dependent on the location of the sensor and the distance between the source and sensor.

And finally, the optimization of FDM process involve various process parameters and complicate objective functions [26]. To apply traditional optimization techniques to it, a great amount of experiments need to be performed to find the global optimum condition. For instance, if the traditional response surface methodology was used to optimize a 4-parameter 1-response problem, at least 30 experiment conditions need to be considered,

let alone additional replicate experiments to ensure repeatability. Considering the machine operation and material cost, as well as the time required to characterize the properties of the products, those techniques are expensive in nature. Difficulties of the traditional optimization methods, in the context of process improvement and product quality enhancement, are the main incentives for developing alternative cost-effective optimization algorithm which could benefit from pre-process property prediction approaches.

1.4. Scope and research objectives

Mechanical strength and dimension accuracy are two of the most crucial factors for product development of FDM technology. However, the solid-liquid-solid change of material in the FDM process make it extremely hard to accurately model thermal and mechanical behavior of the manufactured products and predict the associated strength and accuracy. Multiple methods have been applied to model, predict, and optimize the thermal and mechanical behaviors, but there are limitations in these ways. An approach which is easy to perform, low cost and automated is required to predict the properties of the products and optimize the manufacturing process is essential to improve the quality of FDM fabricated products.

The objectives of this study are focused on product and process improvement of FDM technology. To accomplish that, analysis, modeling, and prediction of thermal and mechanical behavior of the FDM process is necessary. To understand how process

parameters affect the transient temperature distribution and residual stress during the layer-by-layer manufacturing process, an experimental model will be first developed utilizing cost-effective infrared thermography. Transient thermal behavior will be characterized by spatial thermal history and temporal cooling rate of the extruded material. A parametric study would be conducted to evaluate the effect of process parameters on parts' thermal behavior. With the establishment of an experimental model, a numerical model will be used to simulate the heat transfer phenomenon during the same manufacturing process. The numerical model will be first validated with thermal history measurement results then it would be used to further investigate the influence of process parameters on residual stress and part deformation.

A similar experimental-numerical approach would be applied to investigate the process parameters on tensile properties of the manufactured part. Tensile testing of parts with various infill topology design would be first performed. A meso-structure simulation technique is going to be developed to characterize the tensile behavior of numerical simulation models with the same filament geometry. The accuracy of the results will be validated by comparing the experimental results with the results obtained from the finite element simulations. And the performance of the proposed model would be compared against other existing modeling approach.

Finally, the same hybrid model approach would be adopted to optimize the manufacturing process to enhance required properties of the product. The proposed

optimizer is developed to guide the decision-making process in optimization manufacturing conditions by combining cost-effective but less accurate numerical models with expensive but accurate experimental models. A numerical simulation based predictive model would first generate a series of design cases to approximate the solution to the original optimization process. Then iteratively, the optimizer would be updated with most recent performed experimental results and estimate the optimal solution. In summary, this research would provide the FDM industry with the knowledge to develop better monitoring techniques, more accurate modeling approaches, and much cheaper optimization method to address the quality of the manufactured parts.

1.5. Sections overview

Sections are organized as follows:

- ❖ Section 2 reviewed existing analytical and numerical modeling approaches for thermal behavior of the FDM process, current in-process monitoring approaches, infrared thermography as a methodology to describe surface temperature, up-to-date mechanical strength modeling approaches, and methods used to optimize FDM process.
- ❖ Section 3 describes the methodologies applied to understand and characterize the FDM process.
- ❖ Section 4 shows and analyzes the experimental and numerical data describing the thermal behavior of the FDM process.

- ❖ Section 5 shows and analyzes the experimental and numerical data describing the mechanical behavior of the FDM products.
- ❖ Section 6 present the results of the developed optimization algorithm with several case studies.
- ❖ Finally, Section 7 draws the conclusion and presents the future work.

2. LITERATURE REVIEW

2.1. Modeling of thermal extrusion process

2.1.1. Analytical model

The development of analytical models is critical for modeling and predicting thermal behavior that accounts for the quality of the products. An understanding of material property changes during the deposition process would enable optimization and control of such processes. Few analytical models have been established to predict the thermal history of a filament under extrusion. Rodriguez and Thomas performed a 2D transient heat transfer analysis of a single-road-width solidification process [27]. They assumed that filaments have a rectangular cross-section, the effects of conduction to the platform can be neglected, and any contact resistances between filaments are negligible. With the boundary condition set based on Figure 3, they derived that the transient temperature over the bead cross-section is

$$T_{ave}(x, y, t) = T_E + \frac{2T_E}{W} \sum_{m=1}^{\infty} \sum_{n=1}^{\infty} \left(\frac{\alpha_{mn}}{\beta_n} \sin(\lambda_m y) \cos\left(\frac{\beta_n W}{2}\right) \right) e^{-\alpha^2(\lambda_m^2 + \beta_n^2)t} \quad (2.1)$$

³ Part of this section is reprinted with permission from ‘*Experimental and numerical investigation of the thermal behaviour of polylactic acid during the fused deposition process*’ by Xunfei Zhou, Sheng-Jen Hsieh & Yintong Sun Virtual and Physical Prototyping Vol 12:3 pp. 221- 233 (2017) and *Modelling and estimation of tensile behaviour of polylactic acid parts manufactured by fused deposition modelling using finite element analysis and knowledge-based library*’ by Xunfei Zhou, Sheng-Jen Hsieh & ChenChing Ting Virtual and Physical Prototyping (2017). Copyright 2018 by Taylor & Francis Group

Where T is temperature, subscript E stands for extrusion, t is time, and other terms are defined based on the appendix of the original paper [28].

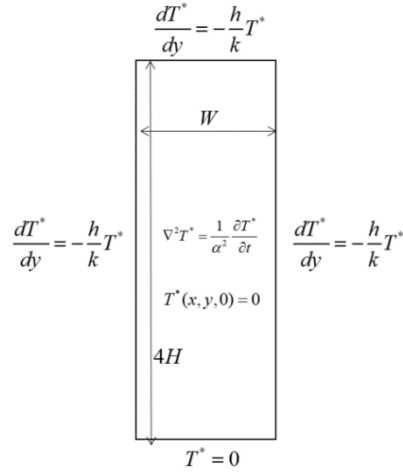


Figure 3 A schematic of the model used by Rodriguez

However, Eq. 2.1 neglected heat transfer effect from the platform that could happen during the deposition process. Yardimci et al. [29] developed a more general 1D heat transfer analysis model where the governing equation is

$$\rho \frac{\partial q}{\partial t} = k \frac{\partial^2 T}{\partial x^2} - \left(\frac{h}{h_{eff}} (T - T_{\infty}) \right) - \frac{k}{W^2} (T - T_{neigh}) \quad (2.2)$$

where ρ, q, k, h, h_{eff} stands for density, specific enthalpy, heat conductivity, convective heat transfer coefficient, and the ratio of road element volume to surface area

for convective cooling, respectively. Subscript ∞ denotes ambient condition while neigh denotes relevant neighbor road. Nevertheless, an analytical solution is difficult to obtain with various terms in Eq. 2.2 remain unknown.

Bellehumeur's research group [30, 31] tried to simplify Eq. 2.2 to a single road structure where lumped capacitance method could apply. With no neighbor roads and assumes heat capacity and conductivity remain constant, the third term on the right side can be neglected and becomes

$$\rho C_p A \frac{\partial T}{\partial t} = Ak \frac{\partial^2 T}{\partial x^2} - A \left(\frac{h}{h_{eff}} (T - T_\infty) \right) \quad (2.3)$$

After rearrangement of terms, Eq. 2.3 becomes

$$\rho C_p A \frac{\partial T}{\partial t} = Ak \frac{\partial^2 T}{\partial x^2} - hP(T - T_\infty) \quad (2.4)$$

where A is the cross-section area and P is the perimeter of it. Solving Eq. 2.4 with the boundary conditions of $T = T_E$ @ $x = 0, t \geq 0$ and $T = T_\infty$ @ $x = \infty, t \geq 0$, the solution would be

$$T = T_\infty + (T_E - T_\infty) e^{-mx} \quad (2.5)$$

with $m = \frac{\sqrt{1 + 4\alpha\beta} - 1}{2\alpha}$, $\alpha = \frac{k}{\rho C_p v}$, and $\beta = \frac{hP}{\rho C_p A v}$.

Costa et al. [32] further derived the analytical model for a multi-filament structure based on the governing equation of

$$\rho C_p A L \frac{\partial T}{\partial t} = -h A_{conv} (T - T_\infty) - \phi h A (T - T_\infty) - \sum_{i=1}^5 h_i A_i (T - T_i) \quad (2.6)$$

where L is the length of the filament, $A_i (i = 1 - 5)$ is the area of contact, subscript 2 stands for in contact with the building platform while other subscripts are in contact with neighbor filaments, as indicated in Figure 4. A_{conv} is the area exposed to ambient air, equals to total surface area minus every other area of contact. ϕ is 1 if the analyzed filament is the first one, if otherwise it becomes 0.

It should be seen that all theoretical models addressed the manufacture condition with underlying assumptions that failed to consider phase transition heat generation/loss into their heat transfer governing equation. Moreover, for an actual multi-filament structure, they are either unable to obtain the solution [27, 29-31] or require additional computer-aided computation[32].

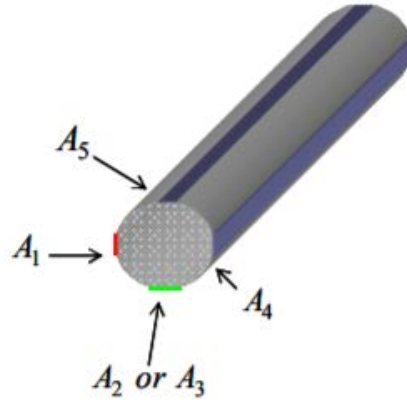


Figure 4 A schematic of contact area of a single filament [32]

2.1.2. Numerical simulation model

Numerical simulation of the thermal behavior of the deposition process in FDM was performed by several groups. Zhang and his coworkers [33, 34] developed a finite element analysis (FEA) model to study the effect of scan speed, road width, and layer thickness on part distortion. The simulations are performed in a stepwise thermo-mechanical manner where elements were gradually added/activated. The initial temperature of any newly activated element was set at the extrusion head temperature and the temperature evolution after extrusion was solved through conduction with the

⁴ Figure 4 is reprinted with permission from Costa, S. F., Duarte, F. M., & Covas, J. A. (2008). *Towards modelling of Free Form Extrusion: analytical solution of transient heat transfer*. *International Journal of Material Forming*, 1(1), 703-706. Copyright 2018 by Springer

neighbor elements and the building platform as well as the convection with ambient air. They discovered through the developed model that the scan speed is the most significant factor affecting part distortions, followed by the layer thickness and road width. Their results were validated with experimentally results only qualitatively. Some other research groups [35, 36] employed a similar technique to evaluate the temperature evolution in the FDM process. In particular, Zhang et al. [37] proposed an adaptable three-dimensional transient mathematical model with a boundary adjusting finite difference method. the FDM process was viewed as sequential deposition of elements following a predefined pattern at time intervals. Their model is able to adjust the boundary area and condition with the deposition of each element. They found out temperature settings, including temperature of printing nozzle, heat plate and the environment, are crucial factors determining temperature variation.

Costa et al. [38] examined the contribution of convection and radiation with the environment as well as the conduction inside of the product to the overall heat transfer effect. The mesh was generated for each individual filament with a circular cross-section shape with the deformation of a filament subjected to its own weight considered. They concluded that the highest impact of heat transfer was coming from thermal convection between the product and the environment, followed by heat conduction between adjacent filaments and the platform.

Dabiri et al. [39] presented fully resolved numerical simulations of the deposition of a filament of hot, viscous liquid, and its solidification process. The method was initially developed for direct numerical simulations of gas-liquid flow, but they successfully applied it to filament extrusion process. They simulated the injection of a hot viscous liquid onto a vertical plate where a Lagrangian front is used to track the surface of the injected melt. After contact with cooler building platform and previously deposited material, the melt cooled down and solidified, a zero velocity was then enforced on the cells which are the cells inside the injected material with the temperature below the melting point.

Despite various approaches, their simulation results either completely lack validation with experimental results [35-39], or they were validated with indirect results of the thermal behavior, such as dimension accuracy [33].

2.2. In-process monitoring techniques

As introduced above, the development of in-process monitoring techniques would be beneficial for cross-validation with transient predictive model results and improvement of advanced schemes. The primary research interest in this area was focused on the temperature profile and the geometry.

2.2.1. Embedded thermocouples

Embedded thermocouples become the natural choice of temperature measurement method. The temperature profiles of extruded filaments were monitored using 0.0118

mm K-type thermocouple in Sun et al.'s work [24]. One thermocouple was embedded in the foam of the base plate of the FDM 2000 machine and layers of filaments were deposited onto it. The temperature profiles they obtained showed that the temperature of the filament located on the bottom layer periodically rises above the glass transition temperature with the deposition of each additional layer. However, their conclusion can only apply to the specimen geometry they discussed, and their results were impacted by the response time of thermocouple. Kousiatza et al. [40] also deployed thermocouples to measure the temperature variation during the building process. Instead of embedding thermocouples in the building platform, they paused the manufacturing process in the middle, deployed thermocouples on top of the finished layer, and then continue manufacturing. The experimental results obtained in their study were compared against the prediction results generated by finite element analysis model, showing a good agreement. Monzon et al. [41] deployed two thermocouples on the axis of the rectangular samples. With only the bottom layer is in direct contact with the thermocouples, a progressive decrease of peak temperature was observed when the nozzle passed over the deployed sensors.

Based on the above discussion, the thermocouple is a valuable temperature measurement device suitable for characterizing temperature of a few fixed points. However, the requirement of pausing the manufacturing process in the middle to deploy temperature sensors and the difficulty of removing them from the manufactured part limited the application of it to industry-level process monitoring.

2.2.2. Infrared thermography

2.2.2.1 Theoretical background

Infrared (IR) imaging [42], also can be called as thermography, is a technique that could capture the radiative energy emitted by objects and transform such energy into a temperature distribution by using an infrared camera or sensor [43]. Thermography can be categorized into two types--active and passive thermography. If no external energy is provided to the object under study, then the technique is called passive thermography, on the contrary, active thermography requires using an external heat source to generate temperature variation to the object under study. Several parameters and factors that could impact the temperature measurement results of modern IR camera systems are listed in Table 1.1 of Vollmer et al.'s book [44]. Among them, quantitative results can strongly depend on the emissivity of the object, distance of the camera to the object, size of the object, and ambient temperature.

Emissivity is the efficiency with which an object emits infrared radiation when compared with a perfect emitter-blackbody, which has an emissivity value of 1. The relationship between total radiation intensity (all wavelengths) and the temperature is defined by the Stefan-Boltzmann law.

⁵ Part of this section is reprinted with permission from Zhou, X., Hsieh, S. J., Peng, B., & Hsieh, D. (2017). *Cycle life estimation of lithium-ion polymer batteries using artificial neural network and support vector machine with time-resolved thermography*. *Microelectronics Reliability*, 79, 48-58. Copyright 2018 by Elsevier

$$Q = \varepsilon \sigma T^4 \quad (2.7)$$

Where Q is radiation intensity, ε is emissivity, and σ is Stefan-Boltzmann constant.

However, targets are not perfect radiators in reality which usually have an emissivity value below 1. For these targets, the temperature was measured from a combination of emitted, reflected, and transmitted radiation, as shown below.

$$\begin{aligned} W_{tot} &= E_{object} + E_{reflection} + E_{atmosphere} \\ &= \varepsilon_{obj} \tau_{atm} \sigma T_{obj}^4 + (1 - \varepsilon_{obj}) \tau_{atm} \sigma T_{ref}^4 + (1 - \tau_{atm}) \sigma T_{atm}^4 \end{aligned} \quad (2.8)$$

where W_{tot} is the total radiation received by the camera, τ_{atm} is the transmittance of the atmosphere. The detailed derivation process of Eq. 2.8 can be found in Usamentiaga's review paper [45]. Rearrange Eq. 2.8, it becomes:

$$T_{obj} = \sqrt[4]{\frac{W_{tot} - (1 - \varepsilon_{obj}) \tau_{atm} \sigma T_{ref}^4 - (1 - \tau_{atm}) \sigma T_{atm}^4}{\varepsilon_{obj} \tau_{atm} \sigma}} \quad (2.9)$$

Therefore, the following parameters must be supplied to calculate the surface temperature of object: the emissivity of the object ε_{obj} , the reflected temperature T_{ref} , the transmittance of the atmosphere τ_{atm} , and the temperature of the atmosphere T_{atm} . τ_{atm} is generally estimated using the distance from the object to the camera and the relative humidity and usually very close to one. The temperature of the atmosphere can be obtained easily through the thermometer. However, as the emittance of the

atmosphere is very close to zero ($1 - \tau_{atm}$), this parameter has little influence on the temperature measurement results. Alternatively, the emissivity of the object and the reflected temperature have a very high influence on the temperature measurement and must be measured very accurately.

2.2.2.2 Application of thermography on FDM

Thermography has the advantages of being non-intrusive, with fast response time, and it can provide temperature mapping of the entire surface. Hence, the application of it on AM technologies, especially FDM has been widely studied. Dinwiddie et al. [46, 47] used both mid-wave and long-wave IR cameras to measure various temperature profiles in thermoplastic parts. Two different FDM machines were involved in their study, one is desktop-level and another is Big Area Additive Manufacturing (BAAM) machine. They found out adding carbon fibers to Acrylonitrile Butadiene Styrene (ABS) increases the extruder temperature and kept the deposited layer hot for a long time for both machines. Seppala and Migler [48] utilized a mid-wave IR camera in conjunction with reflection correction and calibration techniques to measure the temperature profiles of the extrusion region during 3D printing. Since the total signal received by the camera composed of emitted and reflected energy from the object, reflected energy was subtracted to increase the measurement accuracy. It is found the reflected energy can be determined by passing the heated extruder over the build surface without extruding so that the reflection correction could then be performed. Based on their results, It is discovered the extruded material of their sample remained above the glass transition

temperature for approximately 1s. Compton et al. [49] performed a thermal analysis of a large-scale thermoplastic polymer composites during the manufacturing process. They placed one IR camera 1.2m away from a 1.542m length, 0.358m height composite wall to monitor the temperature evolution.

However, there are still several difficulties associated with industrial applications of thermography as an in-process monitoring method. First and foremost, the field of view is limited for a fixed camera. For a stationary camera, the field of view could be easily obscured by a mounted nozzle and finished layer; therefore, observing inner surface temperatures would be difficult [50]. Second, the price of an infrared camera is usually too high for widespread application to commercialized 3D printers. For example, the FLIR SC-7600 mid-wave IR camera used in the study of Dinwiddie et al. [47] costs around \$2000, which is twice the price of a typical desktop-level 3D printer. Therefore, it is essential to develop a low-cost monitoring technique for in-process surface temperature measurements and the monitoring of thermal behavior.

2.2.3. Other techniques

An FDM process is prone to create over-fills and under-fills in the manufactured parts. Therefore, a high-level monitoring technique is required to detect those geometry defects and increase the reliability of the machine. Fang et al. [23, 51] deployed an optical camera to capture the image of each layer after it is built. The captured image was then compared with the expected image to identify any existing defects. Similar work was

done by Baumann and Roller [52], where they placed a camera in front of the machine to detect detachment, missing material flow, parts deformation, surface error, and deviation from the model. Cheng and Jafari [53] applied a 3-D surface reconstruction algorithm called shape from profile to obtain 3D road shapes. Their vision module is able to calculate surface defects and then fed them to a control module to adjust process parameters in order to improve surface quality for the subsequent layers, as well as subsequent parts.

Wu et al. [25] proposed to use acoustic emission (AE) technique to monitor FDM machine condition. The AE sensors were securely attached on the side surface of the extruder with vacuum grease. so that it could detect the stress waves generated from the source of emissions, such as crack, friction, and deformation. Stress wave signatures from the extruder were collected when the extruder was functioned normally, blocked, and semi-blocked. With the use of machine learning technique, they reached over 95% accuracy when detecting extruder blockage.

Kantaros and Karalekas [54] embedded an optical sensor with a short fiber Bragg grating (FBG) at the midplane of FDM built specimens to record developed residual strains. A similar pause-embed-continue scheme as Ref. [40] was used to embed the sensors in the middle of a printing process. The stress results were then used to assess the effect of printing orientation and layer thickness.

Rao et al. [55] conducted online monitoring involved a sensor network including thermocouples, accelerometers, an IR temperature sensor, and a real-time miniature video borescope. The information they could obtain is platform temperature, extrusion temperature, ambient temperature, melt pool temperature, extruder vibration, table vibration, and video.

2.3. FDM process design

2.3.1. Process parameters

In FDM, it is essential to select process parameters for achieving optimal product quality [56]. Usually, the desired process parameters are determined based on the operators' experience or manufacturer's recommendations. Nevertheless, it does not ensure that the selected process parameters would fabricate products with the optimal or near optimal performance for that specific machine and material. Furthermore, determining optimal parameters in an FDM process is complicated due to the presence of multiple conflicting parameters that will contribute to the final part quality and mechanical properties [57].

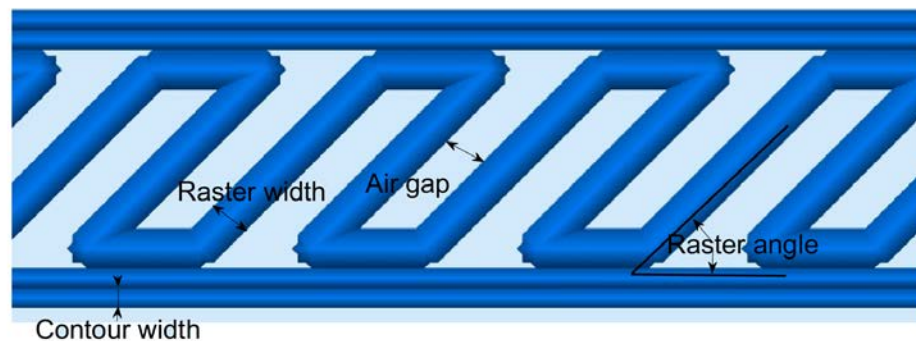


Figure 5 An illustration of process parameters

FDM process parameters can be categorized into product parameters and machine parameters. Product parameters determine how the 3D model get sliced or the geometry of the filament inside of a manufactured product. Some vital product parameters are listed and explained below, an illustration of them was also given in Figure 5.

- ❖ Contour width: Sometimes referred to the perimeter width, is the width of the outside bead.
- ❖ Raster/infill/extrusion/road width: The width of the infill raster material bead. The nozzle of larger diameter extrudes broader raster and vice versa. For a 0.4mm diameter nozzle, a maximum of 0.5mm raster width can be used.
- ❖ Air gap: To reduce the material cost and manufacturing time, the infill of each layer is not always pure solid. The air gap is defined as the distance between adjacent rasters of the same layer. In most 3D printing software, the setting of the air gap is done by changing infill density or infill percentage.
- ❖ Raster angle/infill angle: It is defined as the angle of infill bead with regards to the horizontal axis of the bottom layer. Raster angle determines how much material is there in the direction of force.
- ❖ Layer/wall thickness or layer height: Thickness of each layer. As FDM is a layer-by-layer manufacture process, layer thickness plays an important aspect in final product quality. The lower the value, the thinner each layer is, the better surface

quality can be achieved. However, decreasing the layer thickness also means more layers will be needed to be printed and the manufacturing time would increase proportionally.

- ❖ Infill pattern: Raster tool path inside of each layer. When using any infill percentage, a pattern is required to create a durable and robust structure inside each layer. There are several different infill pattern options, each has their unique advantages and disadvantages between mechanical strength, manufacturing time, and material cost. Some examples are rectilinear, triangular, and honeycomb structures, as illustrated in Figure 6.

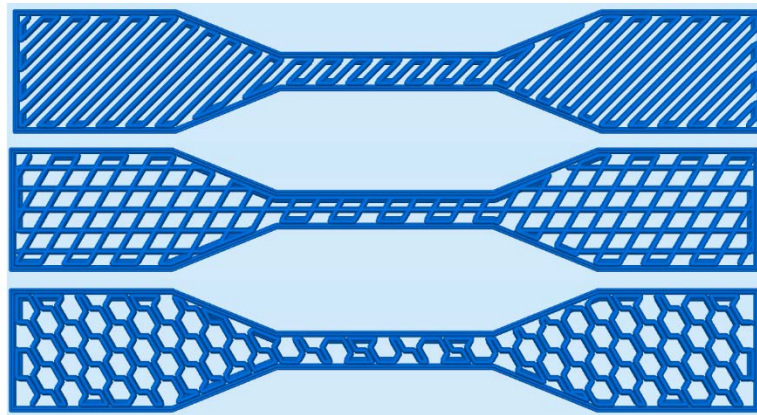


Figure 6 Structures of rectilinear, triangular, and honeycomb infill patterns

FDM machine parameters determine the extrusion condition of the filament, mostly temperature, and speed. Below is an explanation of each individual parameter.

- ❖ Extrusion/nozzle/die temperature: The temperature of the heated extruder. It is evident that the temperature of the filament near the exit of extruder should be close to this value. However, when the filament is leaving the nozzle tip, the temperature of it would be already cooled below this value. Correct setting of extrusion temperature is of immense importance. If the extrusion temperature is too high, the material may not have enough time to solidify before it gets in contact with the below structure, leaving a blob in the manufactured part. If it is set too low, then too much force would be required to extrude, leading to rough surface quality.
- ❖ Platform/envelop/bed temperature: The temperature of the building platform. A heated platform increases the temperature of lower layers, reduced the vertical temperature gradient and residual stress over the printing process, and thus prevent severe part deformation. However, if the platform was over-heated, the material could stay above its glass transition temperature for a longer time and would continue shift/flow when in contact with the bed and thus influence the dimension accuracy.
- ❖ Printing speed: The speed nozzle is moving while extruding the filament to create the physical representation of the 3D model. Printing too fast could cause the material to cool quickly and create a large temperature gradient in the horizontal direction while printing too slow would increase the manufacturing time significantly.

2.3.2. Influence of process parameters on dimensional accuracy

Wang et al. [58] studied the effect of layer thickness, deposition style, support style, deposition orientation, and deposition position on each direction of dimension accuracy and mechanical strength by combining the Taguchi method with the Gray relational analysis. They concluded that an essential parameter to dimensional accuracy is the fused deposition layer thickness. With a mathematical model of the prototype warp deformation constructed, Wang et al. [17] investigated the effect of deposition layers number, the stacking section length, the chamber temperature, and the material linear shrinkage rate on part deformation value quantificationally. Sood et al. [59, 60] conducted investigations on the influence of part orientation, layer thickness, raster width, raster angle and air gap along with their interactions on the dimensional accuracy of FDM manufactured parts. Their results showed there are large numbers of conflicting factors independently or in interaction with others that could influence the dimensional accuracy, of which layer thickness played the most crucial role. Xinhua et al.[61] examined the effect of layer thickness, printing speed, extrusion temperature, filling style, raster width on the distortion of polylactic acid (PLA) thin-plate part. Their results showed the highest distortion of PLA thin-plate part occurs at four corners, and the dimension of the part is an essential factor for the distortion. It is concluded designing large dimension and thin part should be avoided in the practical application. Mohamed et al. [62] explained the optimization method of FDM process parameters using I-optimality criterion. It is found out thickness deformation increases with an increase in

layer thickness and number of contours from low to high level. In comparison, thickness deformation decreases with the increase in the air gap, raster angle, build orientation, and road width. Nancharaiah et al. [63] used the Taguchi method to identify the key factors (layer thickness, road width, raster angle and air gap) that influence dimension accuracy of FDM parts. From the design of experiments and ANOVA analysis, it was found that layer thickness and road width affected the surface quality and part accuracy significantly. In Zhang et al.'s work [64, 65], parameters such as line width compensation, extrusion velocity, filling velocity, and layer thickness are selected as input variables, while dimensional error, warp deformation, and built time were selected as output responses to optimize the FDM process. They discovered that the most significant influence on the performance indexes is line width compensation, followed by extrusion velocity, layer thickness, and filling velocity.

In Table 1, the effect of process parameters on dimension accuracy in the previous work were reviewed, where \nearrow stands for increasing of the corresponded parameter would increase distortion in the vertical direction and reduce dimension accuracy and \searrow denotes the contrary condition. It can be seen that most of the previous work were focused on product/geometry parameters while machine parameters were rarely considered. In addition, ABS received most of the attention while PLA, another popular material candidate in the industry was hardly examined. Lastly, different works have controversial conclusion regarding the effect of raster angle and width. This discrepancy can be explained by the effect of other fixed factor but need further investigation.

Table 1 The relationship between process parameters and increasing of vertical deformation

Ref.	Material	Layer thickness	Infill density	Raster width	Raster angle	Extrusion temperature	Platform temperature	Printing speed
[58]	ABS	↗				270	75	
[17]	ABS	↗				270	↘	
[59] [60]	ABS	↗	↗	↘	↗			
[61]	PLA	↗		↗		↗		↘
[62]	PC-ABS blend	↗	↗	↘	↘			
[63]	ABS	↗	↗	↘	↘			
[64, 65]	ABS	↗						↗

2.3.3. Influence of process parameters on tensile strength

With the booming FDM industry, the determination of the mechanical strength of manufactured parts, especially tensile strength, by process design has become especially intriguing in the 21st century [66]. In 2000, Es-Said et al. [67] conducted tensile testing experiments on ABS specimens with various raster angles. They found out the tensile properties of the ABS samples varied with different orientations, with the highest ultimate and yield strengths in the 0° orientation, the direction where the tensile force applied. Since then, the effect of building orientation on tensile strength has been extensively investigated [68-70], and multiple research groups have concluded that raster direction coinciding with the direction of force improves tensile strength. Another early work conducted by Ahn et al. [71] applied a two-level experimental design, and the effects of air gap, bead width, model temperature, ABS color, and raster orientation on tensile strength were examined and confirmed. Subsequently, Sood et al. [72] concluded that layer thickness, orientation, raster angle, raster width and air gap also influenced the tensile performance of the FDM ABS prototype. They found that small raster angles

were not preferable because a long raster would be generated, which increased stress accumulation along the direction of deposition, resulting in more distortion and, therefore, weak bonding. They indicated that a non-zero air gap causes a flow of material towards the adjacent layers through the gap, increasing the bonding surfaces and causing the strength to improve with gap width. However, their conclusions were contradicted by those of other research groups. Masood et al. [73] performed similar experiments with the input parameters of air gap, raster width, and raster angle and showed the interaction of process parameter is complicated that the trend of tensile strength over one single parameter behaves differently on several levels of other parameters. Hossain et al. [74] focused on how modifying process parameters, such as build orientation, raster angle, contour width, raster width, and air gap, could improve the tensile strength of ABS specimen. They used the insight revision method, a visual feedback method that continues to reduce the air gap between adjacent rasters by tweaking other parameters. Similarly, Nidagundi et al. [75] considered layer thickness, raster angle, and orientation for tensile strength optimization, while Onwubolu and Rayegani [76] investigated layer thickness, part orientation, raster angle, raster width, and air gap on the tensile strength of test specimen. In contrast to investigations of ABS, Tymrak et al. [77] tested PLA specimens with various layer heights and building orientations. Their results indicated that desktop-level parts manufactured by FDM machines have comparable tensile strength and elastic moduli to those printed on commercial 3D printing systems. Recently, Chacón et al. [78] tried to characterize the

effect of build orientation, layer thickness and feed rate on the mechanical performance of PLA samples manufactured with a low-cost 3D printer. They discovered for flat printed samples, the variations of maximum tensile strengths were marginally significance, while a very small layer thickness value (0.06mm) usually resulted in high tensile and flexural strength.

Similar to Table 1, Table 2 listed of how these process parameters affect the tensile strength of FDM manufactured parts, based on the summarized previous work, where ↗ denotes a positively correlation and ↘ indicates a negative correlation. It is demonstrated that the effects of process parameters were not uniform across the results from multiple research groups, and this discrepancy can be explained by the interaction between the investigated parameters and other processing conditions. For example, Chacón et al. [78] discovered that for the effect of layer thickness on the mechanical properties due to the build orientation was different for upright samples (layers were deposited perpendicular to the pull direction) and flat samples (the fused filament deposition is positioned in the same direction as the pull direction). Similarly, the study of Masood et al. [73] demonstrated that UTS of polycarbonate (PC) is negatively correlated with raster angle for raster width of 0.4064 mm and 0.6064 mm, where as in case of raster width of 0.8314 mm, the tensile strength increased with raster angle. Regarding the materials, PLA has advantages over ABS in structural stability and lower sensitivity to environmental conditions [79], but the mechanical behavior has not been

extensively studied [80], suggesting that further investigations are needed to improve understanding of the mechanical behavior of 3D-printed components using PLA.

Table 2 The relationship between process parameters and increasing of tensile strength

Ref.	Material	Layer thickness (mm)	Infill density	Raster width (mm)	Raster angle	Extrusion temperature
[71]	ABS		↗	↘	↘	↗
[72]	ABS	↘ then ↗	↗	↘	↗	
[74]	PC				↘	
[76]	ABS	↘	↗	↘	↗	
[75]	ABS	↘ then ↗			↘	
[77]	PLA	↘ then ↗				
[78]	PLA	↗ then ↘				

2.4. Modeling of mechanical strength of FDM manufactured parts

2.4.1. Conservative isotropic model

Although it is known that FDM manufactured parts showed anisotropic behaviors when subject to external force, it is the simplest way for the manufacturer to represent their material with an isotropic material model. With uniform material properties in all directions, Hooke's law in compliance format applies that define the stress-strain behavior for a 3D object

$$\boldsymbol{\varepsilon} = \mathbf{C}\boldsymbol{\sigma} \quad (2.10)$$

where $\boldsymbol{\sigma}$, \mathbf{C} , $\boldsymbol{\varepsilon}$ stands for stress, the compliance matrix, strain, respectively. Writing Eq.

2.10 in matrix form, it becomes

$$\begin{bmatrix} \varepsilon_{xx} \\ \varepsilon_{yy} \\ \varepsilon_{zz} \\ \gamma_{xy} \\ \gamma_{yz} \\ \gamma_{zx} \end{bmatrix} = \begin{bmatrix} \frac{1}{E} & -\frac{\nu}{E} & -\frac{\nu}{E} & 0 & 0 & 0 \\ -\frac{\nu}{E} & \frac{1}{E} & -\frac{\nu}{E} & 0 & 0 & 0 \\ -\frac{\nu}{E} & -\frac{\nu}{E} & \frac{1}{E} & 0 & 0 & 0 \\ 0 & 0 & 0 & \frac{1}{G} & 0 & 0 \\ 0 & 0 & 0 & 0 & \frac{1}{G} & 0 \\ 0 & 0 & 0 & 0 & 0 & \frac{1}{G} \end{bmatrix} \begin{bmatrix} \sigma_{xx} \\ \sigma_{yy} \\ \sigma_{zz} \\ \tau_{xy} \\ \tau_{yz} \\ \tau_{zx} \end{bmatrix} \quad (2.11)$$

where γ , G , τ stands for shear stress, the shear modulus, shear strain, respectively.

With the modulus of elasticity E and Poisson's ratio ν known, it is possible to calculate the stresses at a given strain. In particular, if the material body was subjected to uniform stretching along the x-direction, the condition of tensile testing, only stress in the x-direction is non-zero, $\sigma_{xx} = P = F / A$. Then the strain in x-direction becomes: $\varepsilon_{xx} = \sigma_{xx} / E$. In the material specification sheet provided by Stratasys [81], usually, only the maximum stress is given, which is a conservative value.

2.4.2. Orthotropic constitutive model

It is possible to develop a constitutive model with orthotropic properties, which has the modulus of elasticity, the shear modulus, and Poisson's ratio defined in all directions.

Under such an assumption, Eq. 2.11 is converted to [82]

$$\begin{bmatrix} \varepsilon_{xx} \\ \varepsilon_{yy} \\ \varepsilon_{zz} \\ \gamma_{xy} \\ \gamma_{yz} \\ \gamma_{zx} \end{bmatrix} = \begin{bmatrix} \frac{1}{E_x} & -\frac{\nu_{xy}}{E_x} & -\frac{\nu_{xz}}{E_x} & 0 & 0 & 0 \\ -\frac{\nu_{yx}}{E_y} & \frac{1}{E_y} & -\frac{\nu_{yz}}{E_y} & 0 & 0 & 0 \\ -\frac{\nu_{zx}}{E_z} & -\frac{\nu_{zy}}{E_z} & \frac{1}{E_z} & 0 & 0 & 0 \\ 0 & 0 & 0 & \frac{1}{G_{yz}} & 0 & 0 \\ 0 & 0 & 0 & 0 & \frac{1}{G_{xz}} & 0 \\ 0 & 0 & 0 & 0 & 0 & \frac{1}{G_{xy}} \end{bmatrix} \begin{bmatrix} \sigma_{xx} \\ \sigma_{yy} \\ \sigma_{zz} \\ \tau_{xy} \\ \tau_{yz} \\ \tau_{zx} \end{bmatrix} \quad (2.12)$$

In this way, nine independent constants are required to define the material model completely. However, this approach has a few limitations [83]. The derived model is only valid for a specific set of process parameters. With the changing of building parameters such as raster angle and infill density, previous literature already demonstrated that the mechanical behavior of the parts would change significantly. Moreover, this model does not consider the usually inter-layer behavior of FDM manufactured parts. This model considered the part as a bulk material with different properties other than its raw material while neglecting the bonding formation across layers. Under complex loading conditions, this model is unlikely to perform well.

2.4.3. Laminar composite model

A laminate is an organized stack of unidirectional composite plies, where all fibers in each layer in the same direction. An FDM manufactured product has a structure very

similar to laminar composite, while each layer could have their unique but uniform properties inside of each one. The difference is composite materials are bounded together in a solid body by some type of binding medium called matrix binder, while a layer-by-layer manufactured product is bound together through sintering filaments [31]. With Q defined as the stiffness matrix, the in-plane stress for a thin laminar is defined as

$$\begin{bmatrix} \sigma_{xx} \\ \sigma_{yy} \\ \tau_{xy} \end{bmatrix} = \begin{bmatrix} Q_{xx} & Q_{xy} & 0 \\ Q_{yx} & Q_{yy} & 0 \\ 0 & 0 & Q_{ww} \end{bmatrix} \begin{bmatrix} \varepsilon_{xx} \\ \varepsilon_{yy} \\ \gamma_{xy} \end{bmatrix} \quad (2.13)$$

So that it only requires the modulus of elasticity on two directions, major Poisson's ratio, and the shear modulus to define. In the classical laminated plate theory, all three transverse strain components are zero and assume a linear distribution of strain in the thickness direction [84]

$$\begin{bmatrix} \varepsilon_{xx} \\ \varepsilon_{yy} \\ \gamma_{xy} \end{bmatrix} = \begin{bmatrix} \varepsilon_{xx}^0 \\ \varepsilon_{yy}^0 \\ \gamma_{xy}^0 \end{bmatrix} + z \begin{bmatrix} k_{xx} \\ k_{yy} \\ k_{xy} \end{bmatrix} \quad (2.14)$$

where z is half thickness, k is bending/twisting curvatures in the lamina, superscript 0 indicates nominal stress in mid-plane.

2.5. Optimization with the application of FDM

The purpose of this section is to discuss the role that can be played by optimization technique in additive manufacturing process, specifically the FDM process. When talking about FDM optimization, it could be referring to either topology optimization or process parameter optimization. The former is aimed to optimal distributing of the material of each layer within a given volume to reduce material weight and increase mechanical strength. The later has a broader scope, focuses on optimal all process parameters to ensure quality of the product, increase strength, improve dimensional accuracy, and reduce material cost and manufacturing time. To review the previous work on process parameter optimization, the generalized form of parametric optimization would be first introduced, followed by description of a few important optimization techniques, then in the end, advantages and disadvantages of most recent work on the FDM process parameter optimization would be presented.

2.5.1. Parametric optimization

As introduced in Section.1, the incorporation of sensors is not achievable with black box controllers currently used in additive manufacture machines, therefore almost every FDM machine adopts open-loop control. The setting of manufacturing conditions would be constant throughout the whole process, resulted in a static system where stochastic parametric (static) optimization problem applies. The general form of static optimization problem is:

$$\left. \begin{array}{ll} \text{Maximize/Minimize } f_p(\mathbf{x}), & p = 1, 2, \dots, P \\ \text{subject to } h_j(\mathbf{x}) = 0, & j = 1, 2, \dots, J \\ g_k(\mathbf{x}) \leq 0, & k = 1, 2, \dots, K \\ \mathbf{x}_{\min} < \mathbf{x} < \mathbf{x}_{\max} \end{array} \right\} \quad (2.15)$$

The objective is to find a set of parameters $\mathbf{x} \in \mathbb{R}^n$ that could optimize (maximize or minimize) the objective functions $f_p(\mathbf{x})$. With the background of FDM, parameters \mathbf{x} could be extrusion temperature, platform temperature, infill pattern and so on, and they are usually discretized into several levels instead of continuously change. To solve this problem, multiple approaches has been developed so far, which would be reviewed in the next subsection.

2.5.2. *Methods of parametric optimization*

Due to the nature of discrete optimization problem with the background of FDM, gradient-based optimization techniques such as gradient descent or simultaneous perturbation could not be applied. Therefore, three categories of optimization methods were introduced in this subsection: model-approximation methods (response surface method and artificial neural network), iteration-based methods (sequential approximate optimization), and meta-heuristics methods (genetic algorithm)

2.5.2.1 **Response surface method**

It should be noted prior to (or even after) perform optimization, the exact form of objective functions $f_p(\mathbf{x})$ would be unknown. Response surface method (RSM) is aimed

to “guess” the analytical structure of objective functions by constructing an approximated metamodel (surrogate model). RSM consists of several steps:

[1]. At first, sampling of the data points is performed to ensure a good representation of the studied design space was achieved

[2]. Then the response of those data points would be collected from the investigated model

[3]. When the coordinates and responses are known, regression or function fitting is performed

[4]. The goodness-of-fitting needs to be carried out to test whether the obtained surrogate model is indeed a good fit

[5]. The minima or maxima of the surrogate model is calculated through mathematical analysis

RSM offers the ability of mapping multidimensional fitting models and could provide interaction effects between parameters. However, RSM is highly dependent on selection of a proper fitting model. And with the increasing of dimensionality of input parameters, extensive experiments need to be performed, which may be time-consuming.

2.5.2.2 Neural network model ⁶

Unlike RSM trying to construct an explicit function to model the relationship between input parameters and output response, artificial neural network (ANN) model aims to build an implicit regression model. Finding a proper fitting function could be difficult for RSM when the problem is highly non-linear, but ANN has been demonstrated to be a good candidate to correlate such problems [85]. Typically, ANN model consists of multiple layers of interconnected linear or non-linear computing elements, called neurons. Those layers usually consist of one input layer, one output layer, and one or more hidden layers. There are many archetypes of a neural network, such as convolution neural network, recurrent neural network, and shallow neural network, while in this dissertation, a single layer shallow neural network was used [86].

Consider a series of input parameters and the evaluated response on those data points

$\{\mathbf{x}_i, \mathbf{y}_i\}, i = 1, 2, \dots, l$ in the $\mathbb{R}^n \times \mathbb{R}^p$ domain. With a network topology of $n-m-p$

topology shown in Figure 7, the j^{th} neuron in the hidden layer accepts n inputs

multiplied by its weight $w_{i,j}$ between two nodes plus a biased term b , produces a sum of

⁶ Part of this section is reprinted with permission from Zhou, X., Hsieh, S. J., Peng, B., & Hsieh, D. (2017). *Cycle life estimation of lithium-ion polymer batteries using artificial neural network and support vector machine with time-resolved thermography*. *Microelectronics Reliability*, 79, 48-58. Copyright 2018 by Elsevier

$$n_j = \sum_{i=1}^m w_{i,j} x_i + b = \mathbf{w}\mathbf{x} + b \quad (2.16)$$

Then a transfer function f , usually the sigmoid function, is applied to the weighted sum, generates its output to the output layer

$$a_j = f(\mathbf{w}\mathbf{x} + b) = \frac{1}{1 + e^{-(\mathbf{w}\mathbf{x} + b)}} \quad (2.17)$$

Then the same procedure repeats, and the estimated output would be equal to

$$f(\mathbf{w}_{out} \mathbf{a}_{out} + b_{out}) .$$

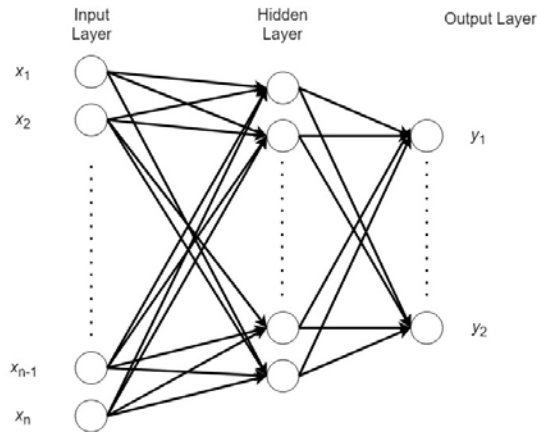


Figure 7 A typical non-linear neural network

ANN has two stages in its applications — training and testing. Under training stage, the algorithm would try to establish the relationship between inputs and known outputs.

While for the testing stage, the algorithm started to use established network to make

predictions based on unfamiliar inputs. After established the ANN model with sampled data, the optimum condition can be located through loop every possible combination of input parameters.

2.5.2.3 Sequential approximate optimization

The main principle of sequential approximate optimization (SAO) [87] is to decompose the optimization process into a sequence of cycles, where in each cycle the previous function space was restricted to a sub-region and searching optimum value is conducted inside of the generated sub-region. It is primarily used in single objective optimization where the steps to perform SAO can be explained in detail as:

[1].Set $k = 0$

[2].Sampling the original design space \mathbf{x} to a certain data points $\mathbf{x}_i^{(k)}$ $i = 1, 2, \dots, n$

[3].Evaluate the model response at $\mathbf{x}_i^{(k)}$ as $y_i^{(k)}$, change k to 1

[4].Construct a sub-region $r^{(k)}$ followed a specific region relocation strategy

[5].Sampling the sub-region design space to a certain data points $\mathbf{x}^{(k)}$

[6].Evaluate the model response at $\mathbf{x}^{(k)}$ as $y^{(k)}$

[7].Construct a surrogate model $S^{(k)}$ based on dataset $\{\mathbf{x}^{(k)}, y^{(k)}\}$

[8].Find the optimum condition of $S^{(k)}$ at $\mathbf{x}_{opt}^{(k)}$

[9]. Return to step 4 if stopping criterion not met, increase k by 1; otherwise, $\mathbf{x}_{opt}^{(k)}$ would be the final optimum condition

Following the steps above, in each iteration cycle, a sub-problem of optimization is created which is similar to RSM. Nevertheless, the difficulties of adopting SAO is to choose an appropriate region relocation strategy to ensure fast and reliable convergence of the algorithm. One possible strategy proposed in Jacobs et al.'s work [87] is to use $\mathbf{x}_{opt}^{(k)}$ as the center point of $r^{(k+1)}$ while the radius of the new sub-region can either be fixed or subject to change.

2.5.2.4 Genetic algorithm

The genetic algorithm (GA) is a meta-heuristic approach, where “heuristic” means to find by trial and error and “meta” means beyond or higher level. It has been inspired by the evolutionary phenomenon that species with the best mutation becoming dominant after successive generations – “survival of the fittest”. With the background of optimization, the data points with the worst response would be replaced by the mutations of data points with the best response after each iteration. A typical GA process is given below:

[1]. Set $k = 0$

[2]. Select a certain random data points $\mathbf{X}^{(k)} = \mathbf{x}_i^{(k)} \quad i = 1, 2, \dots, n$ from the original design space \mathbf{x}

[3]. Evaluate the model response at $\mathbf{x}_i^{(k)}$ as $y_i^{(k)}$, change k to 1

[4]. Compute the fitness value for each data point

[5]. Identify several best and worst fitness values with data point of $\mathbf{x}_{\text{best},j}^{(k)}$, $j = 1, 2, \dots, J$ and

$$\mathbf{x}_{\text{worst},l}^{(k)}, l = 1, 2, \dots, L$$

[6]. If stopping criteria not met, replace $\mathbf{x}_{\text{worst},l}^{(k)}$ by mutation and cross-over of $\mathbf{x}_{\text{best},j}^{(k)}$ in

$\mathbf{X}^{(k+1)}$, increase k by 1; otherwise, return the fittest data point as the optimal location.

Therefore, in each iteration of GA, the population or selected dataset is constantly updated by probabilistically selecting fitter individuals. The convergence rate of GA and the accuracy of solution highly depends on mutation and cross-over algorithms. Up to date, several mutation and crossover methods [88] have been proposed and each have their own strength and weakness.

2.5.3. Recent advance on optimization of the FDM process

The optimization of the FDM process has been conducted for over a decade and Mohamed et al. [57] already reviewed the research carried out until 2014. Therefore, the aim of this subsection is to continue reviewing the most recent study on FDM optimization and identified the research gap. The optimization method, material, model input parameters, and the targeted responses from several research articles have been summarized in Table 3. From Table 3, several limitations of the current optimization

methods should be noted. Firstly, the types of material used are limited to ABS and PLA. As indicated by Mohamed et al. [57], FDM machine liquefier and extruder is already compatible with other thermoplastics such as PC, poly- ether-ether-ketone (PEEK), elastomer and nylon-12, therefore, considerable work can be accomplished in this area. Secondly, a vast majority of the work heavily relies on experiments and most of them are DoE and ANOVA based. With DoE strategies that aimed to reduce experimental runs, such as Taguchi design and partial factorial design, the required dataset size is indeed reduced. Nevertheless, they also possessed the drawback of relatively low prediction accuracy and unable to perform multi-objective optimization [57]. Alternatively, if adopting a full factorial design to build RSM, the number of required experimental conditions would be extremely high.

Moreover, the experimental conditions for almost all the previous work were pre-determined. If the sampled conditions, or the designed condition could not well represent the response surface, then the accuracy of their derived solution would be questioned. Lastly, optimizing the process parameters for mechanical properties was the focus for most of the recent work published, while the investigation of thermal behavior and building time is very rare. Therefore, it is imperative to develop an optimization algorithm that could use low-fidelity but cost-effective numerical model to infer the surrogate model and its optimum solution, and iteratively, this model would be corrected with high-fidelity model by conducting experiment until searched the real optimum solution.

Table 3 Summary of most recent (2014-2018) work on FDM process optimization

Ref.	Material	Experimental or numerical	Method	Inputs	Outputs
[89]	PLA	Exp.	DoE with Taguchi L8, then ANOVA	Infill density, thickness, extrusion temperature, perimeter, printing speed, raster angle, and orientation	UTS, elastic modulus, critical stress intensity factor
[65]	PLA	Exp.	DoE with uniform U17, then RSM	Raster width compensation, printing speed, travel speed, and layer thickness	Dimensional error on three directions
[90]	PEEK	Exp.	DoE with Taguchi L9, then range analysis	Printing speed, layer thickness, printing temperature, and filling ratio	UTS, elastic modulus, elongation
[91]	PLA	Exp.	DoE with partial 11 runs, then ANOVA	Extrusion temperature, layer thickness, and layer-design	Intra- and inter-layer strength
[76]	ABS	Exp.	DoE with full factorial F32, then Group Method for Data Handling (GMDH) network	layer thickness, part orientation, raster angle, raster width, and infill density	UTS
[92]	ABS	Exp.	DoE with 20 runs, then ANOVA, then GA on ANOVA fitted functions	Infill density, horizontal orientation, and vertical orientation	Strength and volumetric shrinkage
[93]	ABS	Exp.	DoE with 86 runs, then RSM, then GA on RSM fitted functions	Raster width, orientation, raster angle, raster width, layer thickness, and infill density	Build time, support material volume, and model material volume
[94]	ABS	Exp. and Num.	DoE with 32 runs, then GA. Numerical model validated with 5 cases	Seven different internal topology parameters	Weighted response on part orientation
[95]	Nylon6–Al–Al ₂ O ₃	Exp.	DoE with central composite full unblocked design of 20 runs, then RSM and ANOVA	Composition, mean barrel temperature, and extrusion temperature	UTS and diameter variation

2.5.4. Surrogate-based optimization using multi-fidelity models

Using multi-fidelity models to perform optimization is not rare in the research field of FEA. As FEA requires discretize the continuous model into discrete counterparts, the size of the part/mesh is critically important. Although smaller mesh size could bring higher prediction accuracy, the computation time would also increase expediently, making surrogate models an attractive option. However, even with a proper DoE

strategy, constructing a surrogate model with high-fidelity model could still be expensive. Hence, the concept of surrogate-based optimization using multi-fidelity models (SBO-MFM) is to replace direct optimization of a high-fidelity model by an iterative response corrective process on a low-fidelity surrogate model. The framework of an SBO-MFM process is illustrated in Figure 8.

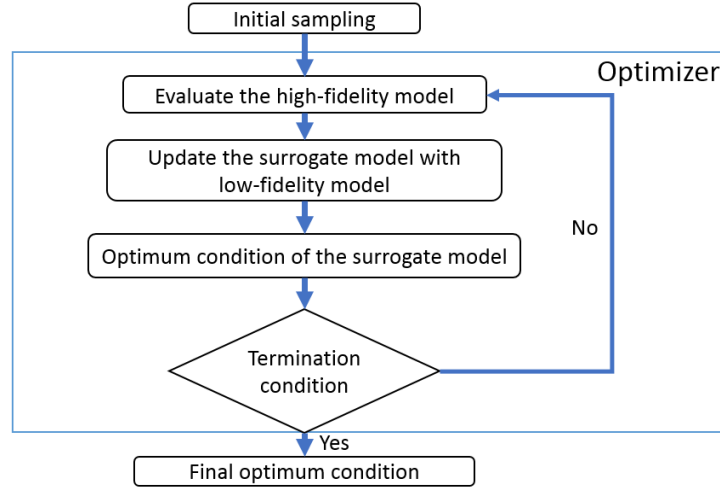


Figure 8 The flowchart of a typical SBO-MFM process

As indicated by Koziel et al. [96], the SBO-MFM problem can be formulated as:

$$\mathbf{x}^{(k+1)} = \arg \min(S^{(k)}(\mathbf{x})) \quad (2.18)$$

where $S^{(k)}(\mathbf{x})$ is the surrogate model constructed at the iteration number k . Several SBO-MFM algorithms have been developed so far, including:

- [1] Parametric response correction methods, also called deterministic methods, such as space mapping [97] and manifold mapping [98]
- [2] Non-parametric response correction methods, also called non-deterministic methods, such as adaptive response correction method [99] and cokriging-based sequential design method [100].

The difference between parametric response correction methods and non-parametric response correction methods is whether the correction term would be explicitly expressed in the analytical form. In the next section, two typical SBO-MFM algorithms, space mapping (SM) and adaptive response correction (ARC) would be reviewed.

2.5.4.1 Space mapping method

The principle of SM approach [97] is to exploit the speed of an efficient low-fidelity (LF) model and corrected it with a few slow but highly accurate high-fidelity (HF) model evaluations to effectively perform optimization. The implementation of this algorithm can be described as follows:

- [1].Set $k=0$, identify one reasonable data point $\mathbf{x}_{\text{initial}}^{(k)}$
- [2].Identify initial m HF model data points $\mathbf{x}_{\text{HF},i}^{(k)}, i = 1, 2, \dots, m$ in the vicinity of $\mathbf{x}_{\text{initial}}^{(k)}$
- [3].Evaluate their response in the HF model $\mathbf{R}_{\text{HF}}^{(k)} = R_{\text{HF},i}^{(k)}, i = 1, 2, \dots, m$

[4]. Find m LF model data points $\mathbf{x}_{\text{LF},i}^{(k)}$, $i = 1, 2, \dots, m$, so that their response

$\mathbf{R}_{\text{LF}}^k = R_{\text{LF},i}^k$, $i = 1, 2, \dots, m$ lies in the vicinity of \mathbf{R}_{HF}^k , which meet the criteria of

$$\|\mathbf{R}_{\text{HF}}^k - \mathbf{R}_{\text{LF}}^k\| \leq \varepsilon$$

[5]. Compute the transformation of $\mathbf{x}_{\text{LF},i}^{(k)} = P^{(k)} \mathbf{x}_{\text{HF},i}^{(k)}$, identify the optimum solution $\mathbf{x}_{\text{LF},\text{opt}}^{(k)}$

in the LF model

[6]. Calculate $\mathbf{x}_{\text{HF},m+1}^{(k)} = P_{-1}^{(k)} \mathbf{x}_{\text{LF},\text{opt}}^{(k)}$, where $P_{-1}^{(k)}$ is the inverse transformation of $P^{(k)}$

[7]. Evaluate the HF model response $R_{\text{HF},m+1}^k$ at the newly added point $\mathbf{x}_{\text{HF},m+1}^{(k+1)}$

[8]. Check the convergence criteria $|R_{\text{HF},m+1}^{(k)} - R_{\text{LF},\text{opt}}^{(k)}| \leq \varepsilon$; if met, then $\{\mathbf{x}_{\text{HF},m+1}^{(k)}, R_{\text{HF},m+1}^{(k)}\}$ is

the optimum condition; if not, $k = k + 1$, return to step 2, and add $\mathbf{x}_{\text{HF},m+1}^{(k)}$ to dataset

$$\mathbf{x}_{\text{HF},i}^k, i = 1, 2, \dots, m$$

The SM algorithm described above is a one-point additive technique since at each iteration, the HF model would be evaluated once. And in total, the HF model would be evaluated $m + k$ times. A few variations of SM technique have been developed so far, such as multi-point space mapping [101] and corrected space mapping [102]. However, space mapping techniques have their own limitation which is associated with the develop of transform function $P^{(k)}$. As indicated by Koziel et al. [99], the response may contain sharp minima corresponding to zeros of the transform function if the response is a highly non-linear function of the investigated parameters. In such cases, the

performance of the space-mapping algorithm may deteriorate with respect of both convergence rate and accuracy.

2.5.4.2 Adaptive response correction

ARC was introduced in 2009 [99] to alleviate the aforementioned difficulty of the standard SM algorithm. For ARC algorithm, in each iteration cycle, a correction term $\Delta_{\text{ARC}}^{(k)}$ is adaptively changed to compensate the difference between surrogate models developed on Multi-Fidelity Models. The details of one variation of ARC algorithm can be explained as follows:

[1]. Identify enough data points $\mathbf{x}_i^{\text{initial}}, i = 1, 2, \dots, n$ and evaluate their response

$R_{\text{LF},i}^{\text{initial}}, i = 1, 2, \dots, n$ in the LF model

[2]. Construct a surrogate model $S_{\text{LF}}^{\text{initial}}$ bases on $\{\mathbf{x}_i^{\text{initial}}, R_{\text{LF},i}^{\text{initial}}\}$ and set $k = 0$

[3]. Sampling m data points $\mathbf{x}_j^{(k)}, j = 1, 2, \dots, m$ from parameter space $\mathbf{x}^{(k)}$ with a proper DoE strategy

[4]. Evaluate the response of $\mathbf{x}_j^{(k)}$ from the the LF and HF models to obtain $\mathbf{R}_{\text{LF}}^{(k)}$ and $\mathbf{R}_{\text{HF}}^{(k)}$

[5]. Construct two surrogate models $S_{\text{LF}}^{(k)}$ and $S_{\text{HF}}^{(k)}$ based on $\mathbf{R}_{\text{LF}}^{(k)}$ and $\mathbf{R}_{\text{HF}}^{(k)}$, respectively

[6]. Compute the ARC correction term $\Delta_{\text{ARC}}^{(k)} = S_{\text{HF}}^{(k)} - S_{\text{LF}}^{(k)}$

[7]. Identify the current optimum point $\mathbf{x}_{\text{ARC,opt}}^{(k)}$ from the ARC surrogate model

$$S_{\text{ARC}}^{(k)} = S_{\text{LF}}^{\text{initial}} + \Delta_{\text{ARC}}^{(k)}$$

[8]. Check the convergence criteria; if met, then $\mathbf{x}_{\text{ARC,opt}}^{(k)}$ is the optimum point; otherwise, increase k by 1, update parameter space $\mathbf{x}^{(k)}$, and return to step 3

As illustrated in the above algorithm, the HF model is evaluated m times at each iteration toward a total of $m \times k$ times, while the LF model is evaluated $n + m \times k$ times. It is possible that the evaluation times of both HF and LF model could be further reduced with the developing of more advanced algorithm.

2.6. Summary

From the above literature review, it is evident that three approaches exist for the current research of the mechanical and thermal behavior of FDM manufactured product and they all have certain limitations.

For theoretical modeling of the process and product, over-simplified assumptions made the current models either unable to obtain the solution or require additional computer-aided computation for actual cases. For numerical modeling of the process, most of the current work lack of validation from experimental data and thus leave their results questionable. Regarding experimental analysis, results from multiple groups are contradicted and focus majorly on ABS. Therefore, it is imperative to develop a hybrid model to analysis, model, and predict the thermal and mechanical behavior of the FDM process and products.

From the FDM optimization perspective, the existing research works overwhelmingly rely on performing pre-designed experiment with certain DoE strategies. With DoE methods, the material and machine operation cost would be extremely high, and a significant amount of time is spent on characterizing the properties of the products. Consequently, it is desired the combination of low-fidelity prediction model and high-fidelity experimental model could reduce the overall cost to find the optimum manufacturing conditions.

3. METHODOLOGY

3.1. Introduction

The objectives of this study are to analyze, model, and predict the thermal and mechanical behavior of the FDM process in order to achieve better dimensional accuracy and mechanical strength. To accomplish these objectives, a methodology of three models is proposed. The three models involved in the study of both thermal and mechanical behavior are an experimental model, a numerical model, and a predictive model.

For thermal analysis [103], the objective of the experimental model is to understand how process parameters affect the thermal history of an extrusion bead. In addition, the experimental model will provide the adequate variables to characterize the thermal-driven extrusion process as well as the tool to validate the numerical model. The objective of the numerical model is to simulate the same process that the experimental model studied and developed an analysis of characteristics that are hard to measure through the traditional experimental model. The conventional imaging method is complicated to obtain temperature and distortion data of inner structure since the field

⁷ Part of this section is reprinted with permission from ‘*Experimental and numerical investigation of the thermal behaviour of polylactic acid during the fused deposition process*’ by Xunfei Zhou, Sheng-Jen Hsieh & Yintong Sun *Virtual and Physical Prototyping* Vol 12:3 pp. 221- 233 (2017) and *Modelling and estimation of tensile behaviour of polylactic acid parts manufactured by fused deposition modelling using finite element analysis and knowledge-based library*’ by Xunfei Zhou, Sheng-Jen Hsieh & ChenChing Ting *Virtual and Physical Prototyping* (2017).. Copyright 2018 by Taylor & Francis Group

of view would be obscured by finished part while numerical approach would be a good supplement. First, the numerical model will be fed with the boundary, and initial conditions of the experimental model; among these conditions are: manufactured part geometry, deposited material temperature, platform temperature, ambient temperature, printing speed, and convective heat transfer coefficient of the platform and surrounding air. The experimental results used for the numerical model are the cooling time of extruded bead for each experimental condition. The experimental conditions will be used to validate the numerical model, and the experimental results will be used to validate the numerical model. Second, the parametric analysis will investigate the effect of printing parameters on temperature profiles during the printing process. Third, the simulation model will be used to predict the temperature, distortion, and thermal stress distribution of the FDM process. The flowchart of the investigation of thermal behavior is demonstrated in Figure 9.

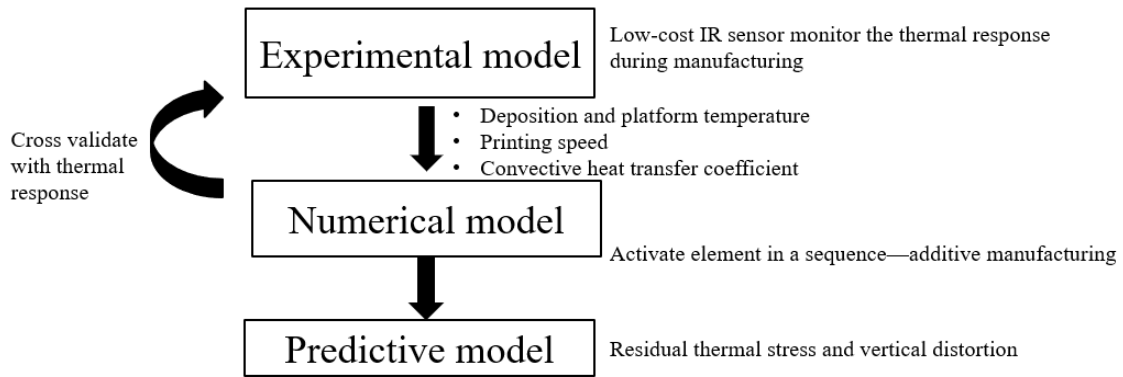


Figure 9 The flowchart for investigation of thermal behavior

For mechanical behavior [66], the objective of the experimental model is to understand how process parameters affect the mechanical strength of the product while the objective of the numerical model is to simulate the same process that the experimental model studied and analyze of how printing patterns would affect the final strength of the product. The information gathered from the experimental model would be the testing conditions and the geometry of each layer of the test specimen. After cross-validation, the developed numerical model could predict the strength and elastic performance of the manufactured part. The flowchart of the investigation of thermal behavior is demonstrated in Figure 10.

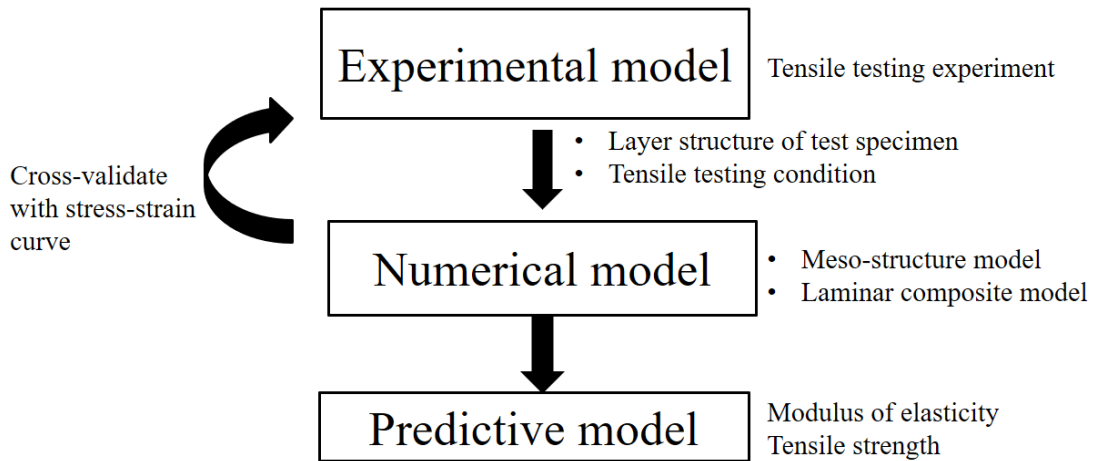


Figure 10 The flowchart for investigation of mechanical behavior

With the establishment of predictive models, a surrogate-based additive manufacturing optimizer (SAMO) is established to expediate the optimization process to maximize or minimize certain products' characteristics. The overall objective of SAMO is to reduce the number of experiments performed on additive manufacturing machines, and thereby making the optimization process more efficient. SAMO is developed to guide the decision-making process in optimization manufacturing conditions by combining cost-effective but less accurate predictive models with expensive but accurate experimental models. Iteratively, the SAMO obtain the current manufacturing condition and the corresponded response and determines the next manufacturing condition to attempt. An illustration of the SAMO optimization process is given in Figure 11.

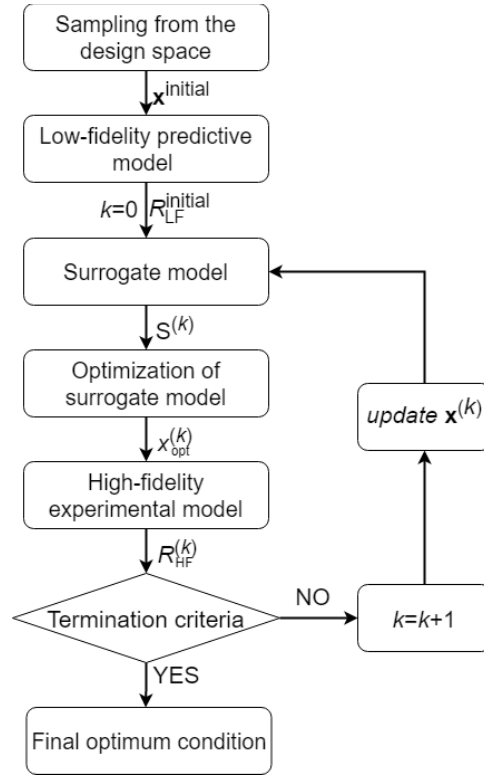


Figure 11 The flowchart of SAMO

3.2. Thermal behavior

3.2.1. Experimental model

3.2.1.1 Experimental material

The experimental system was composed of the printing material, a 3D printer, and one infrared array sensor. The printing material was 100% polylactic acid (PLA) with an emissivity of 0.96 [104]. A desktop-level FDM-based 3D printer (Flashprint Dreamer) was used to manufacture all parts discussed in this paper, which has a platform size of 230×150×150 mm and provides a part dimension error less than 0.2 mm. The temperature measurement device was one Melexis MLX90621 thermal infrared array

sensor. It is a cylindrically shaped infrared sensor with a diameter of 9.5 mm and a height of 13 mm. A 16x4 temperature matrix could be produced by this sensor with a maximum of 512 Hz data acquisition speed and a 60° x 16° field of view. The sensor was calibrated at 32 Hz to achieve a noise equivalent temperature difference at 0.4K with an accuracy of $\pm 1^{\circ}\text{C}$ or 3% of the temperature difference between object and ambient, whichever is larger. In addition, a PTAT (proportional to absolute temperature) sensor is integrated to measure the ambient temperature near the chip.

3.2.1.2 Experimental setup

The samples manufactured in this study were all cuboids with the same dimensions of 100 (length) by 10 (width) by 5mm (height). The geometry of the samples was first constructed in Solidworks and saved as a high-resolution stereolithography (STL) file. Then, the model was sliced and converted to G-code with printing parameters varied using the Flashforge software provided by the manufacturer of the machine. The slice setting is as follows: the top three and bottom three layers were printed with a rectilinear infill pattern with an infill density of 100% to support the structure; the remaining layers were printing with an infill density of 0% and had a single-bead wall structure. This slice setting helps to eliminate the effect of inter-layer bonding on the thermal behavior when the middle layers were manufactured.

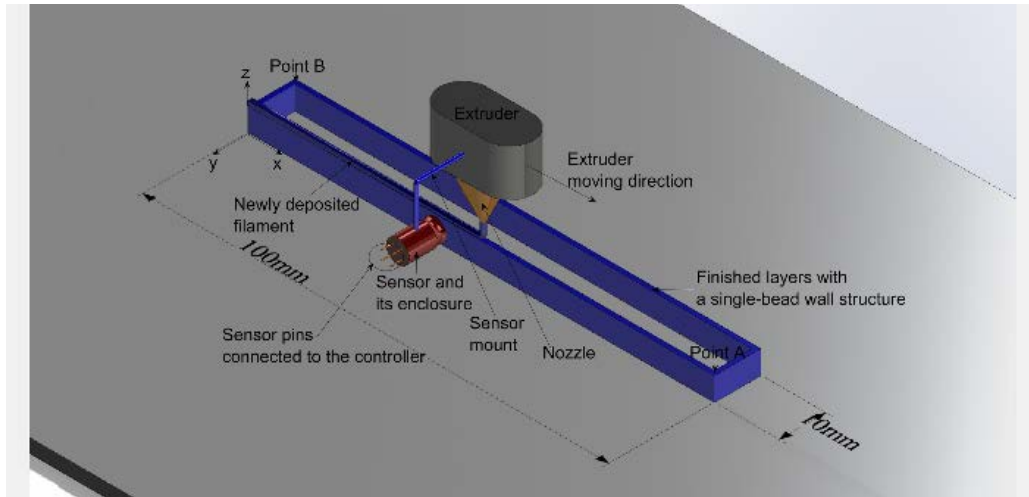


Figure 12 A schematic of the experimental setup for thermal behavior analysis

Figure 12 is a schematic of the system setup during the experiment. The infrared sensor was first installed inside a custom designed, 3D-printed enclosure. The enclosure was then mounted on the extruder, with the sensor positioned 10 mm away from the nozzle tip. As a result, the sensor moves with the nozzle at the same speed, with its field of view following the newly deposited material, providing more local signatures of the freshly deposited layers than the stationary camera. The field of view of the camera was set normal to the x-z plane of the manufactured part and focused on the front side of the newly deposited layer, offering a pixel size of 0.72 mm. An illustration of the field of view of the sensor is provided in Figure 13, where the acquired temperature matrix was converted to a grayscale image. In Figure 13, the white areas indicate high temperatures, while the dark regions suggest low temperatures. For the manufactured samples, only the

freshly deposited layer was monitored; the most recently deposited material (deposition position) was located near the center of the bottom row of the temperature matrix. During the printing process, the monitoring system was controlled by an Arduino board connected to a workstation. The Arduino program coded on the board continually monitored the state of the sensor and received data from it. This system is cost-effective; the whole temperature monitoring system costs less than \$100, which is much lower than the commercialized infrared camera.

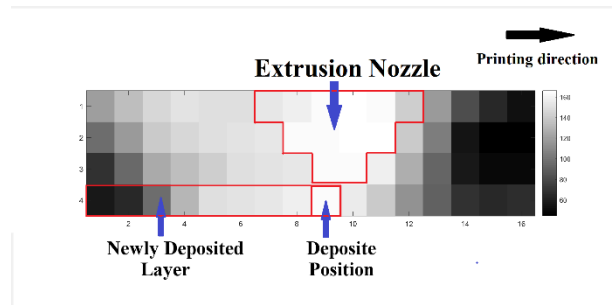


Figure 13 A grey scale image of the temperature matrix taken by the infrared camera

3.2.1.3 Design of experiment

To investigate the effect of printing parameters on temperature profiles during the printing process and to provide results for cross-validation for further numerical simulation, a parametric study approach was applied in the experimental model of this paper. Referring to the theoretical equations for temperature distributions during the

FDM process reviewed by Bellehumeur et al. [31], the process parameters included are the nozzle temperature, platform temperature, printing speed, and filament geometry. With filament width set as a constant variable, the nozzle temperature, platform temperature, printing speed, and layer thickness were chosen as the process parameters to investigate. Test parts were then designed based on those four parameters, where the Taguchi design of the experimental strategy was adopted. The analysis of variance (ANOVA) technique was then used to analyze the results. Three levels were applied to each parameter, representing high, medium, and low levels. A previous study [61] revealed that interactions between selected parameters were insignificant in uneven temperature field-induced distortion; therefore, in this study, an L9 orthogonal array was used for the most simplified design case, as represented in Table 3. Three replicates were performed for each experimental condition to reduce the effect of random noise. For the rest of the process parameters, the layer height and raster width of the solid infill layers were set to 0.3 and 0.4 mm, respectively, and the single-bead wall width (contour width) of the hollow layers was set as 1 mm.

Table 4 Design of experiment for analysis of thermal behavior

No.	Nozzle temperature (°C)	Platform temperature (°C)	Printing speed (mm/s)	Layer thickness (mm)
1	200	50	40	0.15
2	200	60	60	0.2
3	200	70	80	0.25
4	210	50	60	0.25
5	210	60	80	0.15
6	210	70	40	0.2
7	220	50	80	0.2
8	220	60	40	0.25
9	220	70	60	0.15

3.2.1.4 Experimental response

The transient thermal behavior of a sample during an additive manufacturing process can be characterized by the spatial thermal gradient at the onset of solidification, the cooling rate of the deposited material, or the cooling time of material [50]. In this study, the effective diffusion time was selected as the characteristic of the temperature evolution.

Effective diffusion time [105], t_{diff} , is defined as the time interval in between when the plastic material is extruded and reaches the glass transition temperature, T_g . This

characteristic is convenient to measure and calculate, and more importantly, it is directly related to the bonding strength of the products, as demonstrated by Rodríguez et al. [27], which prolongs fiber solidification times, leading to increases in the bonding strength.

3.2.2. Numerical model

A three-dimensional uncoupled thermal-structural finite element model was employed in

this study to simulate the FDM process. The commercial finite element model software ANSYS 17.2 was used for the simulation. Thermal analysis was first conducted to predict the temperature profile of a numerical model with the same geometrical dimensions of the sample. The temperature profiles were then used as the input of structural analysis, serving as the thermal load. The validation of the numerical results was performed by comparing the effective diffusion time with the experimental model. Since thermal stress is directly induced by an uneven temperature distribution, good agreement between the experiment and predictions of the temperature profile would support the applicability of the finite element model.

3.2.2.1 Governing equation of the thermal analysis

During the FDM process, plastic liquid beads, which quickly harden when they come into contact with the layers beneath them, are melted and extruded from the nozzle at a high temperature. The heat of the beads dissipates into the surroundings by conduction, convection, and radiation from the free surfaces. In addition, phase transitions of the polymer material also eject heat to the control volume. Under the transient state, the governing equation for energy balance inside of the printer can be described as

$$\rho c_p \frac{\partial T}{\partial t} = \nabla(k \nabla T) + \dot{q} \quad (3.1)$$

Hence $\rho c_p \frac{\partial T}{\partial t}$ represents the change in thermal energy storage, $\nabla(k \nabla T)$ represents

the transfer of thermal energy by conduction, and \dot{q} is thermal energy generation, which is composed of

$$\dot{q} = q_{\text{convection}} + q_{\text{radiation}} + q_{\text{phasechange}} \quad (3.2)$$

The following assumptions were made in the numerical simulation:

- [1] For a limited time interval, extruded material can be modeled as an element with finite volume and energy imposed on the simulation model.
- [2] Deposition speed of material is equal to extrusion speed of the nozzle, where travel speed of the nozzle is neglected.
- [3] The initial temperature of the material is equal to the deposition temperature.
- [4] Heat transfer from the bottom layer to the printing platform can be regarded as heat convection.
- [5] Radiation loss can be neglected.

Assumption 1 is essential to this work because of the nature of extrusion melting technology. The melted polymer material is deposited continuously to form layers; for a discretized time step, a small volume of material would become 'existent' to the simulation model. To simulate this sequential assembly process, the element birth and death feature of ANSYS is employed. 'Element death' refers the case when the stiffness or conductivity of an element is reduced to a very low level, 1e-6, by default. Therefore, the properties of those 'dead' elements would barely influence the surrounding elements.

In the same manner, if an element is 'born' or reactivated, stiffness and other properties would be restored to the standard value. Assumption 2 was made by analysis of G-code. Travel of the nozzle (movement without extruding material) only occurred when printing the solid infilled bottom and top layers, while the deposition of hollow layers is a continuous extrusion cycle. Assumption 3 was made based on previous experimental results, which showed that the deposition temperature is at least 40°C lower than the nozzle temperature. Assumption 4 was made based on the theory of interface thermal conductance [106]. Interfaces between two highly dissimilar materials are the result of contact at a select number of discrete points, where heat transfers occur through conduction at contact points and convection and conduction of the fluid in the interstitial gaps. Since the mass of the platform is relatively large compared to that of the product, the temperature of the platform can be considered uniform and constant across the printing process; heat transfer on the filament-platform interface would be regarded as convection. Assumption 5 was made based on the findings of Costa et al. [38], who discovered that the effect of radiation loss is negligible in most FDM cases when the convective heat transfer coefficient is more substantial than $60\text{W}\cdot\text{m}^{-2}\cdot\text{K}$.

3.2.2.2 Numerical model description

The geometry of the simulation model was constructed to include only the hollow layers, with a dimension of 100 (length) by 10 (width) by 4.2 mm (height), as demonstrated in Figure 14. The 3D thermal element SOLID70 and the structural element SOLID45 were

used to mesh the domain with the element dimension of 1 by 1 mm by layer thickness in the thermal and structural analyses, respectively. The total element numbers varied from 5964 to 3408, depending on the layer thickness settings.

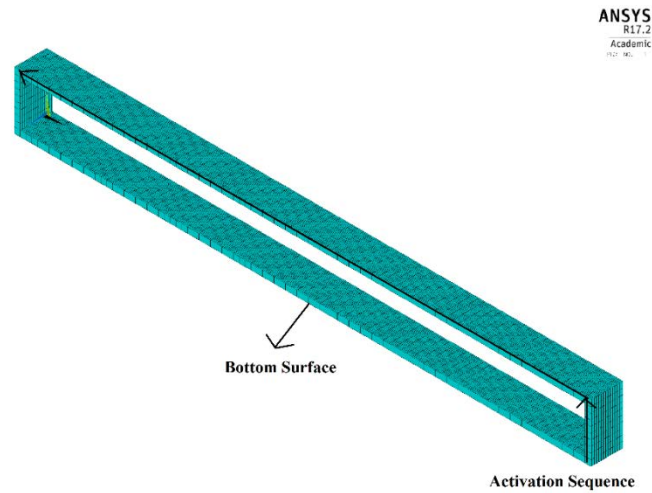


Figure 14 An example of the numerical model and its meshing scheme

3.2.2.3 Initial and boundary conditions

Numerical simulation in this study involves two steps—thermal and structural analysis. The following initial and boundary conditions were applied for thermal and structural analyses:

- [1] The initial temperature of an element is given based on correlations with the experimental results.

[2] In the structural analysis, the bottom surface was fully restrained in the x, y, and z directions.

[3] The boundary conditions of the thermal model will be discussed in section 3.2.3.

3.2.2.4 Finite element model material properties

The material used in the simulation was polylactic acid, which is the same as the experiment. The density was set to temperature-independent values while pressure, heat capacity, and thermal conductivity were set to be temperature-dependent to include abrupt changes around the melting and glass transition temperatures. The thermophysical properties used in the simulation model are listed in Table 5.

Table 5 Material properties used in numerical modeling of thermal behavior

$T(K)$	298.15			310	320	330	340	350	360
$\rho(\text{kg} \cdot \text{m}^{-3})$ [107]	1145.2								
$k(\text{W} \cdot \text{m}^{-1} \cdot \text{K}^{-1})$ [108]	0.111				0.178		0.195		
Young's modulus(Mpa) [107]	1280								
$\beta(\text{K}^{-1})$ [109]	7.4×10^{-4}								
$c_p(\text{J} \cdot \text{K}^{-1} \cdot \text{mol}^{-1})$ [110]	94.69	95.3	98.13	101.6	112.16	146.0	146.8		
$T(K)$	370	380	390	400	420	430	450	470	490
$c_p(\text{J} \cdot \text{K}^{-1} \cdot \text{mol}^{-1})$	148.2	149.05	149.81	150.57	152.09	152.85	154.37	155.89	157.41

3.2.3. Estimation of convective heat transfer coefficient and interfacial conduct resistance using artificial neural networks

3.2.3.1 Problem formulation

The accuracy of a numerical simulation model of the FDM process could greatly suffer from unrealistic treatment of boundary conditions [111]. It has been noticed that the thermal behavior of deposited filament is exceedingly dependent on convective cooling by air flowing through the manufacturing chamber. Bellehumeur et al. [31] discovered that from their theoretical model when convective heat transfer coefficient increased from 50 to 100W/m²·K, a 25% variation on bond formation was induced. Costa et al. [38] studied the effect of convection cooling on thermal diffusion time, they found out as convective heat transfer coefficient increased from 5 to 60W/m²·K, the cooling time needed to reach glass transition temperature decreased from 66 to 3 seconds (22 times), and a further increase to 150W/m²·K brings about a reduction of merely 2 times. Meanwhile, the part under manufacturing was also subject to heat conduction from the building platform. It is expected that convective heat transfer coefficient varies with the airflow rate inside of the chamber, building location, and the geometry of the

⁸ This section is reprinted with permission from Zhou, X., & Hsieh, S. J. (2018, May). Evaluating convective heat transfer coefficients in fused deposition process using infrared imaging and neural networks. In *Thermosense: Thermal Infrared Applications XL* (Vol. 10661, p. 106610K). International Society for Optics and Photonics. Copyright 2018 by SPIE

manufactured part [24]. While heat exchange with the support is controlled by both the thermal contact conductance and contact area [38].

Experimental measurement of convective heat transfer behavior in an FDM process is challenging in nature, as air flow rate in the building chamber are not easy to control in a typical commercial 3D printer [20]. Moreover, this problem is known as an Inverse Heat Conduction Problem (IHCP), which is difficult to solve in nature. Typically, how to determine the temperature history inside solid bodies for known initial and boundary conditions as well as thermophysical properties is a very standard Direct Heat Conduction Problem (DHCP), while IHCP rely on temperature and/or heat flux measurements to estimate unknown boundary conditions appearing in the mathematical formulation of physical problems. Traditionally, inverse problems can be solved either as a parameter estimation approach or as a function estimation approach [112]. If the functional form of the unknown quantity was known, such as the governing equation is known, then the inverse problem can be reduced to the estimation of a few unknown parameters. The general parameter approach is to iterative the boundary condition on the established analytical/numerical model until the result is close enough to the transient temperate measurement data [113]. The procedure involved is needs a long computation time due to large numbers of iterations. And the inverse problem needs to be determined as a function estimation approach in an infinite dimensional space of functions if no prior information is available on the functional form [114]. With these difficulties, the previous study on numerical simulation of the FDM process rarely direct measure the

boundary conditions but tends to estimate those values based on semi-empirical equations of forced convection [103], but the accuracy of them remained unknown.

Therefore, the objective of this study is to estimate the convective heat transfer coefficient from ambient air and interfacial conduct resistance from the building platform through a direct approach. The approach would use neural network to estimate those properties instead of the traditional iterative solutions [111].

The numerical model used in this study has the identical geometry of that used in Figure 12 and is constructed in ANSYS 17.2. The entire model is meshed with the SOLID70 element, and the thermophysical properties of the material are taken from Table 5 as well. The mesh size was selected as 0.2mm in most regions except for the part of interest. Close to the location where two specific points were selected, the mesh was refined to better cross-check with the experimental data, as indicated in Figure 15. The specimen is considered fully manufactured and put on the heated platform. Therefore, all elements would stay activated. With the control volume approach, the governing equation of this scenario is

$$\rho c_p \frac{\partial T}{\partial t} V = h_{\infty} A_{conv} (T - T_{\infty}) + h_p A_p (T - T_p) \quad (3.3)$$

And the initial condition is $T(t=0) = T_i$, as shown in Figure 16 . With the sophisticated geometry that 3D printed product could be, the analytical solution to this problem is not

apparent. To estimate h and h_c based on existing experimental measurement, ANN could be useful.

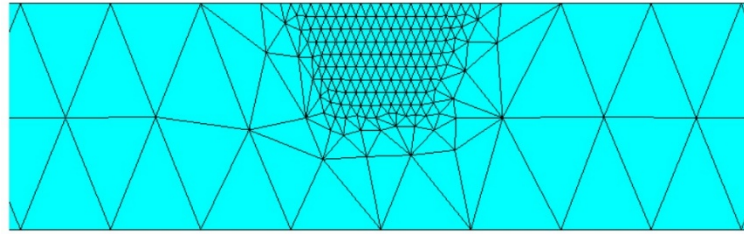


Figure 15 Locally refined mesh in the region of interest

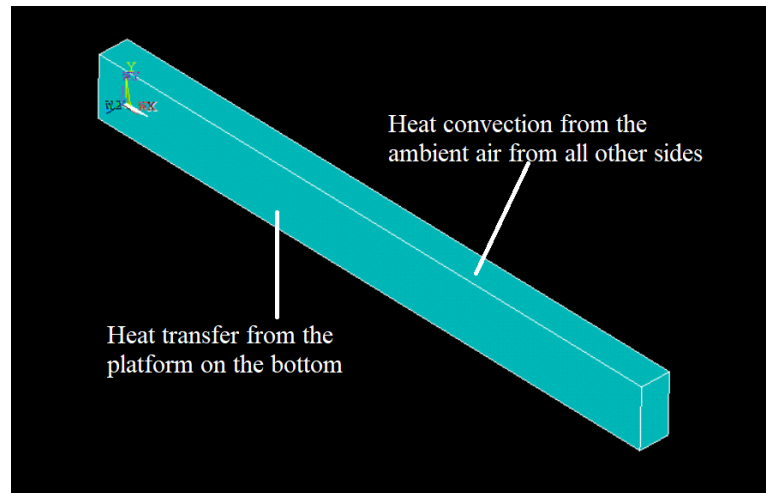


Figure 16 The numerical model used in the determination of boundary condition

3.2.3.2 Training of the ANN models

In this study, Matlab is employed to construct the networks, and only feed-forward networks were used. The Levenberg–Marquardt backpropagation algorithm [115] was used to minimize the mean square error between the actual and desired output by adjusting the weights and biases associated with links inside the network. During the backward pass, the error terms are computed, and the weights/biases are updated. ANN is prone to over-fit the data; therefore, the dataset was divided into three subsets—training, validation, and testing. When the network begins to over-fit the data, the error on the validation set typically begins to rise, which stops the training when the error increases for a specified number of iterations [116]. The structure of the networks is shown in Figure 17.

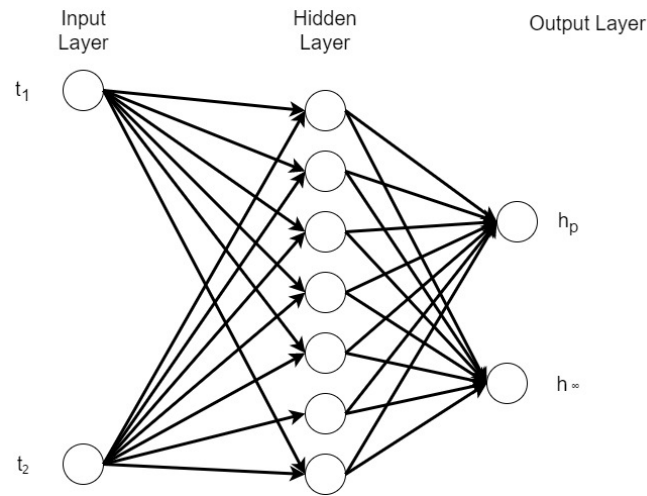


Figure 17 The topology of the ANN model used to determine boundary condition

As depicted in Figure 17, the network has a 2–7–2 topology where the input nodes are two characteristics of the temperature over time curves at two specific surface points. It should be noted it is possible that the entire temperature evolution curve can be used as the input data. However, considering the potential discrepancy between the experimental and numerical results that brought by measurement error and inaccurate initial condition, it is recommended that some typical features should be extracted from the temperature history curves. In this study, the time for the temperature to reach 5 degrees higher than the initial temperature was used (t_{+5}). Other possible approaches include approximation of the measurement data and use temperature difference of two curves at a specific time [117]. Only one hidden layer was used to construct the networks in this paper, and seven hidden nodes generated the best performance during the initial testing and screening process. And finally, the output of the network is convective heat transfer coefficient h_{∞} and interfacial conduct resistance h_p .

100 cases from the simulation data were used to train, validate, and test the network. In those cases, the h_p value varied from 500 to 5000, with an increment of 500 while the h_{∞} value ranged from 10 to 100, with an increase of 10. Those cases were divided into training, validation, and testing subsets with the ratio of 64:16:20, based on a rule of thumb. As the subsets were divided randomly, the network was trained and evaluated 100 times, and the average obtained performance value was chosen to improve network

generalization. An example of the training performance is demonstrated in Figure 18, which showed the result is satisfactory.

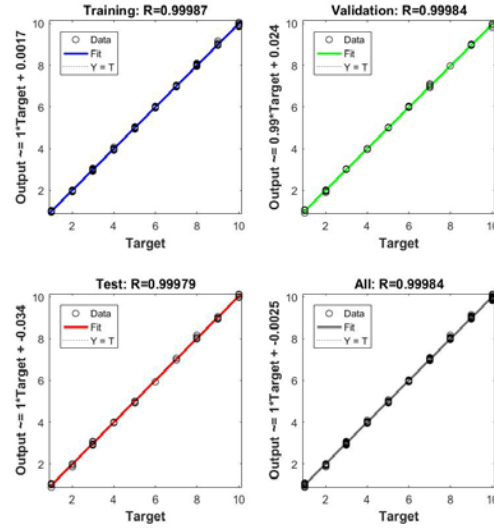


Figure 18 Performance of the trained model

3.2.3.3 Experimental setup

In this work, the manufactured part was heated from the platform while cooled by the ambient air. The response of the thermally excited surface was simultaneously monitored and recorded using an infrared camera. The sample has the same geometry as that used in Figure 12. The experiment was conducted using a Compix[®] model 222 infrared camera (1 frame/second), which could produce images with a resolution of 160

by 120 pixels and was calibrated for a noise equivalent temperature difference at 0.1 K and accuracy of ± 2 °C or 2%, whichever is larger. The test sample was positioned with the front side perpendicular to the view of the camera, at a distance of approximately 130 mm, and then exposed to the thermal excitation, generating a pixel size of 0.5 by 0.5 mm². A picture of the experimental setup is given in Figure 19.

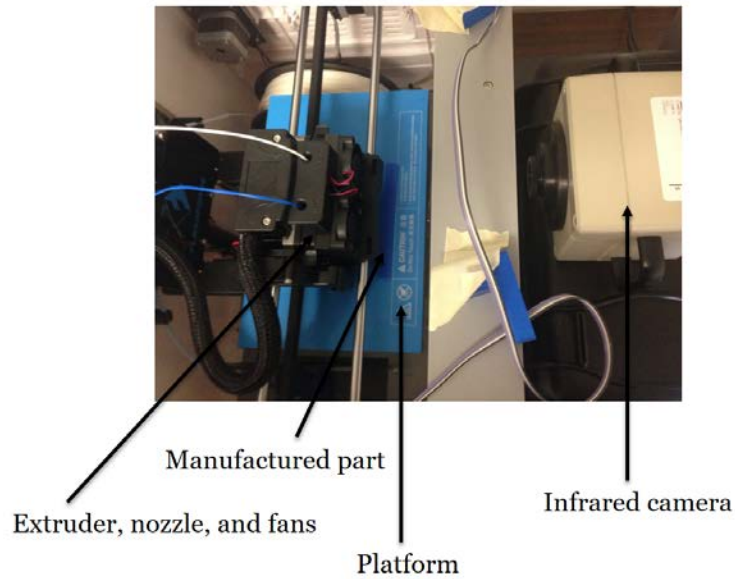


Figure 19 An image of the experimental setup to determine boundary condition

To mimic the manufacturing condition, the experimental procedure can be described as follows: maintain the platform and nozzle temperature at 60°C and 210°C respectively through the machine controller and keep the ambient air temperature at 25 °C through air

conditioning; turn on the turbo and cooling fans and move the extruder above the desired sample position; quickly place the sample from outside to the desired location. In that way, the sample would be heated from ambient temperature to platform temperature in the experimental conditions. The two specific points of interest were determined to be in one pixel and two pixels above the platform, located in the middle of the front face, as shown in Figure 20.

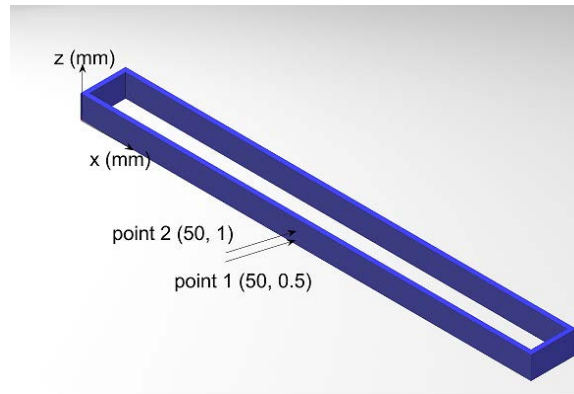


Figure 20 An illustration of the points of interest in the boundary condition determination study

3.3. Mechanical behavior

3.3.1. Experimental model

3.3.1.1 Specimen preparation

The test specimen was created in Solidworks in STL format, and the geometry of it was set according to ASTM D638 [118] Type IV specimen geometry, which is shown in Figure 21.

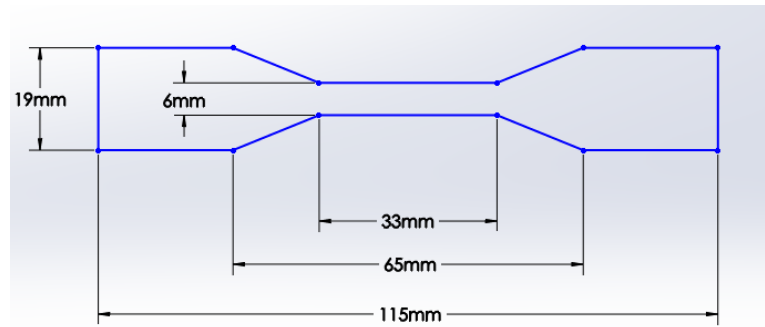


Figure 21 The dogbone structure and its dimensions

Then, the STL file was sliced and converted to G-code with varied process parameters. In this work, two kinds of slice settings were used: the unidirectional model where all layers have the same slice setting, and the bidirectional model, where the top and bottom half layers have different slice settings, with an example given in Figure 22. Using a bidirectional model can accommodate a more efficient filling strategy—an adaptive fill

pattern with variable density. As explained by Stratasys Ltd. [119], on the contrary to traditional filling techniques where the entire part was filled with the same pattern, adaptive fill pattern allows a single part to have combinations of solid and sparse fill styles, and each region's density can be adjusted independently. This filling strategy [119, 120] has the advantage of optimized strength, weight and performance, reduced building time and cost and enabled niche applications (e.g., end-use parts, fiber molding and thermoforming). Yet most current work focuses on uniform printing patterns across all layers. This experimental setting strategy could improve understanding of how the overall strength of the part is affected by each individual layer. To reduce the complexity of the experiment, only the printing pattern and infill density were chosen as parameters to investigate, while other process parameters remained constant over all experimental conditions. Three levels were selected for each variable, while Table 6 shows the design of the experiment.

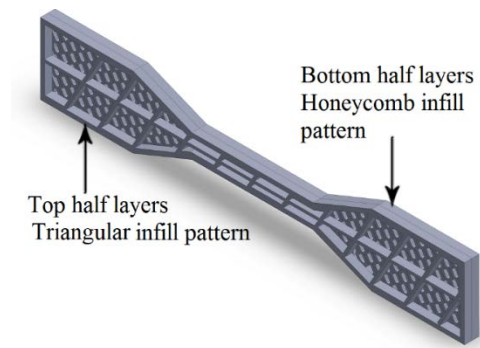


Figure 22 An example of bidirectional sample

Table 6 Design of experiment for mechanical behavior investigation

Unidirectional Specimens				
No.	Infill Density (%)		Printing pattern	
1	20		Rectilinear	
2	20		Honeycomb	
3	20		Triangular	
4	50		Rectilinear	
5	50		Honeycomb	
6	50		Triangular	
7	80		Rectilinear	
8	80		Honeycomb	
9	80		Triangular	
Bidirectional Specimens				
No.	Top Infill Density (%)	Top Printing pattern	Bottom Infill Density (%)	Bottom Printing pattern
1	20	Rectilinear	20	Rectilinear
2	20	Honeycomb	50	Honeycomb
3	20	Triangular	80	Triangular
4	50	Rectilinear	50	Triangular
5	50	Honeycomb	80	Rectilinear
6	50	Triangular	20	Honeycomb
7	80	Rectilinear	80	Honeycomb
8	80	Honeycomb	20	Triangular
9	80	Triangular	50	Rectilinear
10	20	Rectilinear	20	Rectilinear
11	50	Honeycomb	20	Honeycomb
12	80	Triangular	20	Triangular
13	50	Triangular	50	Rectilinear
14	80	Rectilinear	50	Honeycomb
15	20	Honeycomb	50	Triangular
16	80	Honeycomb	80	Rectilinear
17	20	Triangular	80	Honeycomb
18	50	Rectilinear	80	Triangular

The specimens were manufactured in the same FlashForge Dreamer machine [121] used in a previous thermal behavior study, and three replicates were performed for each experimental condition to reduce the effects of random noise. During the manufacturing process, the extrusion and platform temperatures were kept at 210°C and 60°C, respectively. The layer thickness or slice height was set at 0.2 mm, with a total of 20 layers. The horizontal build orientation was adopted for all parts manufactured in this study – all specimens are fabricated with the build direction parallel to the tensile load to be applied later.

3.3.1.2 Tensile testing procedures

For tensile behavior characterization, an Instron 5567 Universal Testing System was utilized. Figure 23 shows the experimental setup of the sample after it was stretched and broken.

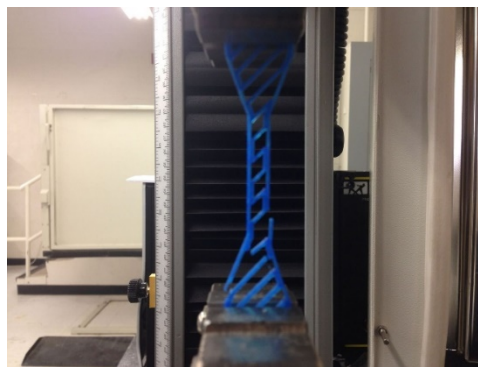


Figure 23 An image of the tensile testing process

The testing was performed in a displacement-controlled manner—the extensometer was used as the control device. The upper grip was travelled at 2.5 mm/min, which causes rupture within 0.5 to 4 min of testing time. The displacement, ΔL , and force load, F , values were recorded every 0.1 s throughout the experiment, and the engineering stress σ and strain ε values were calculated based on the following equations

$$\sigma = \frac{F}{A} = \frac{F}{6 \times 10^{-3} \cdot 4 \times 10^{-3}} \quad (3.4)$$

$$\varepsilon = \frac{\Delta L}{L} = \frac{\Delta L}{33 \times 10^{-3}} \quad (3.5)$$

Where σ and F have the units of Pa and N, respectively. In that way, the corresponding effective elastic modulus was obtained as the slope of the linear portion of the stress over strain curve.

3.3.2. Numerical model

3.3.2.1 The Meso-structure model

The commonly adopted orthotropic constitutive model considers the additive manufactured product as a bulk material, which prevents the reflection of in-product geometry and requires extensive experimental input for the settings of each printing process parameter. Therefore, a direct approach was considered in this study, which aims to depict the fiber structure of each layer. Very limited work [122, 123] has been performed on modelling the bead structure of the actual part, and the accuracy of the

results has not been satisfactory [123]. Considering that drawing the fibers manually for a part with complex geometry requires extensive time, this work developed an automated script to convert G-code to a finite element model ready for analysis in ANSYS.

Since G-code depicts the movement of the nozzle during the printing process, Matlab was first used to convert G-code into a drawing script for a certain layer. Then AutoCAD was utilized to draw the structure of the infill pattern, in this specific layer, in a 2D model. Finally, the 2D filament geometry model was extruded to a 3D format with Solidworks, and then saved as a Parasolid file, which could be used as the geometric input for ANSYS. An example of this conversion process is demonstrated in Figure 24.

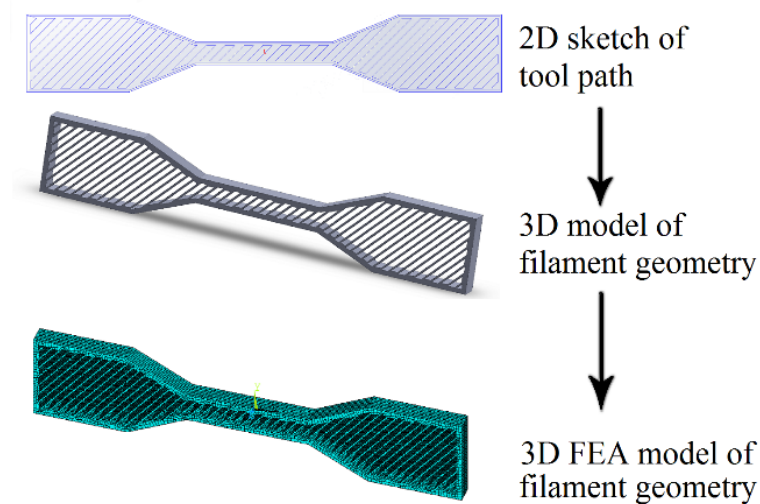


Figure 24 The conversion process from G-code to 3D FEA model

Regarding the meshing scheme, two different element types were considered for each set of individual numerical simulation conditions, based on that which resulted in better mesh quality. The first is free meshing with the SOLID187 element, which is a higher order 3D, 10-node element. It has quadratic displacement behavior and is well suited to modelling irregular meshes. The second meshing scheme is sweep meshing, with the SOLID186 element that is a higher order 3D 20-node solid element that also exhibits quadratic displacement behavior. In this study, it is discovered sweep meshing is preferable with high infill density. The element size and time step for the solving step were selected based on grid and time step independence tests, as discussed later in section 5.2.1.

The tensile testing process was simulated in a displacement-controlled manner, identical to the experimental conditions. The end of one grip was fixed at all conditions, while another end travelled at 2.5 mm/min. The uniaxial test data for the PLA filament was obtained from the literature [124], and the Poisson's ratio of the filament was set as 0.36 [108]. With the boundary conditions defined and material properties set, a transient structural analysis was performed for a total of 10 s. The sum of the nodal force in the x-direction of the moving end was calculated and used as the numerical simulated load force, while the displacement was the travel speed multiplied by time. Hence, the engineering stress, strain, and effective modulus of elasticity could be calculated similarly as for the experimental conditions.

3.3.2.2 The Laminate composite approach

Since there is a research gap with regards to cross-validation between the experimental and numerical data of the laminate composite (LC) modelling approach, this approach was employed to examine the accuracy and then compare with the MS model. The FEA model of this approach was constructed using only the neck region of the specimen (33×6×4 mm) in the experimental model.

SHELL281, a 3D 8-node structural shell element that supports plasticity, was selected in ANSYS 17.2 to mesh the sample geometry. The FE model was meshed with an element size of 0.5×0.5×0.2, which was determined by refining the meshing to achieve appropriate compatibility for the FE results, resulting in a total element number of 15840. The boundary condition was also defined as fully fixed on one end, while the other end travelled in one direction. In the solving step, a transient mechanical analysis was performed with the time interval of 0.1 s and a total of 300 steps to match the experimental data acquisition speed.

In the LC model, the material properties of each layer vary with different values of printing parameters, and the experimental data must be input; therefore, it is unsuitable for validation with unidirectional samples. For the cross-validation of bidirectional samples, the material properties of the top and bottom ten layers were calculated based on previous unidirectional samples.

3.4. Development of surrogate-based additive manufacturing optimizer

In this section, the optimization methodology of the developed surrogate-based additive manufacturing optimizer (SAMO) is presented.

3.4.1. Objective function

Given the nature of AM processes, most process parameters involved are discretized.

For example, set the extrusion temperature in the FDM process to 202.1347°C is meaningless, since the temperature control system cannot reach such an accuracy. It is much more common that the setting of each parameter is partitioned in a certain range. Therefore, optimization of AM process is a discrete optimization problem with each parameter is selected from a range of positive integers. Recall Equation 2.14, the optimization problem with AM background can be formulated as:

$$\left. \begin{array}{ll} \text{Maximize/Minimize} & f_p(\mathbf{x}), \quad p = 1, 2, \dots, P \\ \text{subject to} & h_j(\mathbf{x}) = 0, \quad j = 1, 2, \dots, J \\ & g_k(\mathbf{x}) \leq 0, \quad k = 1, 2, \dots, K \\ & \mathbf{x}_{\min} < \mathbf{x} < \mathbf{x}_{\max} \end{array} \right\} \quad (3.6)$$

where $\mathbf{x} = \{x_1, x_2, \dots, x_n\}$, $\mathbf{x}_{\min} = \{x_1^L, x_2^L, \dots, x_n^L\}$, and $\mathbf{x}_{\max} = \{x_1^U, x_2^U, \dots, x_n^U\}$ are all positive integer vectors. With the background of FDM, \mathbf{x} could be extrusion temperature, platform temperature, printing pattern, etc., while $f_p(\mathbf{x})$ can be characteristics of the products or process, such as tensile strength, dimensional error, or building time. Sometimes it is required to perform multi-objective optimization that each

$f_p(\mathbf{x})$, $p = 1, 2, \dots, P$ need to be either maximized or minimized. Under that condition, although it is possible to locate the Pareto front or a trade-off region that every solution in this region is not dominated by other solutions [125], the operator or end-user still need to select the solution based on his/her personal preference. Hence, in this study we will adopt the weighted sum approach to help the user making the decision. In this approach, the user would be asked for preference levels for multiple objectives (i.e. mechanical strength, building time, material cost) and maximum/minimum allowance limit for each objective. And the multi-objective optimization problem would be converted to a single-objective optimization problem with additional constraints.

$$\left. \begin{aligned} &\text{Maximize/Minimize } f(\mathbf{x}) = \sum_{p=1}^P w_p \cdot f_p(\mathbf{x}), \quad p = 1, 2, \dots, P \\ &\text{subject to } h_j(\mathbf{x}) = 0, \quad j = 1, 2, \dots, J \\ &\quad \quad \quad g_k(\mathbf{x}) \leq 0, \quad k = 1, 2, \dots, K \\ &\quad \quad \quad \mathbf{x}_{\min} \leq \mathbf{x} \leq \mathbf{x}_{\max} \\ &\quad \quad \quad F_{p,\min} \leq f_p(\mathbf{x}) \leq F_{p,\max}, \quad p = 1, 2, \dots, P \end{aligned} \right\} \quad (3.7)$$

3.4.2. Optimization algorithm

The algorithm developed in this study adopted the response correction approach and is specifically designed to reduce the high-fidelity experimental model evaluation times. It can be summarized as follows:

[1] Set $k = 0$, Identify enough data points $\mathbf{x}_i^{(k)}$, $i = 1, 2, \dots, n$ and evaluate their response

$\mathbf{R}_i^{(k)}$, $i = 1, 2, \dots, n$ in the LF predictive model

- [2] Construct an ANN surrogate model $S^{(k)}$ bases on dataset of $\{\mathbf{x}_i^{(k)}, \mathbf{R}_i^{(k)}\}$
- [3] Identify the current optimum point $\mathbf{x}_{\text{SAMO,opt}}^{(k)}$ with the weighted sum approach from the output values of the constructed ANN surrogate model
- [4] Evaluate the response of $\mathbf{x}_{\text{SAMO,opt}}^{(k)}$ from the HF experimental model to obtain $\mathbf{R}_{\text{HF}}^{(k)}$
- [5] Check the convergence criteria; if met, then $\mathbf{x}_{\text{SAMO,opt}}^{(k)}$ is the optimum point; otherwise, increase k by 1, update ANN training dataset $\{\mathbf{x}_i^{(k)}, \mathbf{R}_i^{(k)}\}$, and return to step 2

The key characteristic of the above algorithm is how to update the ANN training dataset

$\{\mathbf{x}_i^{(k)}, \mathbf{R}_i^{(k)}\}$. One intuitive way is to directly add $\{\mathbf{x}_{\text{SAMO,opt}}^{(k)}, \mathbf{R}_{\text{HF}}^{(k)}\}$ to the previous dataset.

While a slightly more complicate approach is to first choose $\mathbf{x}_i^{(k+1)}$ in a trust region of

$\mathbf{x}_{\text{SAMO,opt}}^{(k)}$ so that the criteria of $\|\mathbf{x}_i^{(k+1)} - \mathbf{x}_{\text{SAMO,opt}}^{(k)}\| \leq \varepsilon$ could be met, then insert the

previous optimum point $\mathbf{x}_{\text{SAMO,opt}}^{(k)}$ to $\mathbf{x}_i^{(k+1)}$. The sampling strategy is take 5-10% of the

levels possible on each parameter dimension with evenly space between each other. For

example, if x_1 can vary between level 1 and 100 in its own dimension, then level 20, 40,

..., 100 would be picked to construct the LF surrogate model. The optimizer is

terminated if $\|\mathbf{x}_{\text{SAMO,opt}}^{(k+1)} - \mathbf{x}_{\text{SAMO,opt}}^{(k)}\| \leq 4$ or $k > 50$

3.4.3. Optimization performance evaluation

First of all, it should be noted the accuracy of the algorithm need to be evaluated by the difference of estimated optimum response and real optimum response with the following criteria

$$\text{Error}_{\text{est}} = \frac{\|R_{\text{opt,est}} - R_{\text{opt,real}}\|}{\|R_{\text{opt,real}}\|} \times 100\% \quad (3.8)$$

$\text{Error}_{\text{est}} = 0\%$ means the algorithm successfully located the analytically optimum solution, while a high value means the accuracy performance of the developed algorithm is extremely low.

One characteristic of the objective functions that could impact the accuracy of the optimization algorithms is the local optima. On those local maximum or minimum points, the partial derivatives are 0 and gradient-based algorithms are extremely easy to “trap” in them. With regard to the developed algorithm itself, both DoE or sampling strategy and randomness in step 1 could potentially affect the accuracy of the results. The DoE strategy is designed to allocate enough training points in the studied design space and apparently how to fill the design space would influence the final results. Moreover, as constructing neural networks requires weights between neurons to initialized first, random initial weights would have their effect on accuracy of the algorithm.

Alternatively, recall the overarching goal of develop SBO-MFM is to reduce the cost and time for performing optimization, the criteria would then be the overall cost to conduct the experiment and perform numerical simulation. One way to estimate the overall cost is

$$\begin{aligned} \text{Cost}_{\text{overall}} &= C_{\text{overall}} = C_{\text{exp}} + C_{\text{sim}} \\ &= n_{\text{exp}} (C_{\text{machine}} + C_{\text{material}} + C_{\text{testing}}) + n_{\text{sim}} (C_{\text{computation}}) \end{aligned} \quad (3.9)$$

Based on case study of industry level FDM machine [126, 127], with 30 minutes of manufacturing, one mechanical testing procedure, and 5 minutes of simulation on an average desktop computer, it is estimated that

$$\begin{aligned} C_{\text{machine}} &= \text{Machine and labour cost} \times \text{Build up time} = 20\$/\text{hr} \times 0.5\text{hr} = 10\$ \\ C_{\text{material}} &= \text{Material cost} \times \text{Part weight} = 0.25\$/\text{g} \times 2\text{g} = 0.5\$ \\ C_{\text{testing}} &= 50\$ \\ C_{\text{computation}} &= \text{Computer and Labour cost} \times \text{Build up time} = 10\$/\text{hr} \times 5\text{min} = 0.83\$ \end{aligned} \quad (3.10)$$

And Equation 3.10 can be converted to

$$C_{\text{overall}} = C_{\text{exp}} + C_{\text{sim}} = n_{\text{exp}} \times 60.5\$ + n_{\text{sim}} \times 0.83\$ \quad (3.11)$$

3.4.4. Case studies

The developed SAMO would be evaluated on several cases and compare against existing literature/methods on aforementioned criteria, where the details of those cases were summarized in Table 7.

Table 7 The testing cases for developed SAMO

Case No.	Function source	Input parameter number	Output parameter number	Compare against	Note
1	A simple non-linear function	1	1	SAO and ARC	The most simplified condition
2	Gramacy & Lee function [128]	1	1	SAO and ARC	Semi-periodic function with multiple local optimum
3	Six-Hump Camel function [129]	1	2	SAO and ARC	Six local minima, two of which are global
4	Tensile strength of FDM parts [56]	1	4	Original literature method [56]	Original method is group method for data handling and DoE
5	Strength and volumetric shrinkage of FDM parts [92]	2	3	Original literature method [92]	Original method is DoE with 20 runs, then ANOVA, then GA on ANOVA fitted functions
6	Experiments on modulus of elasticity/building time	1	2	Conducted experiment	Self-conducted experiments based on developed predictive model

For case #1 to #5, low fidelity numerical simulation model would be created by perturbate the original analytical function by a certain degree, typically with a deviation of 10%. While for case #6, the developed numerical simulation model would be used as the low-fidelity model for predict the modulus of elasticity and building time would be estimated by a pre-determined function.

3.5. Summary

A hybrid model approach was proposed to investigate the effect of process parameters on thermal and mechanical behaviors, as well as optimize the manufacturing process. For investigation of thermal behavior, the objective of the hybrid model is to analyze

how extrusion temperature, platform temperature, printing speed and layer thickness would affect effective diffusion time. Taguchi design would be adopted in this study to reduce the experimental runs, and three replicates will be performed for each experimental condition. A low-cost IR sensor is used as the monitoring device and move along with the extruder/nozzle, provided information near the deposition region. The relationship between the effective diffusion time and process parameters would be analyzed by ANOVA and signal-noise ratio analysis, testing where those parameters would significantly affect the response and whether they are positively correlated or not. The numerical model would be constructed in an element activated in sequence way to mimic the additive manufacture process. The initial condition would be gathered from the experimental data, and the boundary condition is solved with an inverse heat transfer problem. After completing cross-validation, the numerical model could predict the residual thermal stress and vertical distortion.

For the investigation of mechanical behavior, the objective of the hybrid model is to analyze how infill pattern and infill density would affect tensile strength of the product. Two types of specimens would be tested which are unidirectional specimens and bidirectional specimens. Bidirectional samples are used to evaluate how a combination of two infill patterns inside of one product would affect the final strength of it. Two approaches are made to numerically model the mechanical behavior — meso-structure model and laminar composite model. The meso-structure model aims to reproduce the geometry of infill patterns while the laminar composite model is used to compare the

performance. Finally, the developed predictive model will determine the tensile strength and elastic performance of the final product with infill patterns as the inputs.

For optimization of the manufacturing process, the objective of the hybrid model is to reduce the number of experiments performed on additive manufacturing machines, and thereby making the optimization process more efficient. The hybrid model based optimizer is developed to guide the decision-making process in optimization manufacturing conditions by combining cost-effective but less accurate predictive models with expensive but accurate experimental models. Iteratively, the developed optimizer obtains the current manufacturing condition and the corresponded response and determines the next manufacturing condition to attempt. Therefore, the developed optimizer would be an efficient algorithm with reduced overall cost.

4. RESULTS AND ANALYSIS OF THERMAL BEHAVIOR OF POLYLACTIC ACID DURING THE FUSED DEPOSITION PROCESS

In this section [103], analysis for thermal behavior experimental and numerical model was performed. Characteristics of the material temperature distribution during the FDM process and the effect of process parameters on thermal diffusion time were evaluated in Section 4.1. Furthermore, Section 4.2 verified and validated the simulation model based on the experimental results. And in the end, the prediction results of part distortion and the accumulated residual stress were presented in this section as well.

4.1. Experimental model

4.1.1. Analysis of deposition temperature

As indicated in Figure 13, the newly deposited material was located at the same pixel position in the acquired temperature matrix due to co-axial movement between the sensor and the nozzle. With the deposition temperature defined as the temperature of the material when in contact with the layer or platform beneath it, the deposition temperature could be analyzed with a plot of the temperature of that fixed pixel over

⁹ This section is reprinted with permission from 'Experimental and numerical investigation of the thermal behaviour of polylactic acid during the fused deposition process' by Xunfei Zhou, Sheng-Jen Hsieh & Yintong Sun Virtual and Physical Prototyping Vol 12:3 pp. 221- 233 (2017). Copyright 2018 by Taylor & Francis Group

time. An example of such a plot under experimental condition No. 1 is given in Figure 25.

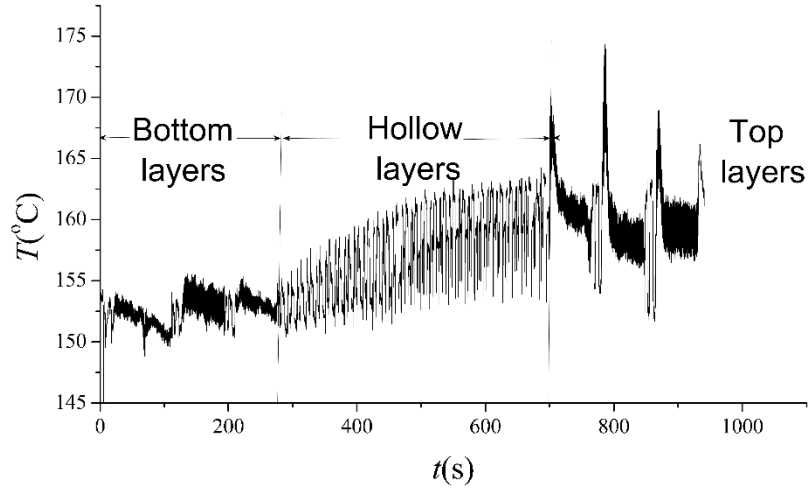


Figure 25 A plot of deposition temperature over time under experimental condition No. 1

Figure 25 demonstrated that under experimental condition No.1, the deposition temperature of PLA would not exceed 170°C in the hollow layers when the nozzle temperature was set as 200°C. This phenomenon was also observed in Dinwiddie et al.'s experiments [47], Seppala and Migler's experiments [48], and Bellini's simulations [130], where ABS or ceramics were used as the printing material. The discrepancy can be explained by the intensive cooling effect during the time interval between extrusion and deposition of the material. Second, it can also be observed that in Figure 25 the temporal deposition temperature profile could be separated into three regions based on

the spacing and shape of the data, where the first region lies in the time range of around 0–300 s, the second lies around 300–700 s, and the third region is from 700 s to the end of the experiment. By examining the G-code, it is discovered that the first region occurred during the printing of the bottom three layers with a 100% linear infill pattern and the third region occurred during the printing of the top three layers with the same pattern. The hollow layers are the part-of-interest of this study; therefore, the data was cropped to only contain the second region for analysis in the following sections. Third, the peaks of the periodic deposition temperature data align with the time when the front filament was fully extruded (point A in Figure 12), while the troughs of the temperature profile match the end time when printing the back filament (point B in Figure 12). The formation of the periodic temperature signal was caused by the gradual change in the heat transfer conditions upon finishing the layer and when the field of view of the sensor was blocked by the front filament when the nozzle moved to the back. Finally, there is an increasing trend in the deposition temperature temporal profile. Plots of the peak temperatures while printing each hollow layer over time in all nine experimental conditions are given in Figure 26.

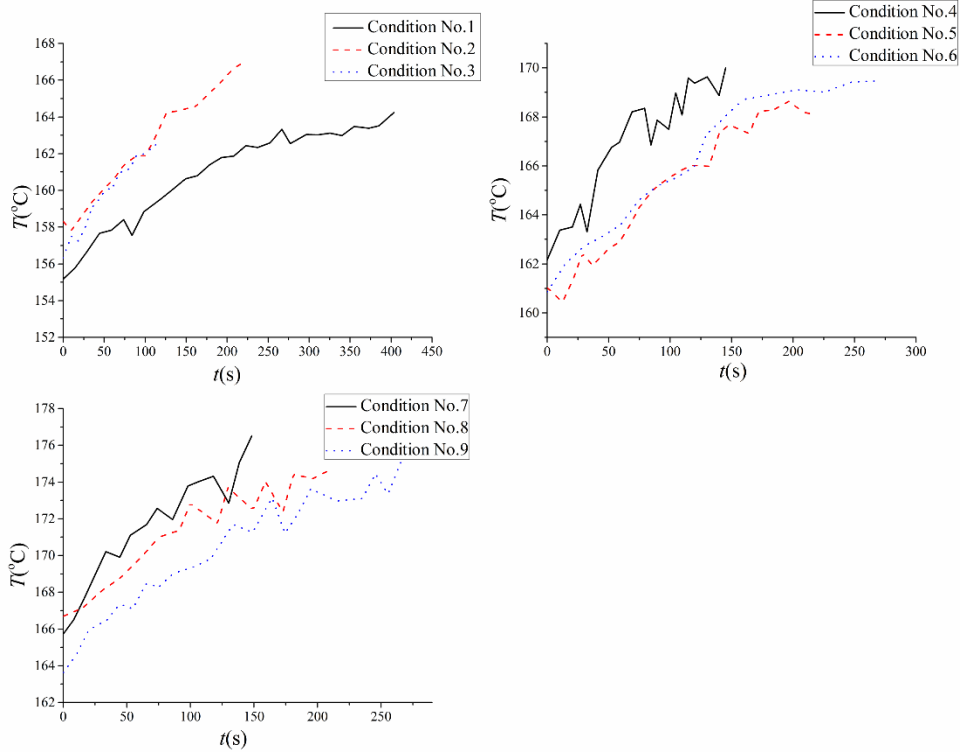


Figure 26 Plots of deposition temperature over time for all experimental conditions

Figure 26 demonstrates that there were at least 8 degrees of temperature increment in all nine cases, which strongly contradicts the assumption that deposition temperature remains constant made in previous simulation literature [34, 130]. It is presumed that this invalid assumption would result in a discrepancy between simulation and experimental data.

4.1.2. Analysis of ambient temperature

During the printing process, ambient air in the machine chamber was heated by the printing platform and nozzle. Ambient temperature was assumed to remain constant in

the previous literature [34, 130]; however, validation of this assumption through experimental data has not been provided. The ambient temperatures of condition Nos. 1 and 9, which represent two extreme cases of nozzle temperature and platform temperature, were plotted in Figure 27.

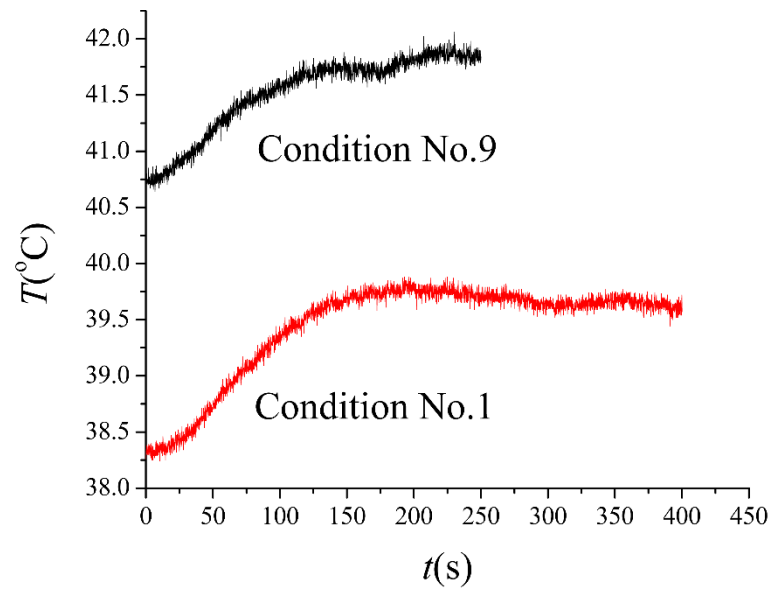


Figure 27 A plot of ambient temperature over time

Figure 27 showed that increasing the nozzle temperature and platform temperature by 20°C would lead to an approximately 3°C increase in the average ambient temperature. However, fluctuation of the ambient temperature was less than 2°C in both cases, while

further analysis of all 27 cases confirmed that overall temperature variation was less than $\pm 1^\circ\text{C}$.

4.1.3. Analysis of effective diffusion time

A reference point was chosen to compare the effective diffusion time of all experimental conditions. In this study, for the layer heights 0.15, 0.20, and 0.25 mm, the center points of the front filaments of the 10th, 8th, and 7th layers were selected as the reference points, corresponding to the height of $\frac{1}{4}$ that of all hollow layers.

Since the infrared sensor was moving along with the nozzle at the same velocity, the temperature data must be mapped to acquire the temporal temperature evolution of the reference point. Denoting the frame when the nozzle was located above the reference point as the reference frame with a frame number of 0, the time is 0, and the reference point occupied the pixel number (x_0, y_0) in the initial frame. During the printing of the front filament of the layer where the reference point was located, the nozzle only moves along the positive x-direction; hence, the reference point would appear in frame number N at the pixel position $(x_0 - \frac{s}{f \cdot \Delta x} N, y_0)$, where s is printing speed (mm/s), f is the frequency that thermography images were taken (Hz), and Δx is the pixel size (mm).

Therefore, temperature of the reference point at time t would be

$$T_r(t) = T(x_t, y_t, N_t) = T(x_0 - \frac{s}{f \cdot \Delta x} N, y_0, N) \quad (4.1)$$

Linear interpolation was performed to locate the temperature value at non-integer pixel numbers. Using the curve of temperature as a function of time, t_{diff} was determined, and the results of all nine experimental conditions and three replicates are listed in Table 8.

Table 8 Results of effective diffusion time under experimental condition

t_{diff} (s)	1 st replicate	2 nd replicate	3 rd replicate	Avg.	Std.
1	0.1135	0.1140	0.1139	0.1138	2.95E-04
2	0.0782	0.0781	0.0778	0.0780	2.15E-04
3	0.0609	0.0608	0.0605	0.0607	1.98E-04
4	0.0779	0.0775	0.0772	0.0775	3.43E-04
5	0.0604	0.0598	0.0593	0.0598	5.47E-04
6	0.1221	0.1238	0.1229	0.1229	8.13E-04
7	0.0590	0.0591	0.0587	0.0589	2.01E-04
8	0.1223	0.1214	0.1204	0.1213	9.51E-04
9	0.0809	0.0839	0.0818	0.0822	1.52E-03

Table 8 suggested that t_{diff} of all experimental conditions was of the magnitude of 0.1 s. This result was compared to the study of Dinwiddie et al. [47], which used an IR camera to monitor another desktop-level 3D printer using ABS as the printing material. With a 25.07 mm/s printing speed, they found that the temperature of the first layer dropped from 255°C to 115°C in about 0.3 s for a square sample with 4 inches (101.6mm) of length. However, theoretical models reviewed by Bellehumeur et al. [31] predict that diffusion time would be seconds, which contradicts the experimental observations. This discrepancy was believed to be caused by incorrect boundary conditions, temperature-

independent thermophysical properties of the material, and the assumption applied in the theoretical models that the phase change effect is negligible.

To analyze the effects of the printing parameters, an evaluation of signal-to-noise (S/N) ratio was conducted. In a parametric study, S/N ratio was designed to quantify how the response varies to noise factors and signal factors under different noise conditions. Since this study aims to prolong the diffusion time, characteristics ‘the larger the better’ were selected, and the S/N ratio was calculated based on

$$S / N = -10 \log \left(\frac{1}{p} \sum_{i=1}^p t_{\text{diff},i}^2 \right) \quad (4.2)$$

where p is the number of replicates, of which there are three in this study. The results of the S/N ratio analyses are plotted in Figure 28.

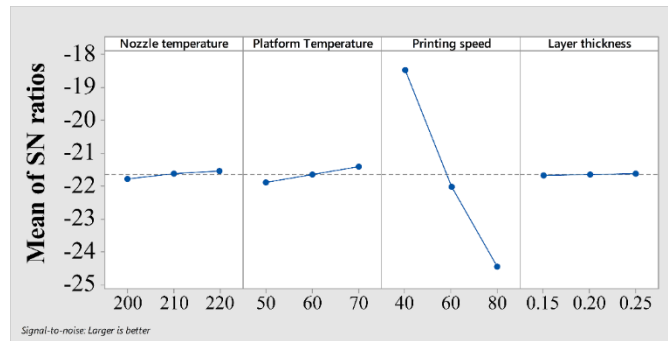


Figure 28 Results of S/N ratio of effective diffusion time under experimental condition

In Figure 28, the printing speed has the most significant influence on diffusion time, followed by platform temperature, extrusion temperature, and layer thickness. The S/N ratio results suggest that PLA would have the longest diffusion time at the nozzle temperature of 220°C, platform temperature of 70°C, printing speed of 40 mm/s, and layer thickness of 0.25 mm.

Additionally, statistical analyses of the experiment result were performed using ANOVA. The results of ANOVA are listed in Table 9; the p-value of all four factors was lower than 0.05, indicating that they all significantly contribute to the response. The importance of factors for effective diffusion times was ranked as follows: printing speed>>platform temperature>nozzle temperature>layer thickness, which corresponded to the S/N ratio results.

Table 9 Results of ANOVA analysis on effective diffusion time under experimental condition

Source	DoF	Adj-SS	Adj-MS	F-value	p-value
Nozzle temperature	2	5.5000E-05	2.7000E-05	5.4660E+01	<0.001
Platform temperature	2	1.2300E-04	6.1000E-05	1.2222E+02	<0.001
Printing speed	2	1.6579E-02	8.2890E-03	1.6520E+04	<0.001
Layer thickness	2	1.0000E-05	5.0000E-06	1.0210E+01	0.001
Error	18	9.0000E-06	0.5000E-06		
Total	26	1.6775E-02			

4.2. Numerical model

4.2.1. Grid independence test

The grid independence test for thermal analysis was performed to evaluate the effects of grid sizes on the results as shown in Figure 29. Four sets of mesh were generated with the element size varied from $0.25\text{mm} \times 0.25\text{mm} \times \text{Layer thickness}$ to $2\text{mm} \times 2\text{mm} \times \text{Layer thickness}$. The test configuration is printing PLA material for 0.2s with the printing speed of 40mm/s. The deposition temperature, platform temperature, and layer thickness are 210°C , 60°C , and 0.15mm, respectively. In total, there is 8mm of material extruded, and the temperature distribution of it was used for compared the performance of the numerical model with different mesh numbers. In each layer, there are 3440, 864, 200, and 110 elements for element size of 0.25, 0.5, 1, and 2mm, respectively. It was observed the element size of 1mm and 0.5mm produced results with a percentage error of less than 3%. Hence, a domain with the element size of 1mm was chosen to reduce the computing time. Considering the element size divided by time step is the printing speed, which is a constant in this scenario; therefore, the grid independence test also served as the time step independence test.

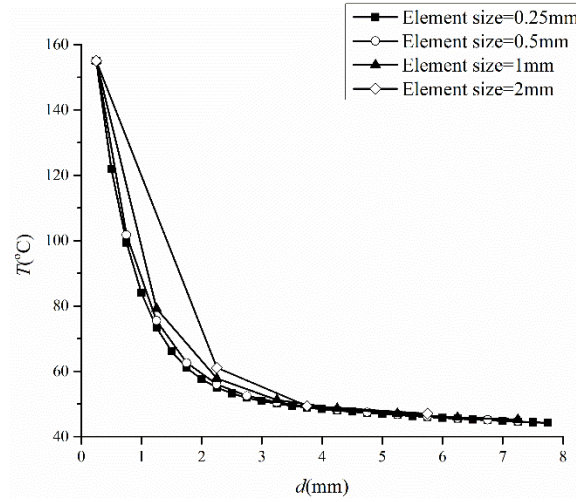


Figure 29 A plot of temperature distribution curves with regard to element size

4.2.2. Determination of convective heat transfer coefficient

Based on the methodology introduced in section 3.2.3, convective heat transfer coefficient and interfacial conduct resistance were estimated using ANN [111]. The average values of them from 100 training processes are 2894 and 61.72 W/(m²·K). The distribution of both values over those 100 networks were plotted in Figure 30, which can be seen that most of the data were concentrated near the average values while a few of them were far away. The random selected training/validation/testing caused such deviation between each constructed network. In addition, the temperature history of the

¹⁰ This section is reprinted with permission from Zhou, X., & Hsieh, S. J. (2018, May). Evaluating convective heat transfer coefficients in fused deposition process using infrared imaging and neural networks. In *Thermosense: Thermal Infrared Applications XL* (Vol. 10661, p. 106610K). International Society for Optics and Photonics. Copyright 2018 by SPIE

measured points under experimental and simulation conditions was given in Figure 31, which demonstrated that the deviation between them is small.

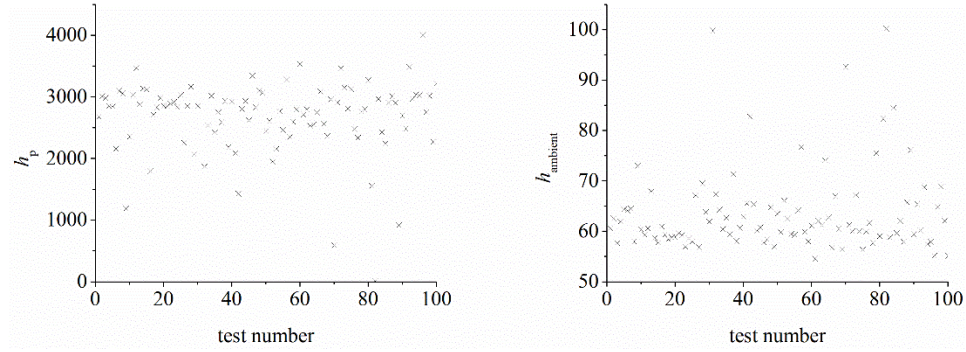


Figure 30 Plots of calculated h_p (left) and $h_{ambient}$ (right) in 100 networks

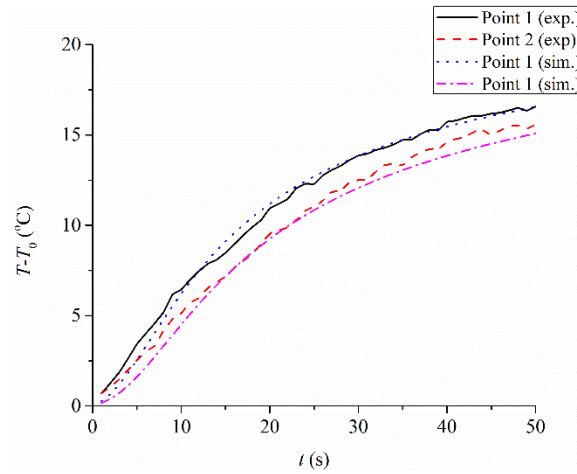


Figure 31 A plot of temperature history of two points under experimental and numerical conditions

4.2.2.1 Uncertainty analysis

One of the issues in solving IHCP is the estimation of the experimental uncertainty.

Inverse results usually do not come with clear statements of the uncertainty due to the difficulties associated with the non-uniqueness of inverse solutions [131]. With regards to ANN models, it is demonstrated that prediction error comes from measurement uncertainty and uncertainty of the inferred network parameters [132]. However, the quantification of uncertainty in ANN is still challenging due to its parallel computing architecture, which consequently limits its application in solving the real-world problems. Therefore, investigation of quantifying the uncertainty in neural networks has never been ceased. In this study, the approach of Monte Carlo method, also known as resampling method would be used. It is a probabilistic-based approach which samples different realization of model inputs or parameters by assigning the probability distribution of each variable [133].

The following assumptions are made to evaluate the time for the temperature to reach 5 degrees higher than the initial temperature:

- [1] Noise equivalent error of 0.25K on both initial and end of temperature measurement based on infrared camera specification

[2] The surface temperature measurement values could be represented by continuous uniform distribution [117]

$$f(T) = \begin{cases} \frac{1}{2a} & \text{for } \bar{T} - a \leq T \leq \bar{T} + a \\ 0 & \text{otherwise} \end{cases} \quad (4.3)$$

where a is the variation of the temperature measurement error.

[3] Temperature changes linearly inside of the measurement time interval

With all these assumptions considered, a time measurement uncertainty of 0.16s was calculated for both input nodes of the network model. Two scenarios were considered for the sources that error could be induced.

The first scenario is the error was induced from the training dataset. Since numerical simulation results instead of experimental measurement results were used to train the neural network model, less accurate cases in the simulation model could potentially arise the estimation error after neural network training [66]. Assuming an uncertainty of 0.16s exists for the training dataset, each node was then resampled 200 times with continuous uniform distribution followed for all 100 simulation conditions. Subsequently, 20,000 (100 runs for average value for all 200 resampled inputs) neural networks were trained. The evaluation results with the experimental data as the input were sorted and plotted in Figure 32 as the cumulative probability function.

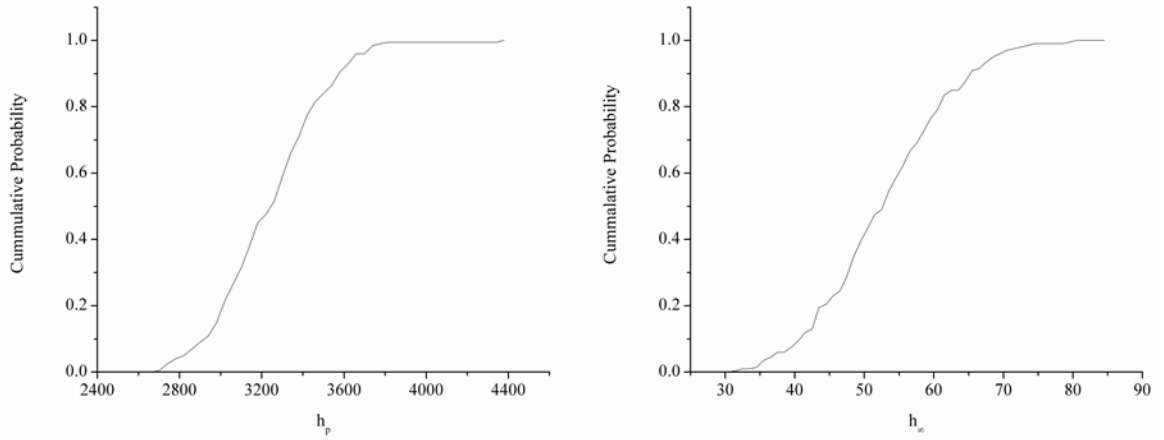


Figure 32 The cumulative probability function of estimation results with error induced from training for h_p (left) and h_∞ (right)

It is discovered that the shape of both cumulative probability functions resembles that of Gamma distribution. Therefore, distribution fitting was performed and two-sample Kolmogorov-Smirnov test was conducted to evaluate the goodness-of-fitting. With the null hypothesis that the original data and the fitted data are from the same distribution, at the significance level of 5%, the p-value of h_p and h_∞ is 0.6107 and 0.7787, respectively. The statistical testing results indicate that the null hypothesis was not rejected for both values. It is concluded that with the distribution of $h_p \sim \text{Gamma}(160.6878, 20.2796)$ and $h_\infty \sim \text{Gamma}(30.8877, 1.7218)$, and the uncertainty was 472.0 (14.4%) and 17.96 (33.8%) for h_p and h_∞ , respectively.

Secondly, for error induced from testing scenario, it is assumed that the neural network model is trained properly and tested with experimental data with uncertainty. The experimental data was assumed to follow continuous uniform distribution and resampled 1000 times. the resulted distribution curve was plotted in Figure 33.

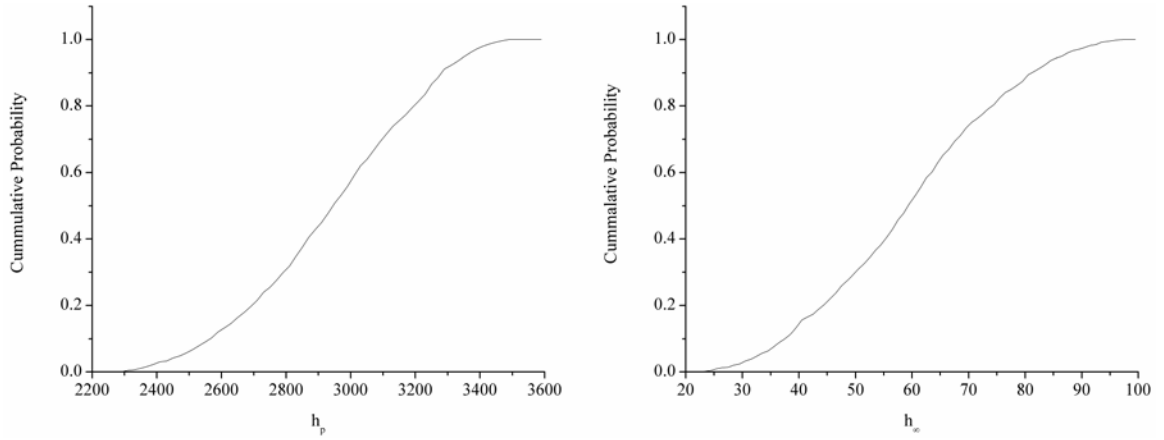


Figure 33 The cumulative probability function of estimation results with error induced from testing for h_p (left) and h_∞ (right)

It is observed that both resulted distribution curves seem to follow the shape of normal distribution. With Shapiro–Wilk test conducted, it is proved that both datasets were not significantly drawn from a normal distributed population at 5% level. And the uncertainty associated with h_p and h_∞ is 495.3 (16.82%) and 30.42 (50.96%).

Through the above analysis, it is evident that the accuracy of h_{∞} is significantly impacted by the measurement error. It is expected that using high-performance infrared imaging device with a lower noise equivalent error ($<20\text{mK}$) could reduce the estimation uncertainty to below 5%.

4.2.3. Validation of simulation results

The effective diffusion time was measured experimentally and simulated numerically under all nine conditions; the results are listed in Table 10.

Table 10 Comparison of experimental, numerical, and literature value of effective diffusion time

	$t_{\text{diff, exp}}$ (s)	Std_{exp} (s)	$t_{\text{diff, sim}}$ (s)	Bias (%)	$t_{\text{diff, sim, lit}}$ (s) (Zhang 2006)	Bias (%)	$t_{\text{diff, theo, lit}}$ (s) [30]	Bias (%)
1	0.1138	2.95E-04	0.0528	53.61	0.0709	37.66	2.8379	2394
2	0.0780	2.15E-04	0.0685	12.19	0.0856	9.70	5.1339	6482
3	0.0607	1.98E-04	0.1133	86.64	0.1447	138.35	11.5741	18968
4	0.0775	3.43E-04	0.0761	1.82	0.0822	6.02	4.9297	6261
5	0.0598	5.47E-04	0.0579	3.17	0.0744	24.42	5.9524	9854
6	0.1229	8.13E-04	0.0993	19.24	0.1939	57.76	7.7553	6210
7	0.0589	2.01E-04	0.0589	0.07	0.0697	18.28	5.5735	9363
8	0.1213	9.51E-04	0.1280	5.51	0.0797	34.32	4.7799	3841
9	0.0822	1.52E-03	0.0718	12.65	0.2564	211.97	10.2577	12379

For layer heights of 0.15, 0.20, and 0.25 mm, the element in the middle of the front filament of the 7th, 5th, and 4th layer, respectively, was chosen to calculate diffusion time

during the simulation. The experimental and simulation values were generally of the same magnitude, and in 6 of 9 cases, the biases were less than 13%. However, significant discrepancies exist in case Nos. 1, 3, 6, and 9. We presumed that this difference was caused by inaccurate modeling of the platform heat transfer mechanism. One common feature of condition Nos. 3, 6, and 9 was that the platform temperature was set at the highest level, indicating that the boundary condition at high platform temperatures might require further improvements. With the reduction of the nozzle temperature, the temperature of the material upon deposition would decrease to a value closer to that of the platform, leading to a more dominant platform temperature effect. As a result, the discrepancy became huge in condition Nos. 1 and 3. The thermal contact resistance value we used between PLA-PLA interface was an estimated value based on experiments with other polymer materials. The availability of future experimental data regarding thermal contact resistance on the PLA-PLA interface will improve the accuracy of the simulation model. A S/N ratio analysis was also carried out using Eq 4.2 for the numerical conditions.

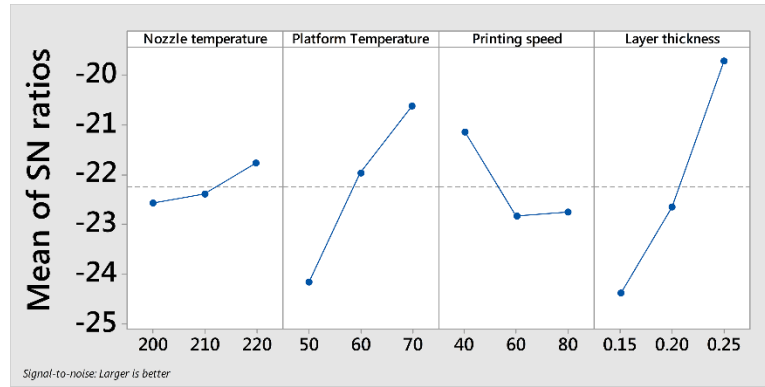


Figure 34 A S/N ratio of effective diffusion time under numerical condition

Figure 34 suggests that PLA would have the longest cooling diffusion time at a nozzle temperature of 220°C, a platform temperature of 70°C, a printing speed of 40 mm/s, and a layer thickness of 0.25 mm, which is consistent with the experimental results.

However, the effect of layer thickness becomes the most significant factor rather than the printing speed, which can be explained using cases with low levels of layer thickness (Nos. 1, 5, and 9). Those simulation results were lower than the experimental results, where for the cases with the thickest layers (Nos. 3, 4, and 8), the simulation results were higher than the experimental results. This discrepancy enlarges the effect of layer thickness, causing it to surpass the impact of printing speed.

Moreover, the results of the experiments and simulation models were compared to the existing literature. Zhang and co-workers presented their simulation result of the FDM process, which assumed that deposition temperature is equal to nozzle temperature [33].

Under these assumptions, the effective diffusion time was evaluated based on the same geometry and material properties of the previously used model, and the results are shown in Figure 34. Li et al. [30] proposed using the lumped capacity analysis to model the cooling processes of the extruded filament in FDM process. The analytical solution they developed to predict diffusion time is

$$t_{\text{diff}} = \log\left(\frac{T_g - T_p}{T_d - T_p}\right) / (-mv) \quad (4.4)$$

$$\text{with } m = \frac{\sqrt{1 + 4\alpha\beta} - 1}{2\alpha}, \alpha = \frac{k}{\rho C_p v}, \text{ and } \beta = \frac{hP}{\rho C_p A v}$$

where A and P represent the cross-section area of the filament and the perimeter of it, respectively. With the material properties of PLA evaluated at 400K and h set to only the forced convection value ($88 \text{ W}\cdot\text{m}^{-2}\cdot\text{K}^{-1}$), the results from the theoretical predictions are also presented in Figure 35.

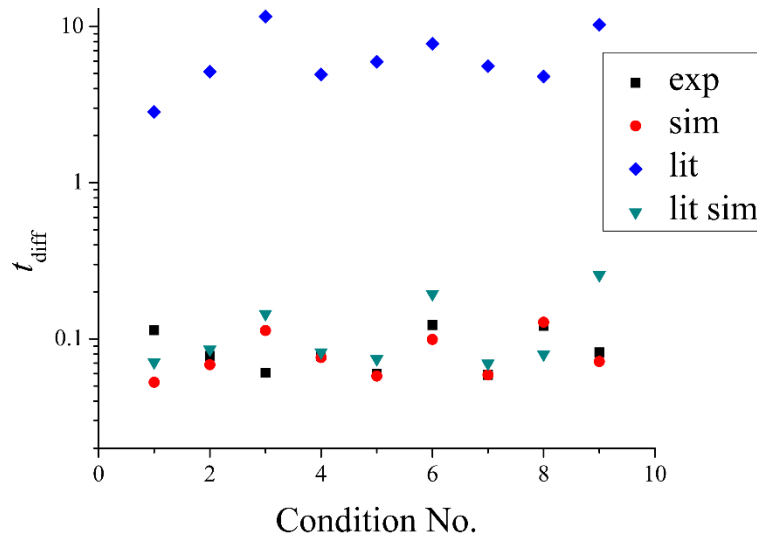


Figure 35 A comparison of effective diffusion time in this study and previous literature

Figure 35 suggests that the simulation model of this paper generated better-correlated results with the experimental data compared with other methods. Taking the assumption that the deposition temperature is identical to nozzle temperature, the reviewed simulation model has a more substantial error. However, their results still had the same magnitude of 0.1 s. Alternatively, the existing theoretical model predicted the diffusion time one magnitude higher than the experimental model, suggesting that conduction between the platform and layers beneath the platform are the largest heat loss source.

4.2.4. *Simulation results on distortion and thermal stress*

Deformation and thermal stress distributions of the simulation model were obtained by applying temperature history of the nodes as the thermal load in the structural analysis.

The contour of z-direction distortion of the model in condition No. 6 was plotted in Figure 36. It can be observed from the top view that the vertical distortion of the part was mostly uniform across the horizontal direction, and a distortion gradient only exists on four rectangular interior and exterior corners in each layer. For all nine conditions, the trend remained consistent when the time of the observation was right after the top layer was manufactured. The maximum vertical distortion values, however, were different for separate conditions, and they are listed in Table 11.

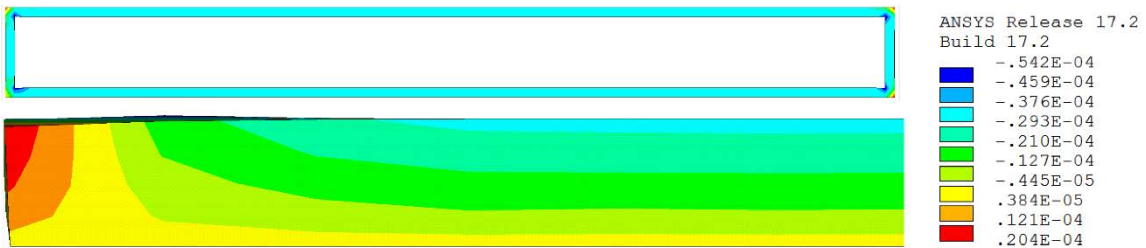


Figure 36 A contour image of z-direction distortion of the model

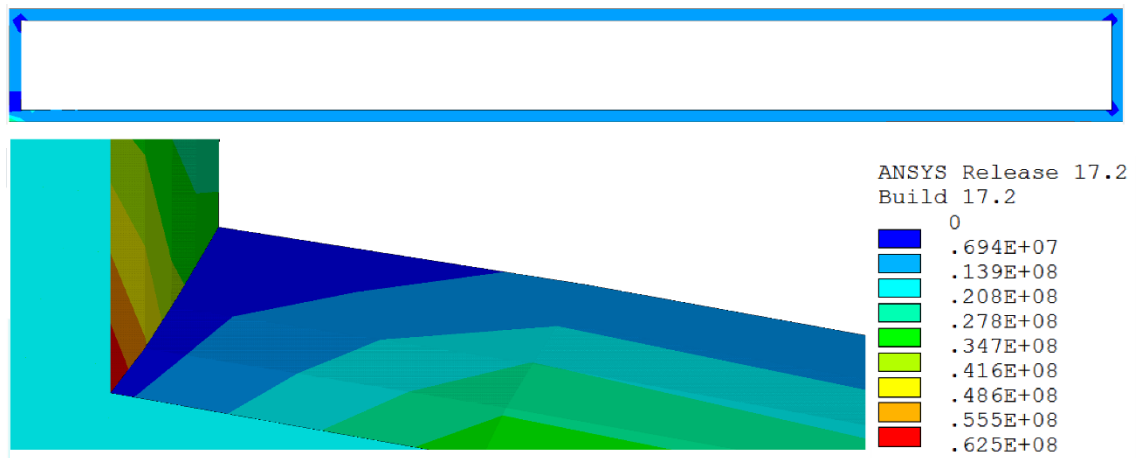


Figure 37 A contour image of residual stress of the model

Figure 37 demonstrates an example of the von Mises stress distribution of the simulation model in condition 6. Stress was concentrated near the corners, but the highest stress was near the most recently deposited material, where temperature gradient was the greatest. The highest von Mises stresses for each condition in the developed simulation model are also listed in Table 11.

Table 11 The highest von Mises stresses for each condition in the developed simulation model

No.	1	2	3	4	5	6	7	8	9
Distortion (mm)	0.147	0.200	0.215	0.227	0.154	0.204	0.213	0.230	0.158
Stress (Mpa)	57.4	61.2	63.6	60.1	59.9	62.5	60.3	61.2	61.3

The S/N ratio analyses were performed based on the results of Table 11 to evaluate the effect of printing parameters on the vertical distortion and maximum thermal stress. The smaller-the-better principle was adopted because we want to minimize the distortion and residual stress.

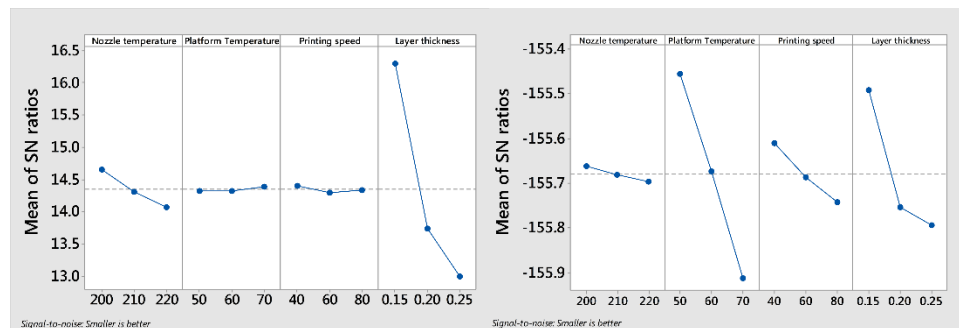


Figure 38 S/N ratio plots for distortion (left) and residual stress (right)

Figure 38 illustrates that the layer thickness is the most significant parameter affecting vertical distortion of the simulation models. Minimizing the vertical distortion of the simulation models is associated with the decrease of the extrusion temperature, printing

speed, and layer thickness, as well as the increase of the platform temperature. This result showed good agreement with the literature. Nancharaiah et al. [63] reported that using thinner layers could increase dimensional accuracy in experimental design. Sahu et al. [60] also discovered that reducing layer thickness leads to better dimension accuracy on the vertical side. Peng et al. [65] combined response surface methodology with a fuzzy inference system and found that lower filling velocity and extrusion velocity help reduce the warp formation. Xinhua et al. concluded that a low nozzle temperature is helpful to reduce the distortion on a PLA-made thin-plate [61].

Figure 38 compared the effect of four printing parameters on the maximum von Mises stress. All four parameters were positively correlated with the response, and the platform temperature had the most significant impact. This finding is consistent with Kantaros et al.'s experimental result, where they also reported that residual strain of the FDM part would decrease with layer thickness [54].

4.3. Discussion

For an FDM process using polymer materials, there are two non-included phenomena that could potentially affect the accuracy of a numerical prediction model. The first is structural relaxation. When a polymer material is cooled from above to below T_g , the resulting glass is unstable, and the density will gradually increase with time [134]. The structural relaxation process towards thermodynamic equilibrium occurs rapidly at temperatures around T_g , and it caused a 3% density value change for polystyrene resin.

The second phenomenon is the wetting/bonding process. In the FDM process, the bonding of filaments occurs when adjacent filaments come into contact, and the temperature is above T_g . To the best knowledge of the authors, there is no existing literature that applies polymer bonding theory to the numerical simulation of FDM. Although for the model constructed in this paper, the impact of filament bonding on the experimental result was reduced to the minimum because the layers studied did not have an infill pattern (no inter-layer bonding); an accurate modeling is still required when considering the deposition pattern. Two dominant theories existed for modeling the bonding process—the healing theory [135] and the sintering theory [31]. Both theories predicted that the volume of the filaments would gradually decrease due to diffusion of the interface when they were brought into good contact at a temperature above the glass transition. This process could be adopted in the current numerical simulation by modeling density as a function of element activation time and nodal temperature. However, the correlation between printing parameters and function coefficient still requires intensive experimental and theoretical investigation.

4.4. Summary

In this section, the thermal behavior of the FDM process was studied both experimentally and numerically; and the effects of nozzle temperature, platform temperature, extrusion speed, and layer thickness on effective diffusion time, maximum vertical distortion, and maximum thermal stress were evaluated.

In the experimental investigation, the thermal history of the FDM process was measured by a co-axial, low-cost, infrared sensor moving with the nozzle. The experimental results revealed that PLA would have the longest diffusion time at high nozzle temperature, high platform temperature, low printing speed, and high layer thickness.

Based on the boundary condition measured by the experiments, a predictive finite element model for the FDM process was developed. For the same geometry model and printing parameters, the simulation model could predict the effective diffusion time with a bias less than 13% in six out of nine conditions, which was relatively lower than the existing simulation and theoretical prediction models in the literature. The developed numerical model revealed that reducing extrusion temperature, slowing printing speed, and decreasing layer thickness could help reduce the vertical distortion and residual thermal stress, while the high platform temperature might have opposing effects on distortion and residual stress.

5. RESULTS AND ANALYSIS OF MECHANICAL BEHAVIOR OF FDM MANUFACTURED POLYLACTIC ACID PARTS

In this section [66], analysis for mechanical behavior experimental and numerical model was performed. Analysis of tensile testing experimental data on unidirectional and bidirectional samples were first carried out in Section 5.1. Validation of the simulation model was conducted in Section 5.2 along with the stress analysis. Finally, Section 5.3 presented of prediction results of stress-strain relationship.

5.1. Experimental model

5.1.1. Analysis of stress-strain relationship

As mentioned in section 3.3.1, each specimen went through the tensile testing procedure with force-displacement data recorded. Therefore, stress-strain curves were plotted for each of them, which were shown in Figure 39 and Figure 40.

¹¹ This section is reprinted with permission from *Modelling and estimation of tensile behaviour of polylactic acid parts manufactured by fused deposition modelling using finite element analysis and knowledge-based library* by Xunfei Zhou, Sheng-Jen Hsieh & ChenChing Ting Virtual and Physical Prototyping (2017).. Copyright 2018 by Taylor & Francis Group

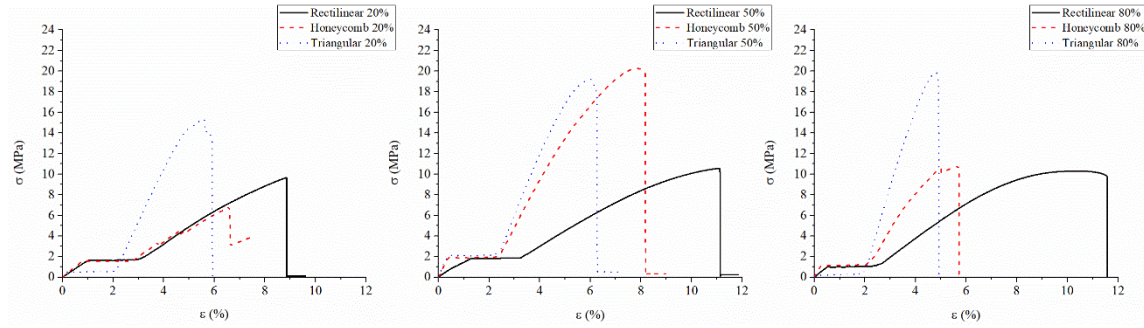


Figure 39 Stress-strain curves for unidirectional samples under tensile testing

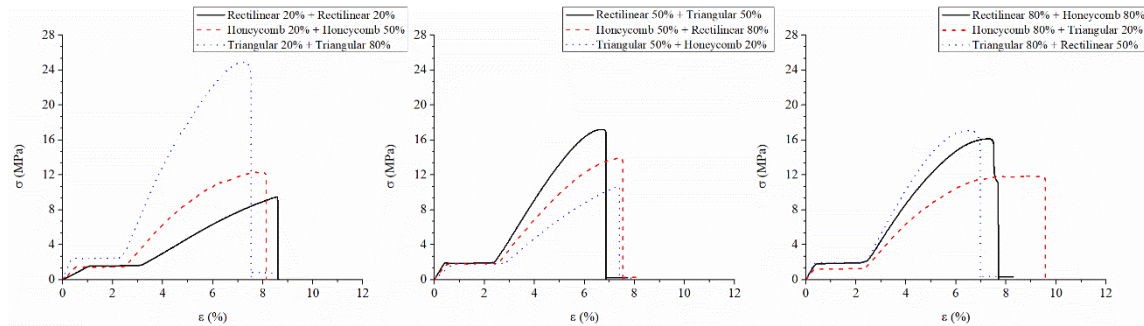


Figure 40 Stress-strain curves for bidirectional samples under tensile testing

For all samples, the behavior of the stress-strain curves was consistent with the nature of PLA—a semi-crystalline thermoplastic polymer. Linear elastic deformation first appears where amorphous regions elongated; then it follows with the formation of the neck where crystalline areas align; those crystalline regions start to slide (cold drawing); the fully drawn sample begins being stretched (strain hardening); and in the end, the fibers fracture. An illustration of this process was given in Figure 41, using a sample with rectilinear infill pattern with the infill density of 50%. The PLA samples manufactured

by FDM did not exhibit an obvious post-yield softening or neck formation effect. Moreover, the cold drawing region appeared to last for at least 1% of the strain change (natural draw ratio > 1%). In this “stable-necking” region, the stress was approximately constant as the neck propagated along the length of the specimen. The long fracture strain of the samples in Figure 39 and Figure 40 indicated a strong interior molecular chain orientation phenomenon, which accompanied the extension and slippage phenomena.

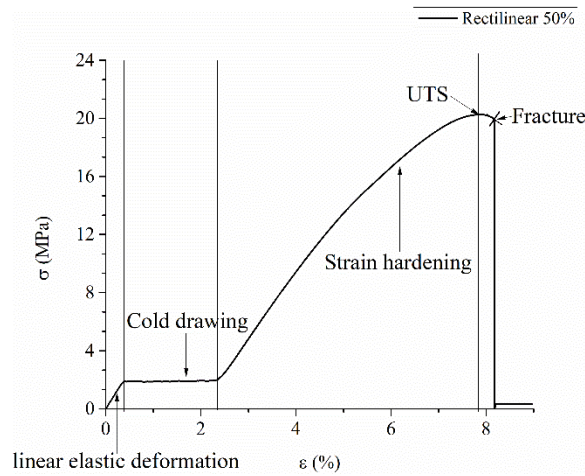


Figure 41 An illustration of semi-crystalline polymer stress-strain curve

5.1.2. Analysis of the modulus of elasticity and UTS

For a semi-crystalline polymer, the slope of the tangent to the stress-strain curve at small stress values is usually taken as the modulus of elasticity [35], and the UTS is defined as

the highest point of the stress-strain curve. In this study, UTS and the modulus of elasticity values for all specimens are summarized in Table 12.

As demonstrated in Table 12, the initial slopes of stress-strain curves, representing Young's modulus E , showed significant differences, depending on the infill pattern. For most cases, there was no doubt that increasing infill density, the proportion of solid fibers to the air gap in the same cross-section area, increased the tensile strength. While comparison of different infill patterns revealed that the rate of UTS increase over infill density is rather low for rectilinear pattern. Previous research [136] showed that 0° raster orientation (raster parallel to the direction of pull force) possessed mostly the highest values for ultimate strength and was relatively insensitive to the increase of infill density. The filament geometry in Figure 6 demonstrated both triangular and honeycomb structure would have such a full or partial 0° raster in the middle of neck region while rectilinear pattern does not have. Therefore, in this case of rectilinear infilled samples, the inter-raster fusion bonds between adjacent rasters withstood most of the applied load with very few rasters pulled along their longitudinal axis.

Table 12 Tensile strength and the modulus of elasticity of all samples tested

Unidirectional Specimens					
No.	Printing pattern	UTS (MPa)	Modulus of elasticity in linear region (MPa)	Weight (g)	UTS/weight (MPa/g)
1	20% Rectilinear	9.41±0.25	149.7±5.7	2.49±0.06	3.79
2	20% Honeycomb	6.31±0.52	194.7±11.5	2.29±0.01	2.75
3	20% Triangular	15.87±0.49	396.7±72.7	2.53±0.00	6.26
4	50% Rectilinear	10.14±0.41	139.8±1.9	3.64±0.01	2.79
5	50% Honeycomb	19.53±0.74	483.7±13.5	3.65±0.01	5.35
6	50% Triangular	18.26±0.96	534.0±11.4	3.59±0.07	5.09
7	80% Rectilinear	10.48±0.18	177.2±13.9	5.27±0.00	1.99
8	80% Honeycomb	10.72±0.00	339.4±13.5	4.65±0.01	2.31
9	80% Triangular	20.39±0.53	699.0±9.8	5.43±0.00	3.75
Bi-directional Specimens					
No.	Printing pattern	UTS (MPa)	Modulus of elasticity in linear region (MPa)	Weight (g)	UTS/weight (MPa/g)
1	20%R + 20%R	9.57±0.08	139.6±4.5	2.40±0.01	3.99
2	20%H + 50%H	12.35±0.03	249.4±3.8	3.06±0.02	4.04
3	20%T + 80%T	24.42±0.48	491.3±23.2	4.26±0.02	5.74
4	50%R + 50%T	17.05±0.15	452.9±16.2	3.52±0.00	4.84
5	50%H + 80%R	13.79±0.11	358.4±8.9	4.53±0.02	3.04
6	50%T + 20%H	10.55±0.16	246.2±7.3	3.05±0.01	3.46
7	80%R + 80%H	15.92±0.21	432.2±16.0	5.04±0.02	3.16
8	80%H + 20%T	11.82±0.04	348.8±16.7	3.55±0.02	3.33
9	80%T + 50%R	16.70±0.35	537.8±11.0	4.55±0.00	3.67
10	20%R + 20%R	9.31±0.63	171.04±4.88	2.45±0.02	3.80
11	50%H + 20%H	11.28±0.36	323.74±0.59	2.78±0.01	4.06
12	80%T + 20%T	25.20±0.20	482.13±6.62	3.85±0.00	6.54
13	50%T + 50%R	17.54±0.07	521.51±0.67	3.79±0.01	4.63
14	80%R + 50%H	14.47±0.10	397.39±0.35	4.23±0.02	3.42
15	20%H + 50%T	9.10±0.22	286.07±6.41	3.01±0.00	3.03
16	80%H + 80%R	17.10±0.14	476.08±7.19	4.95±0.04	3.45
17	20%T + 80%H	12.91±0.15	369.41±3.56	3.81±0.04	3.39
18	50%R + 80%T	16.55±0.15	558.77±2.98	4.86±0.06	3.41

For unidirectional specimens, the triangular infill pattern, especially at 20% infill density, possessed the highest strength/weight ratio—the part is both light and resistant. And for bidirectional samples, it appeared the tensile behavior varied slightly between the samples with layer structures reversed through comparing the results of sample #1-9 and sample #10-18. To analyze the effect of infill geometries on bidirectional specimens, which have two distinct patterns at the cross-section area, the S/N ratio method could be applied, with the results plotted in Figure 42. Figure 42 shows that for bidirectional specimens, increasing UTS benefits from minimizing the air gap and using a triangular infill pattern. However, considering the strength/weight ratio, 20% infill density was the most cost-effective option. While the triangular infill pattern has better performance compared to the rectilinear infill pattern, the honeycomb structure seems to have the lowest strength of the manufactured parts.

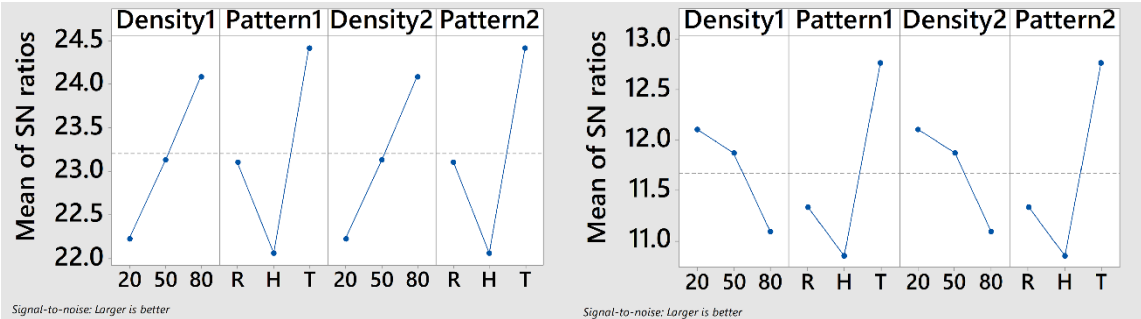


Figure 42 S/N ratio analysis for UTS (left) and UTS/weight ratio (right)

5.2. Numerical model

5.2.1. Grid and time step independence test

Similar to section 4.2.1, both grid and time step independence tests were performed on analysis of mechanical behavior. Mesh was generated with the size of 0.5 to 1.5 mm to evaluate size's effect on load force. The result of specimen #2's load force at 1s versus node number was plotted in Figure 43.

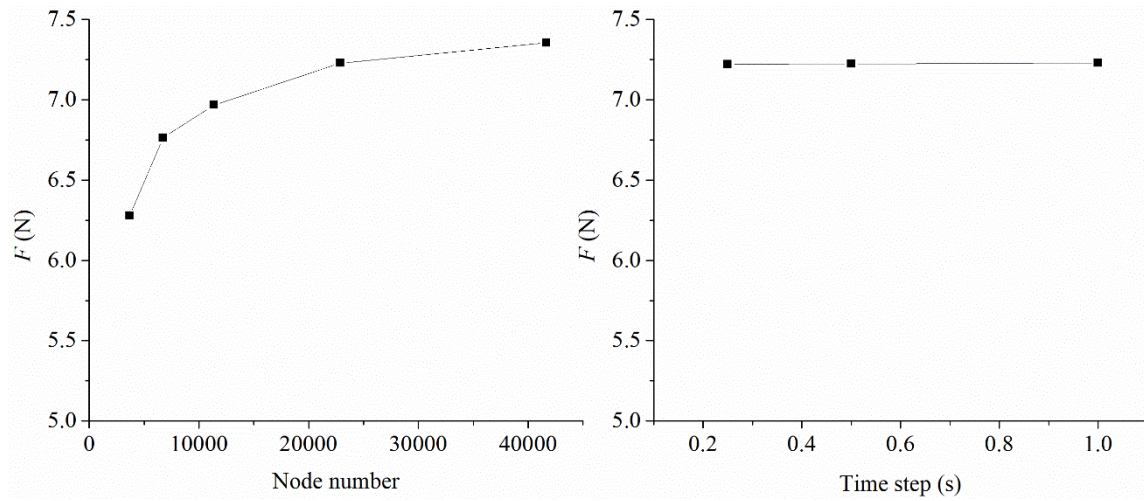


Figure 43 Plots of load force over node number (left) and time step (right)

It is observed that although the load force tends to increase with the node number, refine the mesh size from 0.6mm (total nodes of 22876) to 0.5mm (total nodes of 41689) only resulted in a difference of 1.72% in the result. Therefore, with computation time and accuracy both considered, the element size of 0.6mm was used in this study. In addition, the influence of time step on numerical results was investigated and plotted in Figure 43

as well. It is found time step only has a minimal impact on the calculated load force.

Hence a time step of 1s was used.

5.2.2. Results of effective elastic modulus on unidirectional samples

The effective elastic modulus of the numerical model was calculated based on the load force applied at 1 s (strain rate of 0.14%), compared with the modulus of elasticity in the linear region from the experiment. The results are shown in Table 13.

Table 13 The modulus of elasticity of unidirectional samples obtained by MS approach and experiments

No.	Printing pattern	Load force in numerical model (N)	Numerical modulus of elasticity in linear region	Experimental modulus of elasticity in linear region	Error (%)
1	20% Rectilinear	4.65	154.04	149.7±5.7	4.39
2	20% Honeycomb	6.14	206.20	194.7±11.5	5.93
3	20% Triangular	9.82	329.82	396.7±72.7	16.86
4	50% Rectilinear	4.78	160.57	139.8±1.9	14.90
5	50% Honeycomb	6.41	215.34	483.7±13.5	55.48
6	50% Triangular	17.49	587.63	534.0±11.4	10.05
7	80% Rectilinear	4.83	162.16	177.2±13.9	8.50
8	80% Honeycomb	6.50	218.48	339.4±13.5	35.62
9	80% Triangular	22.70	762.67	699.0±9.8	9.11

Table. 11 lists the calculated and measured modulus of elasticity in two models, and in seven out of nine cases, the numerically calculated value is close to or within the margin of the experimental result. The error between the two approaches rose when the infill

fibres became denser in honeycomb structures, and it appeared finite element model tends to under-predict the effective modulus under those circumstances. The discrepancy suggested that both inter-layer and intra-layer filament bonding might play a vital role. From observing the manufactured part, it appeared filaments of adjacent honeycomb structure bonded firmly through the polymer sintering process [31], while miniature gaps and holes existed in the FEA model, potentially diminished the effective modulus. Moreover, the current FEA model could not accurately reflect the fiber bonding between layers. Scanning electron microscope (SEM) images [137] of the manufactured part revealed the presence of voids within the built specimen and ellipse-like shape of the filament which are difficult to recreate with the current meso-structure approach.

5.2.3. Analysis of stress concentration region on unidirectional samples

Another outcome of tensile testing experiments is sample breakage—at the location with the most stress. This site can be the target of further investigations into increasing the strength or redesigns, while FEA could potentially reduce the experimental cost if performed beforehand. The normal stress distribution in each numerical model at 1 s is shown in Figure 44, along with photos of the experimental samples after the break.

It is demonstrated that the developed model could predict the sample breakage point for 8 out of 9 cases which indicates FEA has the potential to be used as a stress visualization tool for additive manufacturing applications. In cases with a rectilinear and honeycomb infill pattern, Figure 44 shows that simulation models predict the maximum stress to

occur where the infill raster is in contact with outside contours, which is consistent with the fracture locations shown in the post-experiment images except for sample #6. Sharp corners induce high stress intensity, so smoother junctions in those patterns could possibility increase the part strength. Alternatively, in the triangular infill pattern, a horizontal raster, which behaves like a backbone, was added in the printing direction. Therefore, the structure load is primarily shared among three horizontal rasters, and the crack usually appeared simultaneously on them.

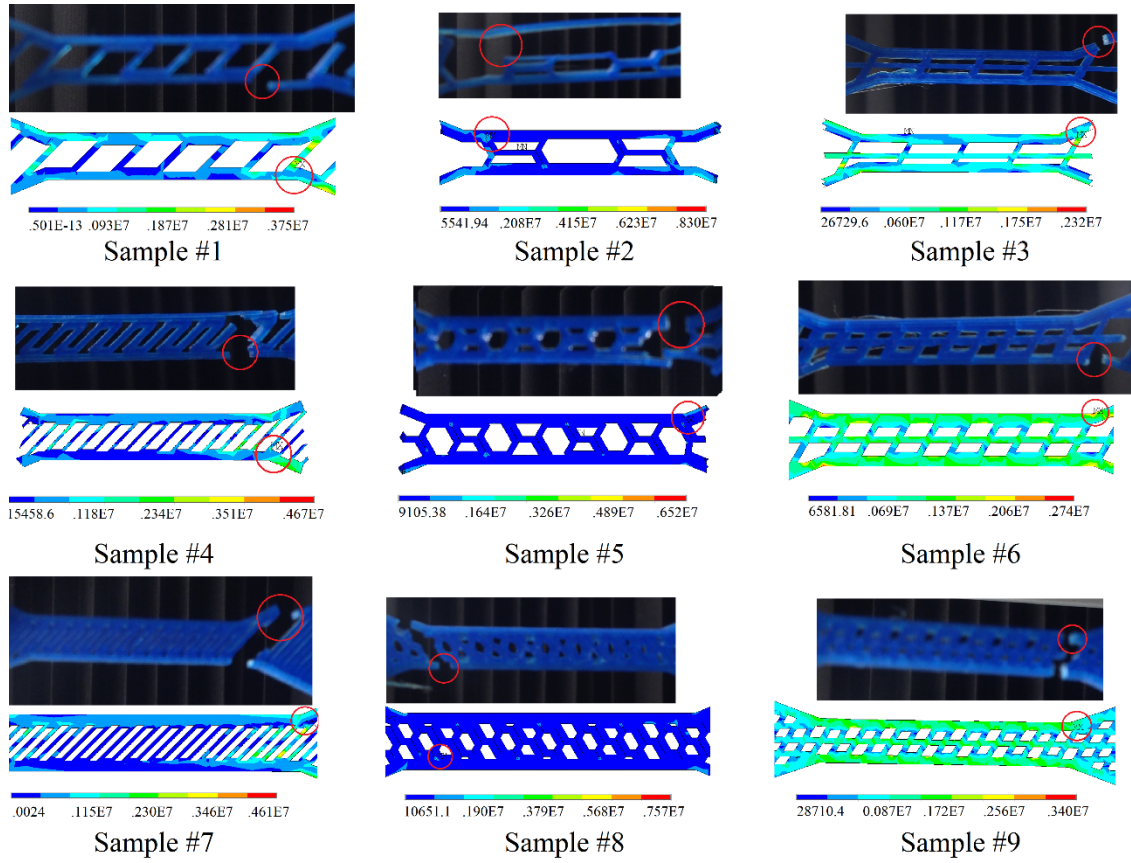


Figure 44 Fracture point in experimental and numerical conditions for sample #1 to #9

5.2.4. Analysis of effective elastic modulus on bidirectional samples

The tensile behaviour results of the bidirectional specimens obtained by the MS model, LC model, and experiments are presented in Table 14. To verify whether the differences between the proposed approach and the existing numerical simulation approach are statistically significant, a hypothesis was constructed so that the mean within-case

difference (errors between the proposed MS and LC methods) was zero, using the t test [138] for paired errors in Table 5 at a significance level $\alpha = 0.05$. With the expectation that the MS approach resulted in a smaller error than the LC approach when compared to the experimental values, the null hypothesis h_0 was set as $\overline{error_{MS}} - \overline{error_{LC}} \geq 0$, while the alternative hypothesis, h_1 , was $\overline{error_{MS}} - \overline{error_{LC}} < 0$. The resulting p-value was calculated as 0.01874, which indicated rejection of the null hypothesis. Therefore, the accuracy of the proposed MS approach was superior to the LC approach when predicting the effective modulus of elasticity of bidirectional samples.

The discrepancy between numerical and experimental results indicates that bonding between the two structures was not perfect and/or stress perturbations exist due to abrupt changes of structure. It is possible that failure strain of the low elongation fiber might be increased to that for a high elongation fiber by isolating the individual critical fiber failures, such that broken fibers are uniformly distributed throughout the parts.

Table 14 The modulus of elasticity of bidirectional samples obtained by MS approach, LCT approach, and experiments

No.	Printing pattern	Experimental modulus of elasticity in linear region	Load force in MS model	Modulus of elasticity in MS	Error (%)	Load force in LC model	Modulus of elasticity in LC	Error (%)
1	20%R + 20%R	139.6±4.5	4.58	154.04	10.7	5.40	161.41	16.0
2	20%H + 50%H	249.4±3.8	8.12	261.45	4.8	10.14	303.07	21.5
3	20%T + 80%T	491.3±23.2	13.76	443.29	9.8	12.90	385.55	21.5
4	50%R + 50%T	452.9±16.2	13.67	440.26	2.8	9.11	272.40	39.8
5	50%H + 80%R	358.4±8.9	10.24	329.79	8.0	9.69	289.56	19.2
6	50%T + 20%H	246.2±7.3	9.29	299.19	21.5	10.67	318.94	29.5
7	80%R + 80%H	432.2±16.0	8.13	261.98	39.4	9.14	273.26	36.8
8	80%H + 20%T	348.8±16.7	9.48	305.48	12.4	12.07	360.77	3.4
9	80%T + 50%R	537.8±11.0	16.68	537.52	0.0	12.91	385.88	28.2

5.3. Formulation of knowledge-based library

5.3.1. Implementing the knowledge-based library information system

Although using the numerical simulation model to predict the tensile behavior of parts manufactured by FDM has an acceptable accuracy, a major drawback is the required processing time. Although the automated script reduced the time required to generate the finite element model, hours of computation time are still required to simulate the tensile testing experiment with a complex infill geometry. Moreover, it is impractical to purchase and install multiple professional numerical simulation software packages to merely estimate the tensile behavior of the designed products. Implementing a knowledge-based library in the 3D printing software is a feasible approach whereby the user could know the estimated strength shortly after the printing parameters in the design

phase were changed. Consequently, regressing techniques were considered to formulate the prediction library with the results of a finite number of numerical simulation cases. Multivariate linear regression was first tested in this work, but the accuracy was questioned. The technique used in this study is the well-known ANN approach, which is a good candidate to correlate non-linear dynamic problems [85]. Typically, ANN consists of multiple layers of interconnected blocks, called neurons, that are used as linear or non-linear computing elements. Those layers are typically one input layer, one output layer, and one or more hidden layers; in this work, only one hidden layer was used, and the number of neurons in it varied from 2 to 20. Five hidden neurons performed best during training; thus, a 2-5-1 network topology was adopted, as shown in Figure 45. With the help of ANN, a library of the mechanical strength of the part with a varied printing pattern could be then constructed, and Figure 46 depicts the process of constructing such a library.

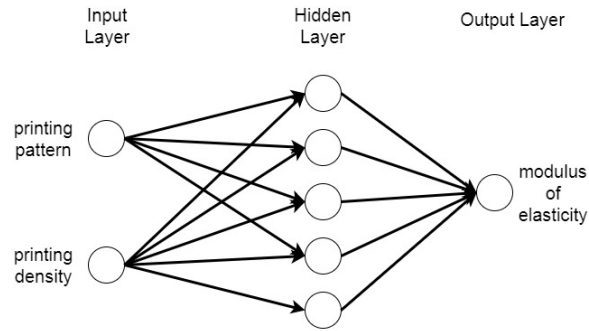


Figure 45 The ANN used to construct the knowledge-based library

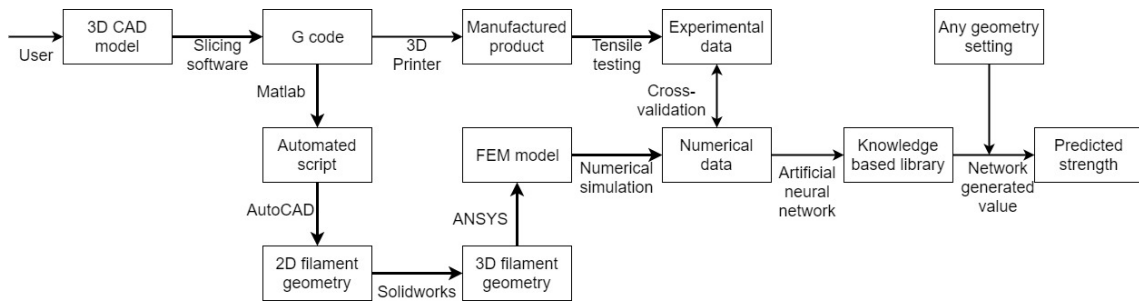


Figure 46 The flowchart of constructing the knowledge-based library

5.3.2. Cross-validation with extrapolation and interpolation

The accuracy of the numerical model for the current work is acceptable, with the involvement of machine learning technique while the accuracy of the predictive model is still questioned. Nine cases are relatively insufficient for building a training dataset;

therefore, nine more cases were included to build the training and testing subset, which was designed by interpolating and extrapolating the used infill density values, forming a dataset with three printing patterns and six different infill densities. Then, 18 cases were randomly divided into training, validation, and testing subsets with the ratio of 14:2:2, based on a rule of thumb. The subsets were divided, and the weights were randomly initialised. Then, the network was trained and evaluated 100 times, and the average performance value was chosen to improve network generalization. The resulting regression results were plotted in Figure 47, showing that the network achieved satisfactory performance, with an average prediction error of 14.80% after 100 trials.

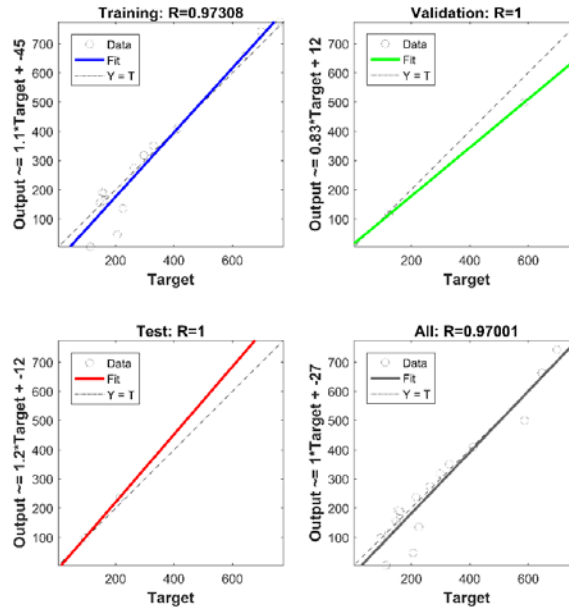


Figure 47 The regression performance of the developed network

For engineering application, an estimation/prediction model with estimation error less than 10% is usually regarded as an accurate one [42, 139], which shows there is still room to improve for the current proposed estimation model. It is believed the reasons causing the slightly higher prediction error are small training dataset and propagation of error from the numerical model itself. It is well recognized that neural networks trained with small datasets often exhibit unstable performance behavior, such as sporadic fluctuations due to the sensitive of network to the initial parameter values [140]. Moreover, network outputs can be affected by the order with which the training data is fed, leading to the potential of erratic outcomes [141]. Alternatively, less accurate cases in the simulation model (i.e. case #5 in Table 13) also arise the estimation error after

neural network training. Therefore, increasing training data for the knowledge base library, exploring other machine learning techniques, and improving the accuracy of numerical simulation model would be the next step of this work.

5.4. Summary

In this section, the mechanical behavior of the FDM process was studied both experimentally and numerically; the effects of the printing pattern and infill density on the ultimate tensile strength-weight ratio and the modulus of elasticity were evaluated. The stress-strain curves of FDM products were measured by tensile testing experiments, and the results indicated that if the air gap was minimized, the triangular infill pattern would be beneficial to UTS/weight ratio. Of the specimens considered, the 20% triangular pattern had the highest UTS/weight ratio. In the numerical investigation, the meso-structure approach does not require input from the unidirectional specimen stress-strain curves, and it could be used to predict the modulus of elasticity and breaking point in most cases. A knowledge-based library was constructed with the meso-structure numerical model and artificial neural network, and it could predict the modulus of elasticity of FDM manufactured polylactic acid with three infill patterns and any infill density with an average prediction error of 14.80%.

6. RESULTS AND ANALYSIS OF SURROGATE-BASED ADDITIVE MANUFACTURING OPTIMIZATION USING MULTI-FIDELITY MODELS

This section evaluated the performance of the developed optimization algorithm on various conditions. Several case studies were first performed in Section 6.1 to compare the performance of SAMO against existing methods. Then Section 6.2 identified factors could influence convergence rate of the developed optimizer.

6.1. Case studies

6.1.1. Case study 1—simple non-linear function

The optimizer developed in this study, SAMO, was first tested on a simple optimization problem— non-linear function with the form

$$\begin{aligned} \text{Maximize } y &= \frac{1000(x/10 + 3)}{(x/10)^2 + 100} \\ \text{subject to } 0 &\leq x \leq 1000, \text{ where } x \text{ is an integer} \end{aligned} \tag{6.1}$$

so that $y(x)$ can be changed from 1.0029 to 67.1141. The performance of SAMO algorithm was compared against SAO which is an experimental-only method introduced in section 2.5.2.3 and ARC which is an SBO-MFM method introduced in section 2.5.4.2. For the SAMO approach, the design space was initially sampled 50 times and evaluated in LF model and then evaluate 1 time in HF model per iteration. For the SAO approach, neural network was used to establish the surrogate model, each relocated sub-region was sampled 15 times per iteration. For the ARC approach, it is discovered the initial LF

model need to be sampled 200 times to establish a reliable ANN surrogate model, and in each iteration of it, both LF and HF model need to be evaluated 5 times. The estimation error over iteration steps for all three methods were plotted in Figure 48, which shows that all three algorithms reached the point exactly as or close to the analytical optimal point. Although the SAMO converged slower which took 7 steps, with the overall experimental and simulation cost considered, SAMO only costs \$465, while SAO and ARC cost \$2722 and \$1376, respectively.

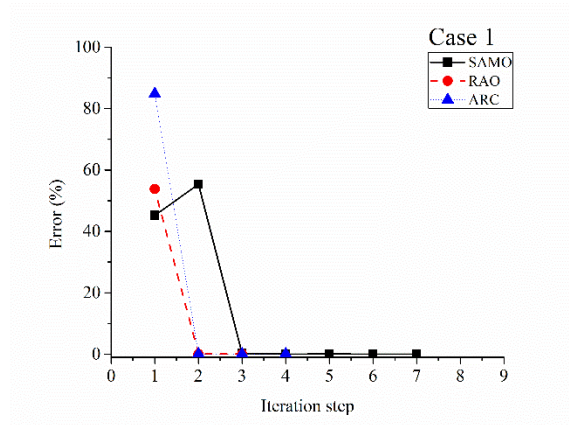


Figure 48 Comparison of optimization error of SAMO, RAO, and ARC algorithms for case #1

6.1.2. Case study 2—Gramacy & Lee function

Gramacy & Lee function [128] is a semi-periodic function with multiple local optimum (see Figure 49) by incorporated Sine function. It has the form of

$$\begin{aligned} \text{Minimize } y(x) &= \frac{\sin(10\pi z(x))}{2z(x)} + (z(x)-1)^4 \\ \text{where } z(x) &= x/500 + 0.5 \\ \text{subject to } 0 &\leq x \leq 1000, \text{ where } x \text{ is an integer} \end{aligned} \quad (6.2)$$

and the optimum solution is -0.8683 when $x = 24$.

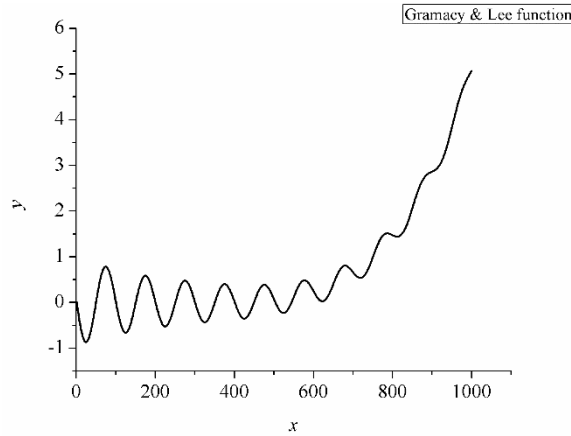
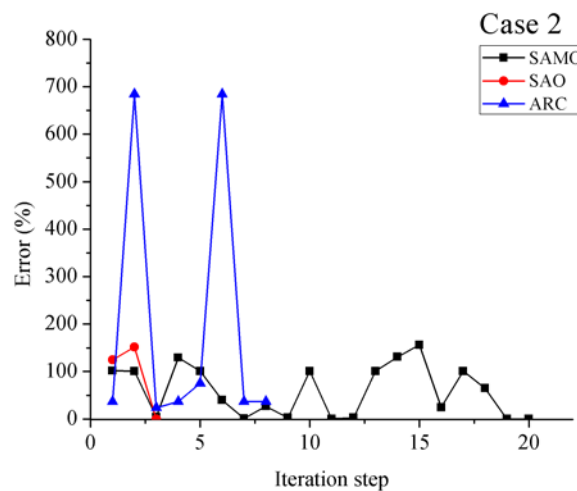


Figure 49 Gramacy & Lee function

The SAMO, SAO, and ARC algorithms were applied, and their performances were compared. For the SAMO approach, same as Case #1, the design space was initially

sampled 50 times and evaluated in LF model and then evaluate 1 time in HF model per iteration. For the SAO approach, it is discovered that each relocated sub-region need to be sampled 25 times per iteration to ensure converge to the analytical optimum solution. For the ARC approach, it is discovered it converges to a local minimum instead of global minimum corresponded to $x=134$ with the previous setting. And further increase the sampling rate does not solve this issue. Figure 50 shows the estimation error over iteration steps for all three methods. It is demonstrated that both SAO and SAMO could converge to the global minimum while ARC failed. Moreover, the overall costs of all three methods are calculated. SAMO is still cost-effective with a value of \$1251.5 and optimization with SAO and ARC cost \$4537.5 and \$2586.



**Figure 50 Comparison of optimization error of SAMO, RAO, and ARC algorithms
for case #2**

6.1.3. Case study 3—Six-Hump Camel function

Six-Hump Camel function [129] is a two-dimensional optimization test function which has six local minima, two of which are global in the entire region. And in the evaluated region, as shown in Figure 51, has 4 minima where two of them are global.

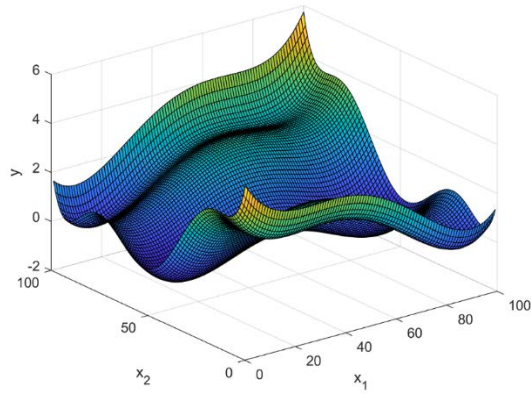
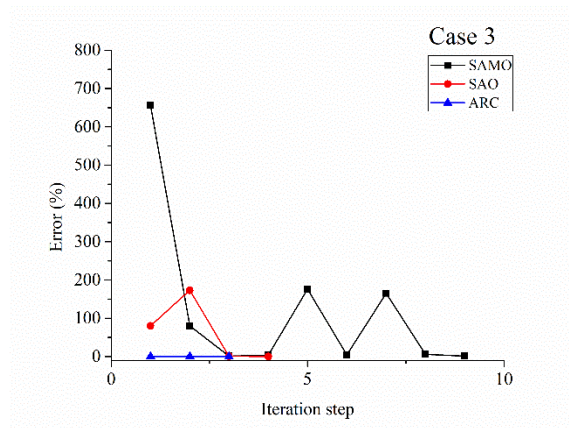


Figure 51 Six-Hump Camel function

The objective function of this problem is

$$\begin{aligned}
 \text{Minimize } y(x_1, x_2) &= (4 - 2.1p(x_1)^2 + \frac{p(x_1)^4}{3})p(x_1)^2 \\
 &\quad + p(x_1)q(x_2) + (-4 + 4q(x_2)^2)q(x_2)^2 \\
 \text{where } p(x_1) &= x_1 / 25 - 2 \\
 q(x_2) &= x_2 / 50 - 1 \\
 \text{subject to } 0 &\leq x_1 \leq 100, \text{ where } x_1 \text{ is an integer} \\
 0 &\leq x_2 \leq 100, \text{ where } x_2 \text{ is an integer}
 \end{aligned} \tag{6.3}$$

The global minimum of y is -1.0307 at (52.14) and (48,86) . A comparison was made between the performances of SAMO, SAO, and ARC. The setting of each algorithm can be described as follows: for SAMO, the design space was initially sampled 10 times on each dimension with evaluation performed in LF model and then evaluate 1 time in HF model per iteration; with regard of SAO, 25 experiments were performed for each iteration; while in ARC algorithm, the parameter space need to be sampled at least 25 times on each dimension to ensure convergence, and 25 experiments were needed for each iteration. Figure 52 demonstrated how the estimation error varied with iteration steps for each algorithm. It can be seen that although SAMO converged slower, but in each step of it, only one experiment run is needed which saved the experimental cost. With the calculation of overall cost performed, for case #3, SAMO only cost \$627.5, while optimize with SAO and ARC need \$6050 and \$5056.25, respectively.



**Figure 52 Comparison of optimization error of SAMO, RAO, and ARC algorithms
for case #3**

6.1.4. Case study 4—optimize tensile strength of FDM manufactured part

As reviewed before, Rayegani and Onwubolu [56] studied how part orientation, raster angle, raster width, and air gap affect the tensile strength of FDM manufactured ABS parts. The model they established can be formed as

$$\begin{aligned}
 &\text{Maximize } y = 33.8477 + 0 \cdot x_1 + 0 \cdot x_2 - 1.6447x_3 - 45.5050x_4 \\
 &\quad - 0.0011 x_1x_2 + 0.0206 x_1x_3 + 0.2293 x_1x_4 \\
 &\quad - 0.0671 x_2x_3 - 0.0732 x_2x_4 + 33.1809 x_3x_4 \\
 &\quad - 0.0013x_1^2 + 0.0020x_2^2 - 4.6791x_3^2 - 23.8441x_4^2 \\
 &\text{where } x_1 = a / 9 \cdot (90 - 0) + 0 \\
 &\quad x_2 = b / 9 \cdot (50 - 0) + 0 \\
 &\quad x_3 = c / 9 \cdot (0.5588 - 0.2034) + 0.2034 \\
 &\quad x_4 = c / 9 \cdot (0.5588 + 0.2055) - 0.2055 \\
 &\text{subject to } 0 \leq a \leq 9, \text{ where } a \text{ is an integer} \\
 &\quad 0 \leq b \leq 9, \text{ where } b \text{ is an integer} \\
 &\quad 0 \leq c \leq 9, \text{ where } c \text{ is an integer} \\
 &\quad 0 \leq d \leq 9, \text{ where } d \text{ is an integer}
 \end{aligned} \tag{6.4}$$

SAMO was used to optimize this process with the help of LF model. The surrogate model was established with sample each dimension three times and loop through all possible combinations. For each iteration, HF model was evaluated once, with 4 iterations in total. Table 15 presented the parameter combination to attempt after each iteration and the corresponded response. It can be seen that although in the end, the SAMO did not reach the exact solution with an error of 3.38% but compared with the original 20 experimental runs to establish such an analytical model, use of the RAMO reduced the overall costs from \$1210 to \$309.23.

Table 15 Details of the SAMO attempted experimental runs and the corresponded response in Case 5

Iteration step	a	b	c	d	Predicted Response	Error
1	1	7	9	0	32.64	11.44
2	0	9	9	0	34.25	7.07
3	0	9	0	0	36.86	0.00
4 (final)	2	9	0	0	35.61	3.38

6.1.5. Case study 5—optimize strength and volumetric shrinkage of FDM manufactured part

In this subsection, multi-objective optimization was performed with the SAMO. The optimization problem can be formulated based on Gurralla and Regalla's study [92], which studies how infill density, horizontal orientation, vertical orientation affect the tensile strength and volumetric shrinkage of the FDM manufactured parts.

$$\begin{aligned}
 &\text{Maximize } f(A, B, C) = w_1 \cdot \text{ST} - w_2 \cdot \text{VS} \\
 &\text{where } \text{St} = 17.51 + 7.19A + 0.73B - 0.37C - 0.032AB \\
 &\quad \quad \quad + 0.25AC + 1.41BC + 2.5A^2 - 5.86B^2 + 8.56C^2 \\
 &\quad \quad \quad \text{VS} = 4.26 + 0.0076A + 0.76B - 0.49C + 0.42AB \\
 &\quad \quad \quad - 0.66AC + 1.94BC - 0.29A^2 - 1.19B^2 + 2.64C^2 \\
 &\quad \quad \quad A = (22.72 - 14.43) / 9 \cdot a + 14.43 \\
 &\quad \quad \quad B = (45 - 0) / 9 \cdot b + 0 \\
 &\quad \quad \quad C = (90 - 0) / 9 \cdot c + 0 \\
 &\text{subject to } 0 \leq a \leq 9, \text{ where } a \text{ is an integer} \\
 &\quad \quad \quad 0 \leq b \leq 9, \text{ where } b \text{ is an integer} \\
 &\quad \quad \quad 0 \leq c \leq 9, \text{ where } c \text{ is an integer}
 \end{aligned} \tag{6.5}$$

The values of w_1 and w_2 were picked based on user's preference and subject to normalization. Considering the maximum value of ST and VS is 35.8868 and 7.9652,

respectively, and assume user prefer stronger parts over dimensional accuracy, w_1 is selected as 0.019 and w_2 is set as 0.037. With 3 sampling on each dimension initially, SAMO was used to optimize the manufacturing process. Table 16 listed the manufacturing condition SAMO recommended to attempt before convergence, showed SAMO reached convergence after only 5 runs. And the results is in close match with Rao and Rai's study [26]. Compared with 20 experimental runs in the initial literature, the SAMO could reduce the optimization cost from \$1210 to \$325.

Table 16 Details of the SAMO attempted experimental runs and the corresponded response in Case 6

Iteration step	a	b	c	Predicted strength	Predicted volumetric shrinkage
1	9	5	9	35.80	5.80
2	9	3	9	34.29	4.30
3	9	4	7	29.54	3.89
4	9	0	9	27.67	1.16
5 (Final)	9	0	8	24.63	0.80
Ref [26]	9	0	8.876	24.60	0.80

6.1.6. Case study 6—optimize the modulus of elasticity over building time of FDM manufactured part

With the help of constructed meso-structure model introduced in Chapter 5, an attempt was made to optimize the modulus of elasticity over building time of FDM manufactured part. In this case, the objective function would be unknown, and the problem is formed as

$$\begin{aligned}
& \text{maximize} \quad y(x_1, x_2) = \frac{\text{the modulus of elasticity}}{\text{building time}} \\
& \text{subject to} \quad 1 \leq x_1 \leq 20, \text{ where } x_1 \text{ is an integer} \\
& \quad \quad \quad 1 \leq x_2 \leq 3, \text{ where } x_2 \text{ is an integer}
\end{aligned} \tag{6.6}$$

where x_1 is infill density divided by 5 and x_2 is one of three infill patterns investigated (rectilinear, triangular, and honeycomb). LF model to predict the modulus of elastic is introduced in detail in Chapter 5 while LF model to predict the building time was based on a ANN model trained on actual measured time. The setting of LF model used to construct the initial surrogate model was listed in Table 17, which consists of 18 different manufacturing conditions derived from the numerical simulation model.

With the LF surrogate model available, SAMO started to suggest experimental run conditions. And after each part manufacturing and optimization process, SAMO took the input of the previous experimental results and suggested the next run to attempt. Those suggested process parameters were also shown in Table 17, it is seen that the algorithm converged with only 3 steps at the infill pattern of 100% triangular. Several other conditions have also been tested and their results were used to check whether the obtained condition is indeed optimum or how close to the true optima. The results were summarized in Table 18, demonstrated that the error of the SAMO obtained solution lied into the optimal state.

Table 17 LF model results used to establish the surrogate model and the SAMO**suggested HF model results**

No.	Printing pattern	x_1	x_2	Predicted modulus of elasticity (MPa)	Predicted building time (min)	y
LF model evaluation results						
1	10% Rectilinear	2	1	95.57	8	11.95
2	10% Honeycomb	2	2	114.07	8	14.26
3	10% Triangular	2	3	215.66	9	23.96
4	20% Rectilinear	4	1	154.04	9	17.12
5	20% Honeycomb	4	2	206.20	9	22.91
6	20% Triangular	4	3	329.82	10	32.98
7	35% Rectilinear	7	1	123.67	11	11.24
8	35% Honeycomb	7	2	161.13	12	13.43
9	35% Triangular	7	3	546.59	11	49.69
10	50% Rectilinear	10	1	160.57	12	13.38
11	50% Honeycomb	10	2	215.34	14	15.38
12	50% Triangular	10	3	587.63	12	48.97
13	65% Rectilinear	13	1	147.62	14	10.54
14	65% Honeycomb	13	2	212.42	16	13.28
15	65% Triangular	13	3	698.42	14	49.89
16	80% Rectilinear	16	1	162.16	15	10.81
17	80% Honeycomb	16	2	218.48	18	12.14
18	80% Triangular	16	3	762.67	16	47.67
HF model evaluation results						
1	45% Triangular	9	3	625.16	12.41	50.38
2	100% Triangular	20	3	1009.97	18.50	54.59
3	100% Triangular	20	3	Algorithm converged!		

Table 18 Results of samples manufactured in the vicinity of the obtained solution

No.	Printing pattern	x_1	x_2	Predicted modulus	Predicted building	y
1	40% Triangular	8	3	572.2 ± 9.7	11.83 ± 0.07	48.37 ± 0.87
2	50% Triangular	10	3	534.0 ± 11.4	12.42 ± 0.09	43.00 ± 0.97
3	55% Triangular	11	3	649.3 ± 9.2	13 ± 0.09	49.95 ± 0.79
4	60% Triangular	12	3	697.6 ± 11.9	13.83 ± 0.13	50.44 ± 0.98
5	65% Triangular	13	3	690.9 ± 7.9	14.42 ± 0.09	47.91 ± 0.62
6	80% Triangular	16	3	699.0 ± 9.8	15.67 ± 0.07	44.61 ± 1.02
7	95% Triangular	19	3	895.0 ± 18.2	18.03 ± 0.12	49.64 ± 1.05

6.2. Discussions

The effect of sampling strategy and low-fidelity model accuracy on the convergence rate of the SAMO was analyzed based on a variation of case #5

$$\begin{aligned}
 &\text{Maximize } f(A, B, C) = 17.51 + 7.19A + 0.73B - 0.37C - 0.032AB \\
 &\quad + 0.25AC + 1.41BC + 2.5A^2 - 5.86B^2 + 8.56C^2 \\
 &\text{where } A = (22.72 - 14.43) / 9 \cdot a + 14.43 \\
 &\quad B = (45 - 0) / 9 \cdot b + 0 \\
 &\quad C = (90 - 0) / 9 \cdot c + 0 \\
 &\text{subject to } 0 \leq a \leq 9, \text{ where } a \text{ is an integer} \\
 &\quad 0 \leq b \leq 9, \text{ where } b \text{ is an integer} \\
 &\quad 0 \leq c \leq 9, \text{ where } c \text{ is an integer}
 \end{aligned} \tag{6.7}$$

In case #5, the uniform grid sampling strategy was adopted where parameters a, b, c were sampled 3 times on each dimension with the equal distance (i.e. level 2, 4, and 7), composed 27 LF data. However, one may wonder would change the sampling strategy to random sampling or increase the grid interval has a huge impact on the convergence rate of the algorithm developed? Table 19 listed the results after the investigation. it appears that increase grid interval lead to the increment of estimation error, but the

convergence rate did not necessarily slow down. Alternatively, if the sampling strategy was changed from uniform grid interval to random sampling, the estimation error clearly increased, and with more data were used to construct the surrogate model, the optimizer converged faster.

Table 19 The convergence data for different sampling strategy

Total samples	Grid interval	Steps that the SAMO converges	Converged at level	Error (%)
125	2	12	(9,5,9)	0
64	3	3	(9,6,9)	0.30
27	3	12	(9,5,9)	0
27	4	3	(9,4,0)	0.2370
8	4	13	(9,3,0)	0.9376
8	5	8	(9,3,1)	10.74
8	Random	19	(9,3,0)	0.9376
27	Random	12	(9,6,9)	0.30
64	Random	6	(9,4,0)	0.3070
125	Random	3	(9,4,0)	0.3070

For case study #1 to #5, the LF model was established with adding random noise to the original analytical model with a perturbation amplitude of 10%. It is intuitive to assume that if the perturbation amplitude was increased to create a less accurate numerical model, the convergence rate would decay and may not be able to converge to the global optimum. With the practical additive manufacturing cases such as Eq.6.7, the perturbation amplitude was gradually increased from 5% to 30%, and the results was recorded. To ensure a fair comparison, the uniform grid sampling strategy was adopted with three levels in each dimension, and the results were listed in Table 20.

Table 20 The convergence data for low-fidelity model accuracy

Perturbation amplitude (%)	Steps that the SAMO converges	Converged at level	Error (%)
5	11	969	0.30
10	12	959	0
15	7	959	0
20	6	959	0
25	11	949	1.30
30	6	969	0.30

From Table 20, it is seen that contradicted to the previous presumption, SAMO had a very good noise tolerance ability. The major reason is ANN has the characteristics of extensive parallel interconnections and distributed information storage, make it ideal to be used to construct a surrogate model with good noise tolerance ability. Moreover, for practical AM problems, the response surface of input-output data seldom contains local optimum, so that the optimizer is more likely to converge even with noise-added data.

As the subsets were divided and weights were initialized randomly in the training stage of ANN models, although the random seed was fixed in the previous study, additional tests were performed to investigate the effect of randomness in the performance of SAMO. A total of 100 test runs were conducted with uniform grid sampling strategy (4 samples on each dimension) and the resulted estimation error and required steps to converge were plotted in Figure 53.

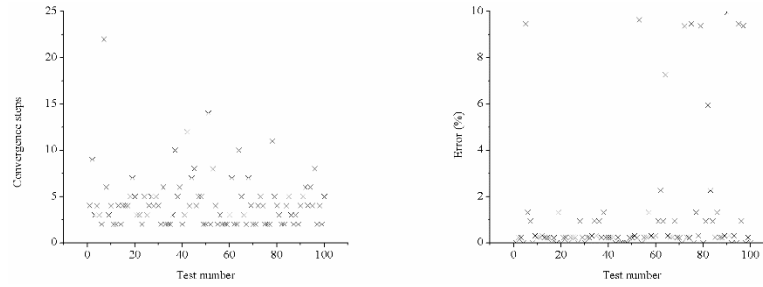


Figure 53 Plots of convergence steps and estimation error in 100 runs with random initialization process

Based on Figure 53, most of the test runs showed a good performance, a majority of them had the estimation error less than 2% and could converge in less than 10 steps.

It should be noted that one assumption made in this section was the input variables/parameters were independent from each other. If covariance or correlation exists between the input parameters, then the change of one parameter might influence how the system would respond to another parameter. Hence it is essential to perform an independence test prior to such an optimization process described in this section.

6.3. Summary

In this section, the developed optimizer, SAMO, was tested on different theoretical and practical optimization problems. Compared with traditional optimization algorithm such as SAO and ARC, the SAMO is less likely to converge to a local optimum and tends to be more accurate. Moreover, given the consideration of overall experimental and

simulation cost to support the optimization process, SAMO showed exceptional cost-effective characteristic. The results presented in this work showed SAMO could reduce the cost by at least 72.4% when compared with experimental-only method, and costs less than half of the fellow surrogate-based method.

The robustness of SAMO was tested with response surface functions provided by previous researchers. It showed a very good noise tolerance ability when the low-fidelity model was added with increasing noise. Furthermore, the random neural network initialization process was discovered to have a small effect on the optimizer performance—a majority of 100 test runs showed an acceptable performance.

7. SUMMARY, CONCLUSIONS, AND FUTURE DIRECTIONS

7.1. Summary

Due to affordability and feasibility, Fused Deposition Modeling (FDM) has become one of the most popular Additive Manufacturing (AM) processes worldwide since the early 2000s. However, low dimensional accuracy and inconsistent mechanical properties of the FDM products hinder the future growth of FDM technology considerably. The literature review revealed that multiple methods have been used to model, predict, and optimize the thermal and mechanical behavior of the FDM process and products. However, relying solely on experimental or numerical models is too expensive or provides only low-accuracy predictive results. Therefore, the focus of this dissertation is to develop a hybrid experimental/numerical model to analyze, predict and optimize the thermal and mechanical behavior of the FDM process and FDM manufactured products.

For the investigation of thermal behavior, the effects of nozzle temperature, platform temperature, extrusion speed, and layer thickness on effective diffusion time were first evaluated using on the experimental model. A numerical simulation model was then established using information provided by the experimental model and validated using the experimental results. In particular, the boundary condition during the manufacturing process was obtained through solving an inverse heat transfer problem with the help of machine learning method. Therefore, a predictive model can be established to predict the

maximum vertical distortion, and maximum thermal stress during and after the manufacturing process with varying process parameters.

For the investigation of mechanical behavior, the effects of printing pattern and infill density on ultimate tensile strength-weight ratio and the modulus of elasticity were evaluated using unidirectional and bidirectional samples. The stress-strain curves of FDM products were measured by tensile testing experiments, providing the outcomes of the experimental model. Similar to the investigation of thermal behavior, a numerical simulation model was established with information provided by the experimental model and validated using the experimental results. However, the approach adopted in this study required only very limited information from the experimental model, which is the structure of the tested sample. With the help of neural networks, a knowledge-based library was constructed to predict the tensile behavior of samples with any infill geometry.

For the investigation of optimization approach, a surrogate-based additive manufacturing optimizer (SAMO) was established to expedite the optimization process to maximize or minimize certain products' characteristics. The overall objective of SAMO is to reduce the number of experiments that need to be performed on additive manufacturing machines, and thereby make the optimization process more efficient. SAMO is developed to guide the optimization decision-making process by combining cost-effective but less accurate predictive models with expensive but accurate experimental

models. The SAMO iteratively obtains the current manufacturing condition and the corresponded response and determines the next manufacturing condition to attempt. The developed optimizer was tested on different theoretical and practical optimization problems, and the results were compared with traditional optimization algorithms. In summary, this research provided the additive manufacturing industry with the knowledge to control, improve, and optimize the manufacturing process.

7.2. Conclusions

The numerical and experimental models in this study both revealed that polylactic acid (PLA) has the longest diffusion time at high nozzle temperature, high platform temperature, low printing speed, and thick layer. For the same geometric model and printing parameters, the simulation model predicted the effective diffusion time with a bias less than 13% in six out of nine conditions, which was relatively lower than the existing simulation and theoretical prediction models in the literature. The developed numerical model revealed that reducing extrusion temperature, slowing printing speed, and decreasing layer thickness could help reduce vertical distortion and residual thermal stress, while a high platform temperature might have the opposite effect on deformation and residual stress.

The experimental results from mechanical behavior analysis revealed that minimizing the air gap, and using a triangular infill pattern are beneficial to UTS/weight ratio. Of all the specimens considered, the 20% triangular pattern has the highest UTS/weight ratio.

In the numerical investigation, the meso-structure approach does not require input from the unidirectional specimen stress-strain curves, and it can be used to predict the modulus of elasticity and product breakage location in most cases.

Using the same hybrid-model approach, SAMO was demonstrated to be superior to traditional optimization algorithms in the area of additive manufacturing applications. SAMO is less likely to converge to a local optimum and tends to be more accurate. Moreover, when considering the overall experimental and simulation cost to support the optimization process, SAMO was found to be exceptionally effective. The results presented in this work showed SAMO could reduce cost by at least 72.4% when compared with experimental-only method, and costs less than half of the fellow surrogate-based method. The robustness of SAMO was tested with response surface functions provided by previous researchers. It showed a very good noise tolerance ability when the low-fidelity model was added with increasing noise.

7.3. Future directions

For an FDM process using polymer materials, two non-included phenomena could potentially affect the accuracy of a numerical prediction thermal and mechanical model; structural relaxation and the wetting/bonding process. For example, through analyzing SEM images of the manufactured product, a geometric coefficient can be introduced to correlate the inter-layer bonding. However, the correlation between printing parameters

and function coefficient still requires extensive experimental and theoretical investigation.

Second, beyond increasing the accuracy of the proposed model, future directions of this work could include investigation of failure mechanism [142], compression behavior [143], and buckling behavior [144] of additive manufactured thermoplastic polymer parts with the help of finite element analysis.

Third, future development of the optimizer could include identification of pareto front for multi-objective optimization problems. Although the current model could possibly be used for this purpose, the high-fidelity model evaluation times were extremely high, which would increase the overall cost. Fitting a generic algorithm into the surrogate-model building process could potentially ease the cost.

Last is the computation time of the optimizer could be enhanced. To acquire the optimum value through a neural network model, the current approach is very straightforward—loop through all possible combinations of the input parameters. However, when the network size became large or input dimensions increased to over 10, the computation cost was heavy. Advanced techniques that take the consideration of both computation time and the accuracy of the results into consideration could be developed.

REFERENCES

1. Weng, Z., et al., Mechanical and thermal properties of ABS/montmorillonite nanocomposites for fused deposition modeling 3D printing. *Materials & Design*, 2016. **102**: p. 276-283.
2. Crump, S.S., Apparatus and method for creating three-dimensional objects. 1992, Google Patents.
3. Kruth, J.-P., Material increment manufacturing by rapid prototyping techniques. *CIRP Annals-Manufacturing Technology*, 1991. **40**(2): p. 603-614.
4. Wohlers, T.T., Wohlers report 2004: rapid prototyping, tooling and manufacturing state of the industry : annual worldwide progress report. 2004: Wohlers Associates.
5. Wohlers, T.T., Wohlers Report 2015: Additive Manufacturing and 3D Printing State of the Industry : Annual Worldwide Progress Report. 2015, Fort Collins, Colorado, USA: Wohlers Associates.
6. Hollister, S.J., Porous scaffold design for tissue engineering. *Nature materials*, 2005. **4**(7): p. 518-524.
7. Melchels, F.P., et al., Additive manufacturing of tissues and organs. *Progress in Polymer Science*, 2012. **37**(8): p. 1079-1104.

8. McGurk, M., et al., Rapid prototyping techniques for anatomical modelling in medicine. *Annals of the Royal College of Surgeons of England*, 1997. **79**(3): p. 169.
9. Azari, A. and S. Nikzad, The evolution of rapid prototyping in dentistry: a review. *Rapid Prototyping Journal*, 2009. **15**(3): p. 216-225.
10. McCullough, E.J. and V.K. Yadavalli, Surface modification of fused deposition modeling ABS to enable rapid prototyping of biomedical microdevices. *Journal of Materials Processing Technology*, 2013. **213**(6): p. 947-954.
11. Poole, S. and R. Phillips. Rapid prototyping of small wind turbine blades using additive manufacturing. in *Pattern Recognition Association of South Africa and Robotics and Mechatronics International Conference (PRASA-RobMech)*, 2015. 2015. IEEE.
12. Guerrero-Villar, F., et al., Development of Vertical Wind Turbines via FDM Prototypes. *Procedia Engineering*, 2015. **132**: p. 78-85.
13. Fernández, S., et al., Additive Manufacturing and Performance of Functional Hydraulic Pump Impellers in Fused Deposition Modeling Technology. *Journal of Mechanical Design*, 2016. **138**(2): p. 024501.
14. Aviation, G. GE Aviation Signs Additive Manufacturing Cooperative Agreement with Sigma Labs. 2013 [cited 2016 Sept. 6].

15. Ziemian, C., M. Sharma, and S. Ziemian, Anisotropic mechanical properties of ABS parts fabricated by fused deposition modelling. 2012: INTECH Open Access Publisher.
16. Carneiro, O., A. Silva, and R. Gomes, Fused deposition modeling with polypropylene. *Materials & Design*, 2015. **83**: p. 768-776.
17. Wang, T.-M., J.-T. Xi, and Y. Jin, A model research for prototype warp deformation in the FDM process. *The International Journal of Advanced Manufacturing Technology*, 2007. **33**(11): p. 1087-1096.
18. Huang, Q., et al., Optimal offline compensation of shape shrinkage for three-dimensional printing processes. *IIE Transactions*, 2015. **47**(5): p. 431-441.
19. Peng, A. and X. Xiao, Investigation on reasons inducing error and measures improving accuracy in fused deposition modeling. *Advances in Information Sciences and Service Sciences*, 2012. **4**(5).
20. Turner, B.N., R. Strong, and S.A. Gold, A review of melt extrusion additive manufacturing processes: I. Process design and modeling. *Rapid Prototyping Journal*, 2014. **20**(3): p. 192-204.
21. Bikas, H., P. Stavropoulos, and G. Chryssolouris, Additive manufacturing methods and modelling approaches: a critical review. *The International Journal of Advanced Manufacturing Technology*, 2016. **83**(1-4): p. 389-405.

22. Weiss, B., D.W. Storti, and M.A. Ganter, Low-cost closed-loop control of a 3D printer gantry. *Rapid Prototyping Journal*, 2015. **21**(5): p. 482-490.
23. Fang, T., et al. Online defect detection in layered manufacturing using process signature. in *Systems, Man, and Cybernetics*, 1998. 1998 IEEE International Conference on. 1998. San Diego, California, USA: IEEE.
24. Sun, Q., et al., Effect of processing conditions on the bonding quality of FDM polymer filaments. *Rapid Prototyping Journal*, 2008. **14**(2): p. 72-80.
25. Wu, H., Y. Wang, and Z. Yu, In situ monitoring of FDM machine condition via acoustic emission. *The International Journal of Advanced Manufacturing Technology*, 2016. **84**(5-8): p. 1483-1495.
26. Rao, R.V. and D.P. Rai, Optimization of fused deposition modeling process using teaching-learning-based optimization algorithm. *Engineering Science and Technology, an International Journal*, 2016. **19**(1): p. 587-603.
27. Rodriguez, J.F., J.P. Thomas, and J.E. Renaud, Characterization of the mesostructure of fused-deposition acrylonitrile-butadiene-styrene materials. *Rapid Prototyping Journal*, 2000. **6**(3): p. 175-186.
28. Thomas, J. and J. Rodríguez. Modeling the fracture strength between fused deposition extruded roads. in *Proceedings of the 11th Solid Freeform Fabrication Symposium*. 2000.

29. Atif Yardimci, M. and S. Güçeri, Conceptual framework for the thermal process modelling of fused deposition. *Rapid Prototyping Journal*, 1996. **2**(2): p. 26-31.
30. Li, L., et al., Modeling of bond formation in FDM process, in the 31st North American Manufacturing Research Conference. 2003: Hamilton, Ontario, Canada.
31. Bellehumeur, C., et al., Modeling of bond formation between polymer filaments in the fused deposition modeling process. *Journal of Manufacturing Processes*, 2004. **6**(2): p. 170-178.
32. Costa, S., F. Duarte, and J. Covas, Towards modelling of Free Form Extrusion: analytical solution of transient heat transfer. *International Journal of Material Forming*, 2008. **1**: p. 703-706.
33. Zhang, Y., Three-dimensional Finite Element Analysis of Residual Stresses and Part Distortions in Fused Deposition Modeling Process. 2006, University of Alabama, Tuscaloosa, Alabama, USA.
34. Zhang, Y. and K. Chou, A parametric study of part distortions in fused deposition modelling using three-dimensional finite element analysis. *Proceedings of the Institution of Mechanical Engineers, Part B: Journal of Engineering Manufacture*, 2008. **222**(8): p. 959-968.

35. Wang, H., et al., Non-metallic coating thickness prediction using artificial neural network and support vector machine with time resolved thermography. *Infrared Physics & Technology*, 2016. **77**: p. 316-324.
36. Ji, L.B. and T.R. Zhou. Finite element simulation of temperature field in fused deposition modeling. in *Advanced Materials Research*. 2010. Trans Tech Publ.
37. Zhang, J., et al., Numerical investigation of the influence of process conditions on the temperature variation in fused deposition modeling. *Materials & Design*, 2017. **130**: p. 59-68.
38. Costa, S., F. Duarte, and J. Covas, Thermal conditions affecting heat transfer in FDM/FFE: a contribution towards the numerical modelling of the process: This paper investigates convection, conduction and radiation phenomena in the filament deposition process. *Virtual and Physical Prototyping*, 2015. **10**(1): p. 35-46.
39. Dabiri, S., S. Schmid, and G. Tryggvason. Fully Resolved Numerical Simulations of Fused Deposition Modeling. in *ASME 2014 International Manufacturing Science and Engineering Conference collocated with the JSME 2014 International Conference on Materials and Processing and the 42nd North American Manufacturing Research Conference*. 2014. Detroit, Michigan, USA: American Society of Mechanical Engineers.

40. Kousiatza, C., N. Chatzidai, and D. Karalekas, Temperature Mapping of 3D Printed Polymer Plates: Experimental and Numerical Study. *Sensors*, 2017. **17**(3): p. 456.
41. Monzón, M.D., et al., Process and material behavior modeling for a new design of micro-additive fused deposition. *The International Journal of Advanced Manufacturing Technology*, 2013. **67**(9-12): p. 2717-2726.
42. Zhou, X., et al., Cycle life estimation of lithium-ion polymer batteries using artificial neural network and support vector machine with time-resolved thermography. *Microelectronics Reliability*, 2017. **79**: p. 48-58.
43. Maldague, X.P., *Nondestructive evaluation of materials by infrared thermography*. 2012: Springer Science & Business Media.
44. Vollmer, M. and M. Klaus-Peter, *Infrared thermal imaging: fundamentals, research and applications*. 2010: John Wiley & Sons.
45. Usamentiaga, R., et al., Infrared thermography for temperature measurement and non-destructive testing. *Sensors*, 2014. **14**(7): p. 12305-12348.
46. Dinwiddie, R.B., L.J. Love, and J.C. Rowe, Real-time process monitoring and temperature mapping of a 3D polymer printing process. *SPIE defense, security, and sensing*, International Society for Optics and Photonics, 2013: p. 87050L.

47. Dinwiddie, R.B., et al. Infrared imaging of the polymer 3D-printing process. in SPIE Sensing Technology+ Applications. 2014. Baltimore, Maryland, USA International Society for Optics and Photonics.
48. Seppala, J.E. and K.D. Migler, Infrared thermography of welding zones produced by polymer extrusion additive manufacturing. Additive Manufacturing, 2016. **12**: p. 71-76.
49. Compton, B.G., et al., Thermal analysis of additive manufacturing of large-scale thermoplastic polymer composites. Additive Manufacturing, 2017.
50. Mani, M., et al., Measurement science needs for real-time control of additive manufacturing powder bed fusion processes. National Institute of Standards and Technology, Gaithersburg, MD, Standard No. NISTIR, 2015. **8036**.
51. Fang, T., Online image processing and defect detection in layered manufacturing using process signature. 2000.
52. Baumann, F. and D. Roller. Vision based error detection for 3D printing processes. in MATEC web of conferences. 2016. EDP Sciences.
53. Cheng, Y. and M.A. Jafari, Vision-based online process control in manufacturing applications. IEEE Transactions on Automation Science and Engineering, 2008. **5**(1): p. 140-153.

54. Kantaros, A. and D. Karalekas, Fiber Bragg grating based investigation of residual strains in ABS parts fabricated by fused deposition modeling process. *Materials & Design*, 2013. **50**: p. 44-50.
55. Rao, P.K., et al., Online real-time quality monitoring in additive manufacturing processes using heterogeneous sensors. *Journal of Manufacturing Science and Engineering*, 2015. **137**(6): p. 061007.
56. Rayegani, F. and G. Onwubolu, Fused deposition modelling (FDM) process parameter prediction and optimization using group method for data handling (GMDH) and differential evolution (DE). *International Journal of Advanced Manufacturing Technology*, 2014. **73**.
57. Mohamed, O.A., S.H. Masood, and J.L. Bhowmik, Optimization of fused deposition modeling process parameters: a review of current research and future prospects. *Advances in Manufacturing*, 2015. **3**(1): p. 42-53.
58. Chung Wang, C., T.-W. Lin, and S.-S. Hu, Optimizing the rapid prototyping process by integrating the Taguchi method with the Gray relational analysis. *Rapid prototyping journal*, 2007. **13**(5): p. 304-315.
59. Sood, A.K., R. Ohdar, and S.S. Mahapatra, Improving dimensional accuracy of fused deposition modelling processed part using grey Taguchi method. *Materials & Design*, 2009. **30**(10): p. 4243-4252.

60. Sahu, R.K., S. Mahapatra, and A.K. Sood, A study on dimensional accuracy of fused deposition modeling (FDM) processed parts using fuzzy logic. *Journal for Manufacturing Science & Production*, 2013. **13**(3): p. 183-197.
61. Xinhua, L., et al., An investigation on distortion of PLA thin-plate part in the FDM process. *The International Journal of Advanced Manufacturing Technology*, 2015. **79**(5-8): p. 1117-1126.
62. Mohamed, O.A., S.H. Masood, and J.L. Bhowmik, Optimization of fused deposition modeling process parameters for dimensional accuracy using I-optimality criterion. *Measurement*, 2016. **81**: p. 174-196.
63. Nancharaiah, T., D.R. Raju, and V.R. Raju, An experimental investigation on surface quality and dimensional accuracy of FDM components. *International Journal on Emerging Technologies*, 2010. **1**(2): p. 106-111.
64. Zhang, J.W. and A.H. Peng. Process-parameter optimization for fused deposition modeling based on Taguchi method. in *Advanced Materials Research*. 2012. Trans Tech Publ.
65. Peng, A., X. Xiao, and R. Yue, Process parameter optimization for fused deposition modeling using response surface methodology combined with fuzzy inference system. *The International Journal of Advanced Manufacturing Technology*, 2014. **73**(1-4): p. 87-100.

66. Zhou, X., S.-J. Hsieh, and C.-C. Ting, Modelling and estimation of tensile behaviour of polylactic acid parts manufactured by fused deposition modelling using finite element analysis and knowledge-based library. *Virtual and Physical Prototyping*, 2018. **13**(2): p. 1-14.
67. Es-Said, O., et al., Effect of layer orientation on mechanical properties of rapid prototyped samples. *Materials and Manufacturing Processes*, 2000. **15**(1): p. 107-122.
68. Durgun, I. and R. Ertan, Experimental investigation of FDM process for improvement of mechanical properties and production cost. *Rapid Prototyping Journal*, 2014. **20**(3): p. 228-235.
69. Cantrell, J., et al., Experimental Characterization of the Mechanical Properties of 3D Printed ABS and Polycarbonate Parts, in *Advancement of Optical Methods in Experimental Mechanics*, Volume 3. 2017, Springer. p. 89-105.
70. Zhang, Y., M.S. Mamadapur, and J. Wang, Constitutive modelling for fused deposition modelling of acrylonitrile butadiene styrene (ABS) under elastic response. *International Journal of Rapid Manufacturing*, 2015. **5**(1): p. 76-94.
71. Ahn, S.-H., et al., Anisotropic material properties of fused deposition modeling ABS. *Rapid Prototyping Journal*, 2002. **8**(4): p. 248-257.

72. Sood, A.K., R. Ohdar, and S. Mahapatra, Parametric appraisal of mechanical property of fused deposition modelling processed parts. *Materials & Design*, 2010. **31**(1): p. 287-295.
73. Masood, S.H., K. Mau, and W. Song. Tensile properties of processed FDM polycarbonate material. in *Materials Science Forum*. 2010. Trans Tech Publ.
74. Shojib Hossain, M., et al., Improved Mechanical Properties of Fused Deposition Modeling-Manufactured Parts Through Build Parameter Modifications. *Journal of Manufacturing Science and Engineering*, 2014. **136**(6): p. 061002-061002-12.
75. Nidagundi, V.B., R. Keshavamurthy, and C. Prakash, Studies on parametric optimization for fused deposition modelling process. *Materials Today: Proceedings*, 2015. **2**(4-5): p. 1691-1699.
76. Onwubolu, G.C. and F. Rayegani, Characterization and optimization of mechanical properties of ABS parts manufactured by the fused deposition modelling process. *International Journal of Manufacturing Engineering*, 2014. **2014**.
77. Tymrak, B., M. Kreiger, and J.M. Pearce, Mechanical properties of components fabricated with open-source 3-D printers under realistic environmental conditions. *Materials & Design*, 2014. **58**: p. 242-246.

78. Chacón, J., et al., Additive manufacturing of PLA structures using fused deposition modelling: effect of process parameters on mechanical properties and their optimal selection. *Materials & Design*, 2017. **124**: p. 143-157.
79. Zein, I., et al., Fused deposition modeling of novel scaffold architectures for tissue engineering applications. *Biomaterials*, 2002. **23**(4): p. 1169-1185.
80. Stephen, A., K. Dalgarno, and J. Munguia. Quality assurance and process monitoring of fused deposition modelling made parts. in *High Value Manufacturing: Advanced Research in Virtual and Rapid Prototyping: Proceedings of the 6th International Conference on Advanced Research in Virtual and Rapid Prototyping*. 2013.
81. Ltd., S. ABSplus Spec Sheet. 2014 [cited 2017 08/17].
82. Bellini, A. and S. Güçeri, Mechanical characterization of parts fabricated using fused deposition modeling. *Rapid Prototyping Journal*, 2003. **9**(4): p. 252-264.
83. Mamadapur, M.S., Constitutive modeling of fused deposition modeling acrylonitrile butadiene styrene (ABS). 2010, Texas A & M University.
84. Li, L., et al., Composite modeling and analysis for fabrication of FDM prototypes with locally controlled properties. *Journal of manufacturing processes*, 2002. **4**(2): p. 129-141.
85. Sarle, W.S., *Neural networks and statistical models*. 1994.

86. Zhou, X., A. Malik, and S.-J. Hsieh. Life cycle monitoring of lithium-ion polymer batteries using cost-effective thermal infrared sensors with applications for lifetime prediction. in Thermosense: Thermal Infrared Applications XXXIX. 2017. International Society for Optics and Photonics.
87. Jacobs, J., et al., Framework for sequential approximate optimization. Structural and Multidisciplinary Optimization, 2004. **27**(5): p. 384-400.
88. Richter, J.N., On mutation and crossover in the theory of evolutionary algorithms. 2010: Montana State University.
89. Torres, J., et al., An approach for mechanical property optimization of fused deposition modeling with polylactic acid via design of experiments. Rapid Prototyping Journal, 2016. **22**(2): p. 387-404.
90. Deng, X., et al., Mechanical Properties Optimization of Poly-Ether-Ether-Ketone via Fused Deposition Modeling. Materials, 2018. **11**(2): p. 216.
91. Spoerk, M., et al., Parametric optimization of intra - and inter - layer strengths in parts produced by extrusion - based additive manufacturing of poly (lactic acid). Journal of Applied Polymer Science, 2017. **134**(41).
92. Gurralla, P.K. and S.P. Regalla, Multi-objective optimisation of strength and volumetric shrinkage of FDM parts: a multi-objective optimization scheme is used to

optimize the strength and volumetric shrinkage of FDM parts considering different process parameters. *Virtual and Physical Prototyping*, 2014. **9**(2): p. 127-138.

93. Srivastava, M., et al., Multi-response optimization of fused deposition modelling process parameters of ABS using response surface Methodology (RSM)-Based desirability analysis. *Materials Today: Proceedings*, 2017. **4**(2): p. 1972-1977.

94. Villalpando, L., H. Eiliat, and R. Urbanic, An optimization approach for components built by fused deposition modeling with parametric internal structures. *Procedia CIRP*, 2014. **17**: p. 800-805.

95. Boparai, K.S., R. Singh, and H. Singh, Modeling and optimization of extrusion process parameters for the development of Nylon6–Al–Al₂O₃ alternative FDM filament. *Progress in Additive Manufacturing*, 2016. **1**(1-2): p. 115-128.

96. Koziel, S. and L. Leifsson, *Simulation-driven design by knowledge-based response correction techniques*. 2016: Springer.

97. Bandler, J.W., et al., Space mapping technique for electromagnetic optimization. *IEEE Transactions on Microwave Theory and Techniques*, 1994. **42**(12): p. 2536-2544.

98. Echeverria, D., et al., Manifold-mapping optimization applied to linear actuator design. *IEEE transactions on magnetics*, 2006. **42**(4): p. 1183-1186.

99. Koziel, S. and S. Ogurtsov, Design optimisation of antennas using electromagnetic simulations and adaptive response correction technique. IET Microwaves, Antennas & Propagation, 2013. **8**(3): p. 180-185.
100. Le Gratiet, L. and C. Cannamela, Cokriging-based sequential design strategies using fast cross-validation techniques for multi-fidelity computer codes. Technometrics, 2015. **57**(3): p. 418-427.
101. Koziel, S. and L. Leifsson. Knowledge-based airfoil shape optimization using space mapping. in 30th AIAA Applied Aerodynamics Conference. 2012.
102. Robinson, T., et al., Surrogate-based optimization using multifidelity models with variable parameterization and corrected space mapping. Aiaa Journal, 2008. **46**(11): p. 2814-2822.
103. Zhou, X., S.-J. Hsieh, and Y. Sun, Experimental and numerical investigation of the thermal behaviour of polylactic acid during the fused deposition process. Virtual and Physical Prototyping, 2017. **12**(3): p. 221-233.
104. Antar, Z., et al. Thermophysical and radiative properties of conductive biopolymer composite. in Materials Science Forum. 2012. Trans Tech Publ.
105. Rodriguez, J., Modeling the Mechanical Behavior of Fused Deposition Acrylonitrile-Butadiene-Styrene Polymer Components. 1999, University of Notre Dame, Notre Dame, Indiana, USA.

106. Bergman, T.L., et al., Fundamentals of heat and mass transfer. 2011, Hoboken, NJ: John Wiley & Sons.
107. Garlotta, D., A literature review of poly (lactic acid). Journal of Polymers and the Environment, 2001. **9**(2): p. 63-84.
108. Labs, M.P., Moldflow Material Testing Report MAT2238-NatureWorks PLA 2007, Cargill Dow LLC: Minnetonka, USA.
109. Henton, D.E., et al., Polylactic acid technology. Natural fibers, biopolymers, and biocomposites, 2005. **16**: p. 527-577.
110. Pyda, M., R. Bopp, and B. Wunderlich, Heat capacity of poly (lactic acid). The Journal of Chemical Thermodynamics, 2004. **36**(9): p. 731-742.
111. Zhou, X. and S.-J. Hsieh. Evaluating convective heat transfer coefficients in fused deposition process using infrared imaging and neural networks. in Thermosense: Thermal Infrared Applications XL. 2018. International Society for Optics and Photonics.
112. Colaço, M.J., H.R. Orlande, and G.S. Dulikravich, Inverse and optimization problems in heat transfer. Journal of the Brazilian Society of Mechanical Sciences and Engineering, 2006. **28**(1): p. 1-24.
113. Roetzel, W., Iteration-free calculation of heat transfer coefficients in heat exchangers. The Chemical Engineering Journal, 1977. **13**(3): p. 233-237.

- 114. Woodbury, K.A., Inverse engineering handbook. 2002: Crc press.
- 115. Demuth, H.B., et al., Neural network design. 2014: Martin Hagan.
- 116. Dreiseitl, S. and L. Ohno-Machado, Logistic regression and artificial neural network classification models: a methodology review. Journal of biomedical informatics, 2002. **35**(5): p. 352-359.
- 117. Chudzik, S., Applying infrared measurements in a measuring system for determining thermal parameters of thermal insulation materials. Infrared Physics & Technology, 2017. **81**: p. 296-304.
- 118. ASTM, Standard Test Method for Tensile Properties of Plastic, in ASTM D638. 2014, ASTM: U.S.
- 119. Stratasys, L. Creating Variable Density Parts. 2014 [cited 2018 1/30/2018].
- 120. Ehsan Toyserkani, Y.S., Mihaela Vlasea. 3D Variable Density Printing. 2017 [cited 2018 1/30].
- 121. FlashForge. FlashForge Dreamer 3D Printer User Guide. 2017 1/30/2018].
- 122. Garg, A. and A. Bhattacharya, An insight to the failure of FDM parts under tensile loading: finite element analysis and experimental study. International Journal of Mechanical Sciences, 2017. **120**: p. 225-236.

123. Baikerikar, P.J. and C.J. Turner. Comparison of As-Built FEA Simulations and Experimental Results for Additively Manufactured Dogbone Geometries. in ASME 2017 International Design Engineering Technical Conferences and Computers and Information in Engineering Conference. 2017. American Society of Mechanical Engineers.
124. Letcher, T. and M. Waytashek. Material property testing of 3D-printed specimen in PLA on an entry-level 3D printer. in ASME 2014 International Mechanical Engineering Congress and Exposition. 2014. American Society of Mechanical Engineers.
125. Coello, C.A.C., G.B. Lamont, and D.A. Van Veldhuizen, Evolutionary algorithms for solving multi-objective problems. Vol. 5. 2007: Springer.
126. Ransikarbum, K., et al., Multi-objective optimization analysis for part-to-Printer assignment in a network of 3D fused deposition modeling. Journal of Manufacturing Systems, 2017. **43**: p. 35-46.
127. Laboratories, M.T. Price List (2014). 2014 [cited 2018 3/14]; Available from: <http://www.mtecmechanical.com/files/pricelist.pdf>.
128. Gramacy, R.B. and H.K. Lee, Cases for the nugget in modeling computer experiments. Statistics and Computing, 2012. **22**(3): p. 713-722.

129. Molga, M. and C. Smutnicki, Test functions for optimization needs. Test functions for optimization needs, 2005. **101**.
130. Bellini, A., Fused deposition of ceramics: a comprehensive experimental, analytical and computational study of material behavior, fabrication process and equipment design. 2002, Drexel University, Philadelphia, PA, USA: Philadelphia, PA.
131. Woodfield, P. and M. Monde, Estimation of uncertainty in an analytical inverse heat conduction solution. Experimental Heat Transfer, 2009. **22**(3): p. 129-143.
132. Penny, W.D. and S.J. Roberts, Error bars for linear and nonlinear neural network regression models. Technical report, Neural Systems Research Group, Imperial College of Science, Technology and Medicine, 1998.
133. Kasiviswanathan, K. and K. Sudheer, Methods used for quantifying the prediction uncertainty of artificial neural network based hydrologic models. Stochastic Environmental Research and Risk Assessment, 2002: p. 1-12.
134. D'Amore, A., et al., Numerical evaluation of structural relaxation-induced stresses in amorphous polymers. Composites Part A: Applied Science and Manufacturing, 2006. **37**(4): p. 556-564.
135. Wool, R.P., Polymer Interfaces: Structure and Strength. 1995, Munich, Germany: Hanser Publishers.

136. Rankouhi, B., et al., Failure analysis and mechanical characterization of 3D printed ABS with respect to layer thickness and orientation. *Journal of Failure Analysis and Prevention*, 2016. **16**(3): p. 467-481.
137. Chockalingam, K., N. Jawahar, and J. Praveen, Enhancement of anisotropic strength of fused deposited ABS parts by genetic algorithm. *Materials and Manufacturing Processes*, 2016. **31**(15): p. 2001-2010.
138. Montgomery, D.C., G.C. Runger, and N.F. Hubele, *Engineering statistics*. 2009: John Wiley & Sons.
139. Chen, Y., et al., Quantitative analysis of lithium-ion battery capacity prediction via adaptive bathtub-shaped function. *Energies*, 2013. **6**(6): p. 3082-3096.
140. Shaikhina, T. and N.A. Khovanova, Handling limited datasets with neural networks in medical applications: A small-data approach. *Artificial intelligence in medicine*, 2017. **75**: p. 51-63.
141. Bowden, G.J., H.R. Maier, and G.C. Dandy, Optimal division of data for neural network models in water resources applications. *Water Resources Research*, 2002. **38**(2).
142. Fiedler, B., et al., Finite-element modeling of initial matrix failure in CFRP under static transverse tensile load. *Composites Science and Technology*, 2001. **61**(1): p. 95-105.

143. Liu, Y. and H. Hu, Finite element analysis of compression behaviour of 3D spacer fabric structure. *International Journal of Mechanical Sciences*, 2015. **94**: p. 244-259.
144. Deng, S. and K. Suresh, Topology optimization under thermo-elastic buckling. *Structural and Multidisciplinary Optimization*, 2017. **55**(5): p. 1759-1772.
145. ASTM, Standard Test Method for Calibration and Accuracy Verification of Wideband Infrared Thermometers, in ASTM E2847 – 14. 2014, ASTM International: West Conshohocken, PA 19428-2959. United States.
146. Zhou, X., et al., Frequency-modulated thermography and clustering analysis for defect detection in acrylic glass. *Insight-Non-Destructive Testing and Condition Monitoring*, 2018. **60**(1): p. 28-36.

APPENDIX A

CALIBRATION OF INFRARED SENSOR

The calibration of the infrared sensor used in section 4 was performed based on ASTM E2847–14 standard [145]. A heating plate was selected as the flatplate radiation source which was used for infrared thermometer calibrations. It was covered with black electrical tape (Commercial Electric™) to increase the emissivity. The thickness of the tape is 0.152mm, which is negligible to the overall board thickness, while the emissivity of the tape is 0.945 [146]. A fully calibrated Compix® model 222 infrared camera was used as the transfer standard, corresponded to scheme II of ASTM E2847–14. Both the infrared camera and the infrared sensor were set to emissivity of 0.945 and mounted on a mounting fixture, with their field of views concentrated on and normal to the center of the flatplate. The distance between the infrared camera and the infrared sensor to the heating plate was set to 15cm and 7cm from the radiation source, respectively, to ensure adequate target size. During the calibration process, the surface temperature of the heating plate was varied from 40°C to 120°C, with a roughly 10°C increment each time. For each temperature point, the temperature readings from both devices were collected and averaged over 30 seconds, and the results before the calibration were listed in Table 21. It is seen that before calibration, the error between the two devices could be up to 3 degrees. Therefore, a cubic regression was performed, and the resulted fitting equation is

$$y = \sum_{i=0}^3 c_i x^i \quad (\text{I.1})$$

where y and x are the post- and pre- calibration values, respectively, and c are the correlation coefficients, has the form of [1.55933225e+00, 8.60625197e-01, 3.22146974e-03, -1.67403625e-05]. The results and error after performing calibration were also listed in Table 21, which demonstrated that the accuracy was greatly improved.

Table 21 The calibration results

Heating plate temperature settings (°C)	Infrared camera reading (°C)	Pre-calibration Infrared sensor reading (°C)	Post-calibration Infrared sensor reading (°C)	Difference after calibration (°C)
40	39.56	39.49	39.54	0.02
50	48.72	48.38	48.85	0.13
60	58.56	57.16	58.15	0.41
70	67.68	66.82	68.46	0.78
80	78.62	75.72	77.93	0.69
90	86.94	84.52	87.20	0.26
100	97.54	94.30	97.33	0.21
110	105.52	102.71	105.80	0.28
120	114	111.01	113.89	0.11

APPENDIX B

THERMAL MODEL APPLICABILITY ANALYSIS ON ANOTHER FDM MACHINE

In section 4, the applicability of the developed finite element model was tested on one FDM machine-Flashforge Dreamer (Machine A) and the results were satisfactory.

However, it is well known that FDM processes have variability between runs, between machines, and across time. This appendix section aims to numerically simulate the same process on a different FDM machine and the numerical data were compared with the experimental results to analyze the scalability and applicability of the established finite element model.

The machine used in this section is a MTW Create 3D Printer (Machine B), which is also a desktop-level FDM machine. The machine has a building area of 250 x 315 x 250mm and a building resolution of 0.01mm. It can be installed with two extruders, but the left extruder's nozzle was removed and replaced with the same IR sensor used in section 4 to observe the temperature distribution of the filament came from the right extruder, as demonstrated in Figure 54. The IR sensor was located 19mm from the right nozzle, resulted in a 1.37mm pixel resolution. The fabricated samples' geometry was the same, cuboids with the dimensions of 100 (length) by 10 (width) by 5mm (height) with hollow layers inside.

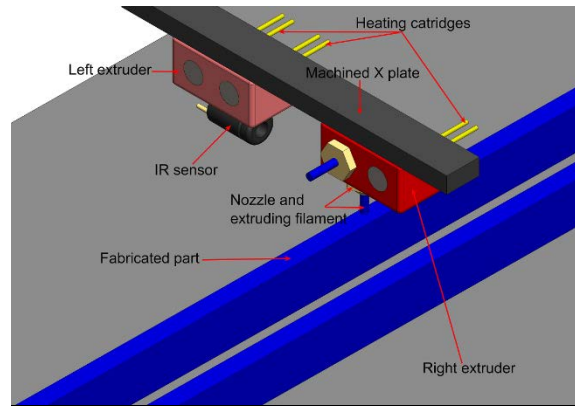


Figure 54 Schematic of experimental setup on Machine B

The design of experiment methodology was similar to that of section 3.2.1.3. Six conditions were selected to observe the different between experimentally acquired effective diffusion time and numerically computed values. With the convective heat transfer coefficient and thermal conduct resistance determined to be 61 and 4296 $\text{W/m}^2\cdot\text{K}$, respectively. And the results were listed in Table 22.

Based on the comparison of numerical and experimental results made in Table 22, it appeared that the developed numerical model can still reach less than 15% error on another FDM machine, demonstrated its applicability and scalability. Moreover, the obtained values on Machine B were still in the magnitude of $\sim 0.1\text{s}$, but were higher than those acquired on Machine A. It is suggested that the cooling effect on Machine B is not as strong as Machine A, possibility due to the structure difference and different cooling fan settings near the deposition region.

**Table 22 Comparison of experimental and numerical values of effective diffusion
time on Machine B**

No.	Nozzle temperature (°C)	Platform temperature (°C)	Printing speed (mm/s)	Layer thickness (mm)	$t_{\text{diff, exp}}$ (s)	$t_{\text{diff, sim}}$ (s)	Error (%)
1	200	70	60	0.2	0.139	0.133	4.44
2	200	70	80	0.2	0.105	0.111	5.75
3	220	70	80	0.2	0.119	0.111	7.06
4	210	60	80	0.15	0.117	0.100	14.80
5	200	70	80	0.25	0.113	0.123	8.98
6	220	60	40	0.25	0.245	0.215	12.33

APPENDIX C

EFFECT OF PROCESS PARAMETERS ON WALL WIDTH

In the process parameter settings of section 4, the width of perimeter/wall of the hollow layers was set at 1mm for all experimental conditions. However, different process parameter might affect it after the parts were fabricated. To validate the assumption that wall widths of the manufactured sample were uniform under different experimental conditions, measurement of the widths was made, and statistical analysis of the results was conducted.

For all nine experimental conditions, before the top solid layers of the samples were deposited, the wall width of the samples was measured at three random locations with a calliper (have a resolution of 0.01mm and accuracy of 0.02mm), and the results were presented in Table 23.

Table 23 Measurement results of the wall width for all experimental conditions

Width (mm)	Location 1	Location 2	Location 3	Avg.	Std.
1	0.97	0.97	0.96	0.97	0.01
2	0.96	0.98	0.99	0.98	0.02
3	0.94	0.96	0.95	0.95	0.01
4	1.00	0.96	0.99	0.98	0.02
5	0.96	0.97	0.97	0.97	0.01
6	0.98	0.99	0.97	0.98	0.01
7	0.97	0.98	0.96	0.97	0.01
8	0.97	0.99	0.99	0.98	0.01
9	0.96	0.95	0.98	0.96	0.02

It can be seen in Table 23 that the average wall widths of all conditions were in the range of 0.95 to 0.98mm, slightly lower than the set value of 1mm but were very close. To further investigate if manipulation of the printing parameters altered the wall thickness, the analysis of variance (ANOVA) was conducted and the statistical analysis results were listed in Table 24.

Table 24 ANOVA results of the wall width

Source	DoF	Adj-SS	Adj-MS	F-value	p-value
Nozzle temperature	2	6.89E-4	3.44E-4	2.21	0.138
Platform temperature	2	6.22E-4	3.11E-4	2	0.164
Printing speed	2	0.00109	5.44E-4	3.5	0.052
Layer thickness	2	4.67E-4	2.33E-4	1.5	0.25
Error	18	0.0028	1.56E-4		
Total	26	0.00567			

In Table 24, the p-values of the four varied printing parameters were 0.138, 0.164, 0.052, and 0.25, respectively. With the significance level of 0.05 and the null hypotheses that all individual means are equal, the null hypotheses were accepted for all parameters investigated, showed there is no significant difference between the mean widths of the various experimental conditions. Therefore, the same wall width was used in the developed simulation models.